A Digital Holographic Imager for Cloud Microphysics Studies

Thomas Edward Chambers

School of Physical Sciences

University of Adelaide

This thesis is submitted for the degree of

Master of Philosophy

April 2017

I dedicate this thesis to my parents without whom none of this would have been possible

Declaration Of Originality

I certify that this work contains no material which has been accepted for the award of any other degree or diploma in my name, in any university or other tertiary institution and, to the best of my knowledge and belief, contains no material previously published or written by another person, except where due reference has been made in the text. In addition, I certify that no part of this work will, in the future, be used in a submission in my name, for any other degree or diploma in any university or other tertiary institution without the prior approval of the University of Adelaide and where applicable, any partner institution responsible for the joint-award of this degree.

I give consent to this copy of my thesis when deposited in the University Library, being made available for loan and photocopying, subject to the provisions of the Copyright Act 1968.

I acknowledge that copyright of published works contained within this thesis resides with the copyright holder(s) of those works.

I also give permission for the digital version of my thesis to be made available on the web, via the University's digital research repository, the Library Search and also through web search engines, unless permission has been granted by the University to restrict access for a period of time.

Signed: ..... Date: .....

Acknowledgements

First and foremost, I extend my deepest gratitude to my supervisors; Murray Hamilton and Iain Reid. Throughout this project they have provided an endless source of knowledge, enthusiasm and encouragement and it has been an honour and a pleasure to have worked with them over these years. To Iain, your unique insights and suggestions regarding problems that I have faced along this journey are gratefully acknowledged as well as your support and encouragement along the way. Particular thanks must be extended to Murray for his seemingly limitless patience and wisdom displayed in all discussions throughout this project and for being a constant source of inspiration as both a scientist and a mentor. I have learnt much from this experience and I am deeply grateful for all the opportunities he has provided me with over the course of this project.

To my friends and colleagues in the atmospheric physics group, optics group and physics department; Andrew Spargo, Tuong Cao, Joshua Pease, Nicola Bilton, Andrew Heitmann, Nicky Luo, Simon Curtis, Baden Gilbert, Nadia Steyn, Jarryd Day, Rosa Hoff, Andrew MicKinnon, Bob Vincent, Mike Hatch, Steven Saffi, Josh Charvetto, Josh D'Agostino, Peter Veitch, Miftar Ganija, Eleanor King, Myles Clark, Lachlan Harris and David Ottaway as well as the other members whom I have spent time with. It has been a true pleasure meeting and spending time with you all over the years and it has made this journey a rewarding and thoroughly enjoyable experience. I am grateful to Andrew McKinnon, Bob Vincent, Peter Veitch, Won Kim, Neville Wild, Adrian Giffin, Adrian Selby, Blair Middlemiss, Joel Younger, Jesper Munch and Richard White for their useful insights on some of the technical aspects related to this project and to Bob Chivell for his expert technical assistance in the development of the instrument mounts.

I am grateful for the support from Robert Males and Philip Nelson of Tasnetworks for their assistance in installing the holographic instrument at their mountain site. The Bureau of Meteorology is also acknowledged for providing weather station observations during this testing.

Finally, my heartfelt thanks is extended to my external friends and family. Your unwavering support and encouragement has been invaluable to me and has allowed me to persevere in the face of all challenges encountered along this journey.

Abstract

Clouds play a crucial role in regulating the climatic and meteorological systems of planetary atmospheres due to their impact on the radiative transfer of electromagnetic energy through the atmosphere and in governing the hydrological (or equivalent) cycles. The role of clouds is of particular interest within the Earth's atmosphere where they cover approximately 70% of the Earth's surface and also have an impact on aircraft safety considerations due to aircraft icing and associated hazards.

To quantitatively understand the influence of clouds in an atmospheric system, the underlying physics of their formation, evolution and interaction with other atmospheric dynamical processes must be observed and modelled. These processes are governed by the underlying microphysical cloud properties such as the cloud particle shapes, sizes, spatial clustering and thermodynamic phase. Direct observations of these microphysical properties have historically proved challenging with large discrepancies seen between the outputs of climate models and direct observations, suggesting a lack of understanding of these processes.

Digital holography is a three dimensional imaging technique that allows direct measurement of many microphysical observables, such as the particle size distribution, particle shape distribution and spatial distribution, making it an attractive solution to this observational challenge. Previous instruments have been expensive and heavy devices, limiting their use to ground based observations or on board expensive research aircraft flights, which has severely limited the amount of data obtained from these instruments. There is therefore a need for a low cost, light weight digital holographic instrument suitable for deployment on a tower structure or weather balloon to obtain these critically needed measurements in remote and widespread regions. The development of such an instrument is outlined in this thesis.

Table of contents

List of figures

List of tables

Chapter 1

Introduction

1.1 Overview and Motivation

Clouds play a crucial role in the evolution, characterisation and habitability of planets due to their role in governing the radiative transfer of energy through a planetary atmosphere[1–4] and in maintaining the hydrological (or equivalent) cycle[5–7]. Clouds are of particular interest on Earth due to their important role in the climatic[8, 9] and meteorological systems[10] along with their influence on aircraft safety[11, 12], astrophysical observations[13] and severe weather events[14]. Despite considerable research interest, there remains much that is unknown about the formation, evolution and influence of clouds in planetary atmospheres. Much of this uncertainty stems from the complex microphysical processes[15–17], occurring on scales from nanometres up to centimetres inside of clouds, which have proven challenging to measure in a robust and reliable way. There is therefore a need for new instrumentation to be developed to improve our understanding of these enigmatic bodies.[18].

Clouds play a key role in the Earth's climate system due to their influence on the radiative transfer of energy through the atmosphere via the scattering and absorption of shortwave solar and longwave thermal radiation. Large discrepancies are seen between observations and predictions of climate models[19, 20], particularly over the polar regions[21, 22] which are particularly sensitive to a changing climate[23]. The International Panel on Climate Change (IPCC) has identified clouds as being one of the leading sources of uncertainty in model predictions[24] and hence an improved understanding of the physical processes that govern the large scale properties of clouds is crucial. Cloud properties vary on scales from nanometres to kilometres as a function of latitude, timescale and anthropogenic influence, making these systems particularly challenging to constrain observationally. The development of reliable climate models therefore requires reliable measurement instruments to be developed with high temporal and spatial resolutions.

The evolution and properties of large scale thunderstorms are strongly dependent on the underlying microphysical processes that mediate their formation[14, 25]. Dynamical effects such as convection[26] and turbulence[27] coupled with microphysical processes[28, 29] lead to complicated large scale storm properties that are challenging to predict and constrain[30]. The generation and nature of lightning, for example, has been considered to be one of the least understood problems in atmospheric physics[31, 32]. Various theories have been proposed relating lightning to the interactions of water droplets and ice crystals with high energy cosmic rays[33, 34] however, direct observations are critically needed to better understand these extreme processes[35, 36]. Such extreme weather events are of interest both from a theoretical point of view and also in improving early warning and prediction systems to mitigate the expensive damage caused by these processes.

A strong understanding of clouds is also important for astrophysical observations. The aerosol and cloud structure of the atmosphere is a fundamental component of the detection process in ground based high energy gamma ray[13] and cosmic ray[37] air shower detectors. A thorough understanding of the atmospheric scattering and absorption properties, as influenced by aerosol and cloud particles, is therefore required to obtain reliable data[38–40]. Clouds also play an important role in the study of exoplanets in orbit around other star systems. Recent observations suggest that exoplanet properties, such as the total water content, may be masked by the presence of clouds[41]. There is therefore a need to improve our understanding of cloud processes to improve the interpretation of observations[42] and in improving planetary models[43]. The existence and properties of clouds are also strongly linked to the habitability of planets via their role in the hydrological cycle and are therefore of interest in exoplanetary characterisation[44].

Observables of cloud microphysical processes include the cloud particle size distributions, cloud particle spatial distributions, the fraction of ice and liquid water, particle shape distribution, ice crystal roughness, cloud electric field distribution and aerosol properties. Given the dynamic and small scale nature of these observables, conventional measurement instruments such as the Cloud Particle Imager (CPI)[45] and the Forward Scattering Spectrometer Probe (FSSP)[46] have been unable to provide a full understanding of the complicated cloud processes[47] due to issues related to limited sampling volume sizes and problems associated with poor resolution capabilities. There is therefore a need for new instruments to be developed to better constrain these properties in forming theories to describe and predict the evolution of cloud systems.

Digital holography is a wavefront sensing technique that records both the amplitude and the phase of a coherent optical wavefront[48]. When applied to light scattered from a field of objects, this allows three dimensional (3D) images to be reconstructed with theoretically

diffraction limited resolution[49], making it an appealing tool for measuring cloud particle properties such as their shape, size and spatial distributions. Previous holographic instruments, such as the recently developed HOLODEC instrument[50], have been heavy and expensive devices which has restricted their use to ground based observations[51, 52] or on board expensive research aircraft flights[53]. This has severely restricted the amount of data obtained from these instruments, particularly over widespread and remote regions where data is critically needed. The aim of this project was therefore to develop a low cost, light weight digital holographic imaging device suitable for deployment on a tower structure or weather balloon to significantly improve observational capabilities of these important cloud microphysical observables, as required for the understanding of large scale cloud processes.

1.2 Thesis Organisation

In this thesis the development and experimental testing of a low cost digital holographic imager for the study of cloud microphysics is outlined. Chapter 2 presents a review of the underlying theory of cloud microphysics and a survey of modern observational techniques in the field. In chapter 3 the theory of digital holography is described along with results of the design, simulation and optimisation considerations for this holographic imager. Chapter 4 presents a summary of experimental testing results and characterisation of the instrument. Results of a field campaign in which the instrument was tested at a Tasmanian mountain site are presented in chapter 5 and chapter 6 provides a summary and outlook for future work.

Chapter 2

Cloud Microphysics

2.1 Introduction

The influence of clouds on the radiative transfer of energy through the atmosphere is a major source of uncertainty in climate models and weather forecasting. This discrepancy is largely due to the complicated interactions that govern the formation and evolution of macrophysical cloud properties such as their reflectivity, infrared absorption and total water content. These macrophysical properties depend on the underlying microphysical processes, that occur on scales of nanometers to centimetres, such as the condensation of water droplets, growth of ice crystals and their resultant optical scattering properties. The bulk cloud properties also depend on dynamical processes such as convection and turbulence; however, an emphasis is placed on the role of microphysics as the instrument developed in this work has been designed for the study of these processes.

In this chapter, the background theory of cloud microphysical processes and their impact on the Earth's climate system will be outlined, along with a review of the major observational techniques.

2.2 Theory Overview

Clouds form in the atmosphere via the conversion of water vapour in the air into water droplets and ice crystals referred to as cloud particles[54–56]. A thermodynamic mixture of condensed and vaporised water can exist in equilibrium when the vapour pressure of the water (e) is equal to the saturation vapour pressure (e_s) defined relative to a plane of water and the ratio of these quantities defines the Relative Humidity (RH) of the mixture. The growth of water droplets in a cloud is primarily due to the diffusion of water vapour onto

nucleating aerosol particles, as a result of differences between the ambient vapour pressure of the air and the local vapour pressure around the curved cloud particle surface. The formation of water droplets follows two distinct processes; homogeneous nucleation of vapour directly to the liquid phase and heterogeneous nucleation which involves a nucleating surface such as an aerosol acting as a Cloud Condensation Nuclei (CCN). Observations suggest that conditions for homogeneous nucleation of water droplets are rarely achieved in the Earth's atmosphere[55] and so only heterogeneous nucleation will be discussed in this overview.

In the heterogeneous nucleation process, an aerosol particle is required to act as a CCN from which the water droplet grows. Atmospheric aerosols may be classified as either primary or secondary aerosols based on their formation mechanism[57]. Primary aerosols are produced by direct transport of particles from the surface to the atmosphere via a range of processes such as sea spray, mineral dust, biogenic sources such as the decay of plant matter and anthropogenic sources. Secondary aerosols are produced directly in the atmosphere via the chemical interaction of sulphuric acid, produced for example from anthropogenic sources, with neutral gases and ions. The differing aerosol production mechanisms result in different aerosol sizes, number densities, chemical compositions and electrical properties, which significantly influence the large scale properties of the macroscopic clouds formed. These aerosol properties vary as a function of latitude, dynamical background effects and anthropogenic influence and the complex interplay between these factors result in large spatial and temporal variations in cloud formation around the Earth[58, 59], making worldwide measurements crucial in understanding the overall state of the atmosphere. Aerosol density in the atmosphere can be influenced anthropogenically through the emission of primary aerosols and via the subsequent chemical reactions of emitted gases that alter the atmospheric sulphuric acid concentration. Natural sources of aerosol variation also exist since the ion content in the atmosphere that regulates the production of secondary aerosols is influenced by meteors and cosmic rays[60, 61]. The extent of the influence of anthropogenic versus natural sources is a key uncertainty that must be constrained in producing accurate climate models[62].

Heterogeneous nucleation of water droplets in a cloud can be described by the interaction between the ambient water vapour field in the air and the local CCN properties. The saturation vapour pressure over such a water droplet can be derived to first approximation via thermodynamic arguments by considering the energy of surface tension on the surface of the particle along with the aerosol chemical properties. The resultant equation for the saturation vapour pressure around a cloud particle is referred to as the Kohler equation[54]

$$e_s'(a, n_w) = e_* \exp\left(\frac{2\sigma}{a\rho_l R_v T} - \nu\frac{n_s}{n_w}\Phi_s\right) \tag{2.1}$$

where e_s' is the saturation vapour pressure over the droplet surface, a is the droplet radius, n_w is the number of moles of water, e_* is the saturation vapour pressure relative to a plane surface of water, σ is the droplet surface tension, ρ_l is the density of water, R_v is the water vapour gas constant, T is temperature, ν is the chemical dissassociativity, n_s is the number of moles of aerosol species and Φ_s is a fitting factor. The first quotient in the exponential term can be attributed to the surface tension properties of the droplet and the second is due to the chemical composition of the aerosol mixture.

The difference between the saturated vapour pressure around a water droplet as predicted by the Kohler equation and that of the background air leads to water droplet growth by vapour diffusion. It can be shown that if the saturated vapour pressure around a water droplet becomes equal to the ambient vapour pressure, the water droplet will reach a stable equilibrium size, otherwise droplet growth will continue until the ambient vapour field is depleted or the droplet is removed from the cloud as rain[55]. It is this distinction between particles that grow freely in size via the diffusion of water vapour and those that remain at some fixed size in equilibrium with the background saturation vapour pressure that defines the difference between a cloud and a background mixture of aerosols. This diffusion based growth process is relatively slow and is unable to explain the broad particle size distributions observed in real clouds[63]. A more realistic model for water droplet growth includes the effects of collisional growth and coalescence which can be modelled as a stochastic collection process[64] influenced by the particle size, inertia and electric charges of the cloud particles. At small radii, the cross sectional collection efficiency is low and so the droplet growth is dominated by condensation. As the droplet grows, the probability of collision increases and hence the growth to larger rain droplet sizes is thought to be dominated by the collection process.

A major unsolved problem in cloud physics is the nature of the transition from the condensation growth regime to the collection growth regime[65]. This transition is crucial in understanding the production of rain in warm clouds, defined as those with a temperature greater than 0°C. Growth by condensation is observed to produce particles below the size required for efficient collectional growth in a homogeneous, uniform cloud and hence other mechanisms are required to explain the evolution of cloud particles into rain. A number of theories have been proposed to account for this discrepancy such as the role of micro scale turbulence in increasing particle densities that enhance local supersaturation[66],

giant aerosol CCN[67, 68], in the range of 1 to 10 microns, to seed larger particles by condensation and variations in the Liquid Water Content (LWC) within the cloud due to entrainment of unsaturated ambient air[69]. Observations of these processes have traditionally proved challenging with conventional detection methods and there is therefore a need for robust instruments, such as the one developed in this work, that can directly measure the microphysical state of the cloud in a statistically significant manner.

The formation and growth of ice crystals in a cloud can be described in a similar manner to water droplets; however, due to the crystalline nature of solid ice, the growth of ice crystals leads to more complicated shapes referred to as crystal habits. The molecular structure of water, along with the thermodynamic conditions in the atmosphere, constrain the possible crystal shapes that may form. Water can exist in 15 different known crystalline phases[70]; however, within the Earth's atmosphere only hexagonal ice and metastable cubic ice are believed to form based on laboratory studies[71]. In situ observations are still required to determine the prevalence of the metastable cubic ice structure in the atmosphere[72]. The large scale shape of ice crystals grown from cubic ice is more isotropic[70] than that from hexagonal ice, which favours irregular shapes such as hexagonal plates and columns and hence observational methods sensitive to particle shape such as polarisation studies and directing imaging methods should be suitable to study this phenomena.

Similarly to the formation of water droplets from water vapour, ice crystals may form via homogeneous and heterogeneous nucleation of water droplets or water vapour directly to the solid phase. Homogeneous nucleation occurs at temperatures below $\sim$ -38° C[73] and is thought to be an important process in cold cirrus clouds[74], Arctic Mixed Phase Cloud (MPC) formations[75] and in convective systems[76]; however, heterogeneous freezing is thought to be the dominant process for ice crystals formed in warmer tropical and equatorial clouds[77]. Heterogeneous nucleation of ice requires Ice Nuclei (IN) particles which are a subset of aerosols with properties that are suitable for ice crystal nucleation[78–80]. Growth of ice crystals is then governed by a range of processes such as vapour deposition[81], riming[82] and aggregation[83]. The complicated interactions of water vapour, liquid and ice is poorly understood and leads to a wide variety of ice crystal shapes observed in the atmosphere[84] as summarised in Figure 2.1[85]. The symmetric and fractal nature of many of these observed ice crystals allow their bulk properties, such as particle mass, to be parametrised by power law functions which simplifies their representation in models[86]. The local variations in temperature, relative humidity and electric field around the IN as it travels through the cloud also contribute to the range of observed shapes; however, much remains unknown about the quantitative details of the ice crystal growth process[87].

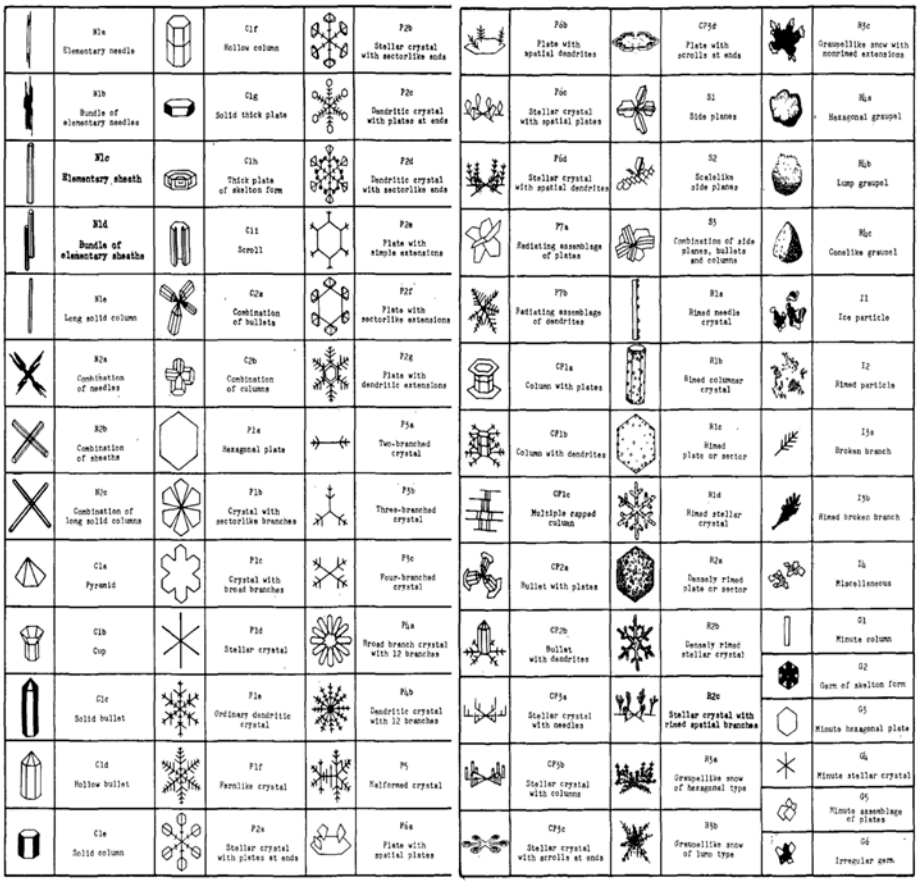

Fig. 2.1 Variety of ice crystal shapes observed in clouds. Figure reproduced from Magono and Lee (1966).

Since it is energetically more difficult to form ice crystals than water droplets, clouds consisting of mixtures of ice and supercooled liquid water are commonly observed, particularly in the polar regions[22, 88, 89]. The equilibrium vapour pressure for ice is lower than for liquid and hence in a mixture of ice and liquid in a MPC, it is expected that water droplets will evaporate whilst ice crystals tend to grow via vapour deposition. This process is referred to as the Wegener-Bergeron-Findeisen (WBF) mechanism[90] and suggests that MPC will become fully glaciated over the course of a few hours. Observations, however, indicate MPC lifetimes of days to weeks[91] suggesting a lack of understanding of the key physical processes that describe the evolution of MPC[92]. Observations of MPC in the Arctic indicate that supercooled water and ice is not homogeneously mixed within a cloud, with distinct layers consisting of a single phase identified[93]. Due to the considerably different optical properties of water droplets and ice crystals[94, 95], this layering can signif-

icantly affect the radiative properties of the cloud[96] and must therefore be characterised in climate modelling. This underlying complexity is part of the reason that the Arctic climate is so poorly understood and presents such a large source of uncertainty in global climate modelling[97, 98].

2.2.1 Cloud Microphysics and Climate

Radiative transfer of electromagnetic energy through the Earth's atmosphere is a key driver of climatic and meteorological processes. As a result of the complicated formation and evolution of clouds, as outlined in the previous section, there is significant uncertainty attributed to the role of clouds in the radiative transfer process. This lack of understanding is apparent in climate models where clouds are acknowledged to be one of the largest sources of uncertainty and hence there is significant interest in improving our understanding of the physical processes that govern the scattering and absorption properties of clouds.

Radiative transfer describes the balance between incoming shortwave solar radiation and longwave thermal radiation in the atmosphere. The net radiative effect of clouds relative to clear skies, at the top of atmosphere or surface, is described by the Cloud Radiative Forcing (CRF) which quantifies the net cooling or warming effect of clouds. The CRF can be described by the following relation[23]

$$CRF = F(A_c) + Q(A_c) - F(0) - Q(0) \tag{2.2}$$

$$= CRF_{LW} + CRF_{SW} \tag{2.3}$$

where F and Q are the net surface longwave and shortwave fluxes measured in W/m^2 and A_c is the cloud cover fraction. This parameter varies significantly as a function of latitude, aerosol conditions and timescale[99]. This large variability is due to the complicated scattering and absorption interactions between optical photons and micrometer sized cloud particles. The scattering properties of cloud particles depends on their geometric properties such as particle size, shape, surface roughness, refractive index and on their spatial distribution. This complexity is challenging to accurately model and hence large discrepancies are seen between observations and model outputs[100]. This is highlighted in Figure 2.2 which shows the differences between the time averaged modelled longwave and shortwave CRF and satellite measurements of these quantities. These significant discrepancies correspond to large variations in predictions of quantities such as the mean surface temperature[101, 102] and hence it is crucial that these uncertainties are reduced through a better understanding of the role of clouds in the atmosphere.

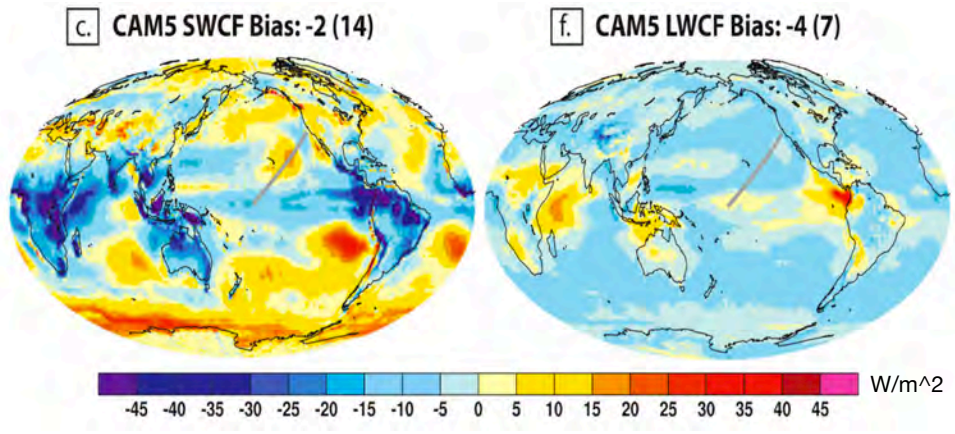

Fig. 2.2 Difference between observed and modeled CRF_{LW} and CRF_{SW} across the globe. Figure adapted from Kay (2012).

The radiative properties of clouds are parametrised within climate models by considering the bulk optical properties of a distribution of cloud particles within some volume[103]. These bulk optical properties are typically described by the averaged scattering phase function $P(\theta)$, or its parametrisation via the asymmetry factor (g), averaged single scattering albedo ($\widetilde{\omega}$) and mass extinction coefficient (k_{ext})[104]. The mass extinction coefficient, for example, can be parametrised by the following relation[105]

$$k_{ext} = \frac{\int_{\lambda_{\min}}^{\lambda_{\max}} \int_{D_{\min}}^{D_{\max}} \sum_{h=1}^{M} \left[Q_{ext,h}(D,\lambda) A_h(D) f_h(D) \right] S(\lambda) n(D) \, dD d\lambda}{\int_{\lambda_{\min}}^{\lambda_{\max}} \int_{D_{\min}}^{D_{\max}} \sum_{h=1}^{M} \left[V_h(D) f_h(D) \right] S(\lambda) n(D) \, dD d\lambda} \tag{2.4}$$

where λ is wavelength, D is the particle size, M is the number of particle habits, $f_h(D)$ is the particle habit distribution, $S(\lambda)$ is the source spectrum, $n(D)$ is the particle size distribution, $A_h(D)$ is the particle area distribution, $V_h(D)$ is the particle volume distribution and $Q_{ext,h}$ parametrises the single scattering properties for a given habit. The other bulk optical parameters can be described by similar relationships and therefore to model these properties, direct knowledge of both the single scattering properties of various ice crystal geometries [95] as well as realistic particle size, shape, area and volume distributions[86] is required. The single scattering properties can be calculated using scattering theories such as the Discrete Dipole Approximation (DDA)[106] or T matrix method[107]. Scattering properties are determined for a range of wavelengths, particle sizes and surface roughnesses

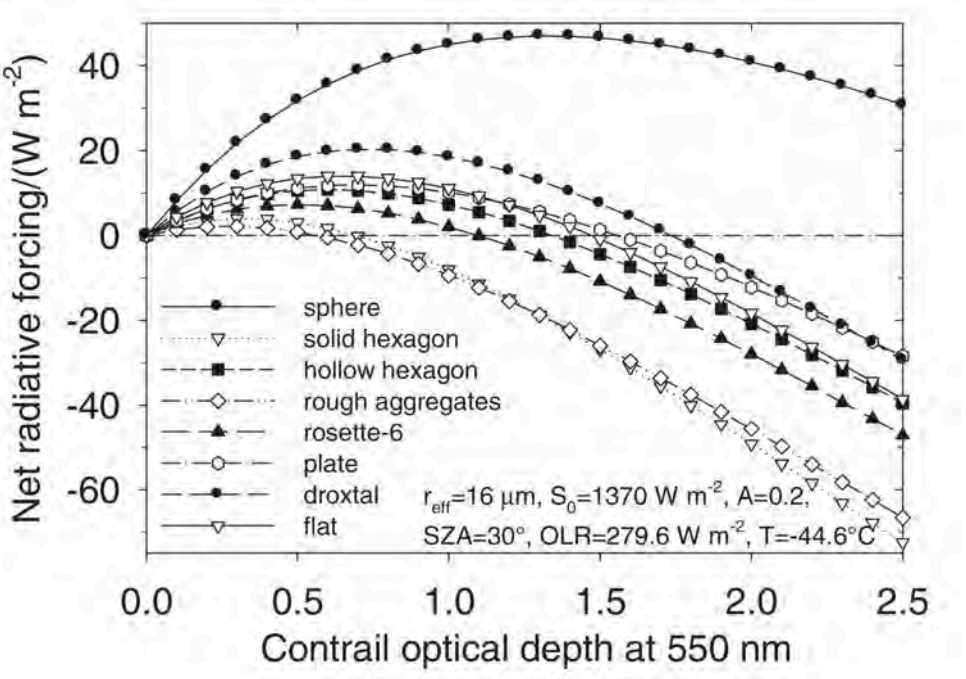

Fig. 2.3 Comparison of the modelled CRF as a function of cloud particle shape and cloud optical depth. Figure reproduced from Schumann et al. (2012).

and then stored in look up tables[95, 108]. The particle size, shape, area and volume distributions can be directly measured by in situ instruments[86, 109] such as the one developed in this work. Given the complexity of cloud formation, there is a need to increase the amount of these in situ microphysical measurements for a range of cloud types and seasonal conditions to better parametrise cloud effects in climate models and remote sensing retrieval algorithms[110]. There is also a need to determine the variation of these properties with respect to other factors such as temperature[111] and spatial homogeneity[53] within the cloud.

Once parametrised, the bulk optical properties are then used as inputs to the radiative transfer equations to determine the net radiative effect of clouds. The sensitivity of model outputs such as the CRF to the underlying microphysical parametrisations have been demonstrated by various authors[105, 112]. This model sensitivity is highlighted in Figure 2.3 which shows the modelled CRF as a function of cloud particle habit and cloud optical thickness. It is seen that by varying the cloud particle shape, the net CRF can go from positive to negative and hence will produce a net cooling or warming dependent directly on particle habit. Direct observations of these ice crystal shape properties are therefore required in obtaining realistic climate models.

2.3 Measurement Techniques

Given the significant lack of understanding of cloud microphysical processes, both in the Earth's atmosphere and in those of other planetary atmospheres, a large experimental effort has gone into measuring these processes. Observational techniques can be broadly classified as either remote sensing measurements[113] or direct in situ detections[47] and both of which will be reviewed in this section.

2.3.1 Remote Sensing

Remote sensing methods sample the atmosphere without making physical contact with the system being studied. Remote sensing of clouds is commonly performed using either passive imaging/radiometric detectors of reflected solar and thermal radiation or with active techniques such as LIDAR and radar that transmit electromagnetic energy through the atmosphere and measure the reflected signal. Remote sensing instruments can be installed on board satellites in orbit around the Earth to obtain measurements with a high spatial resolution or deployed at ground based field sites to obtain measurements with a high temporal resolution. These instruments are typically expensive and this limits the widespread deployment of such instruments and similarly in remote areas where detector maintenance can be challenging.

Due to the large detection distances involved, these instruments cannot directly sample the microphysical properties of clouds and must infer these using single scattering calculations and assumptions of the underlying microphysical state based on results from direct in situ observations[110, 114, 115]. Modelling of the single scattering properties of ice crystals is performed for a range of habits, crystal sizes, surface roughnesses and wavelengths and these results are stored in look up tables[95, 108]. In situ observations, such as particle size distributions and particle habit distributions[86, 109], are then used with the single particle scattering properties to calculate the bulk scattering properties of the clouds such as the effective particle size (D_{eff}), Ice Water Content (IWC) and Cloud Optical Thickness (COT)[116]. Radiative transfer equations[117] are used to calculate the properties of the reflected signal for a range of microphysical configurations. These modelled bulk scattering properties are then compared to remotely sensed bulk scatter measurements and the model parameters that give the best agreement are taken as the retrieved microphysical parameters.

Remote sensing observations can be used to validate the outputs of global climate models such as D_{eff}, IWC and CRF. The accuracy of the remote sensing retrieval is strongly dependent on the reliability of the input in situ observations used to parametrise the modelled ice cloud properties[19, 118]. This dependence is highlighted in Figure 2.4 which shows the

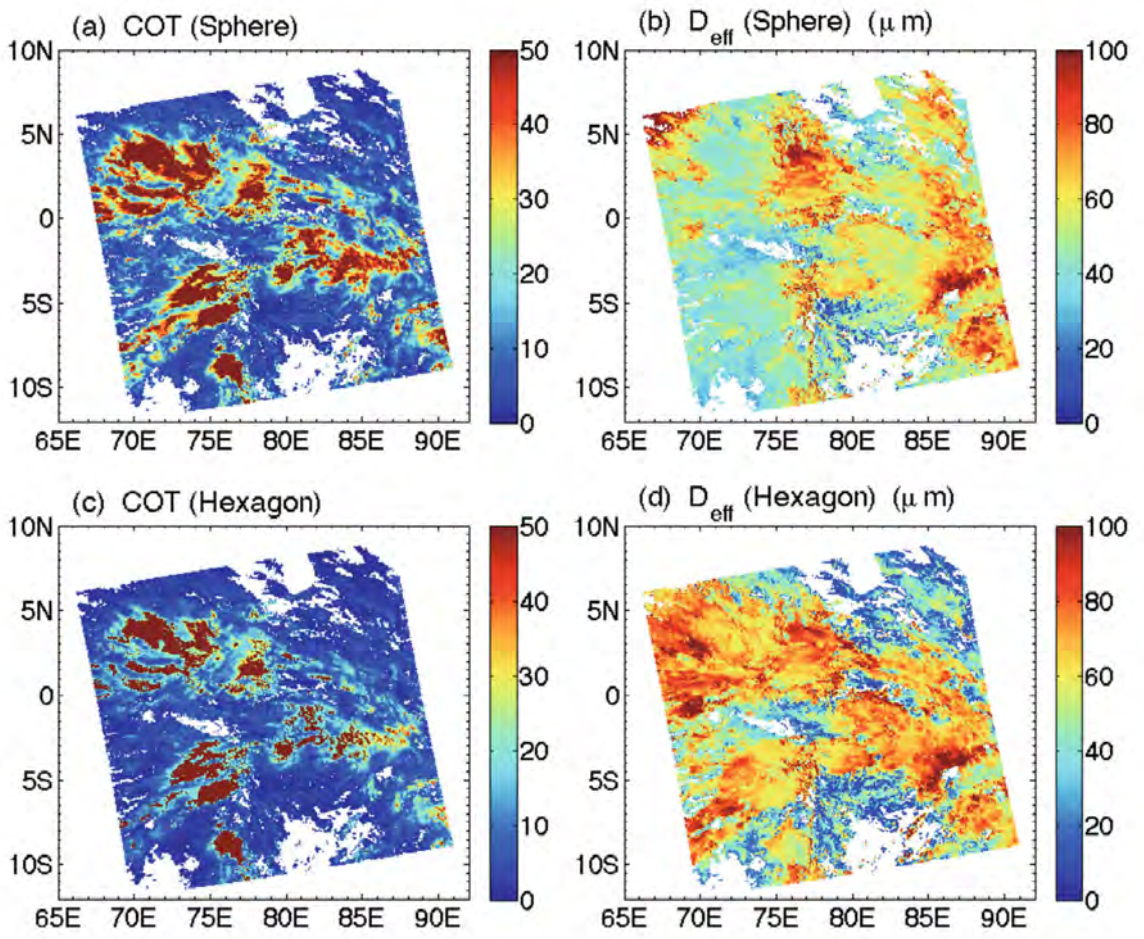

Fig. 2.4 Effect of particle shape assumption on MODIS retrievals of cloud optical thickness and effective particle size. Figure reproduced from Yang (2015).

difference in retrievals of COT and D_{eff} from the satellite borne MODIS instrument based on an assumption of either spherical ice crystals or hexagonal crystals[116]. Further in situ observations over widespread regions and large time scales are critical to obtain an accurate climatology of these inputs to better parametrise ice cloud optical properties.

The fraction of ice and liquid water in a cloud can be inferred remotely through measurements of the depolarisation of scattered light via polarimetric instruments[119] such as the CALIOP LIDAR on board the CALIPSO satellite[120]. Liquid water droplets are spherical and hence a low depolarisation of scattered light is observed whereas ice crystals can have more complex geometries and correspondingly larger depolarisations, allowing such devices to distinguish between the two phases[121]. The cloud IWC can be extracted from these instruments by using empirical relationships between the backscattered signal

and IWC derived from in situ observations[122]. Discrepancies are noted between remote sensing retrievals of IWC and in situ observations[123, 124] suggesting a need for further in situ measurements to better parametrise the input empirical models and to identify potential dependences on other factors such as temperature, cloud particle spatial distribution and seasonal effects.

LIDAR measurements require assumptions to be made about the signal penetration depth into optically thick clouds[125], although progress is being made to resolve this limitation[126], which leads to uncertainty in the derived observables[125]. MPC have been observed to form distinct layers of supercooled liquid water and ice and hence a full vertical profile of the cloud is required to adequately characterise the cloud state. Radar return signals are dependent on the size of the scattering cloud particles[127–129] and hence returns are typically dominated by scatter from large ice crystals, masking the detection of smaller liquid water droplets, which adds further uncertainty to results derived from these techniques. In situ measurements are therefore also critical in validation of these remote sensing techniques.

2.3.2 In Situ Measurements

In situ techniques require direct physical contact between the cloud and the measuring instrument. This allows very accurate measurements to be made by such devices with minimal assumptions necessary and hence are critical for calibration and validation of remote sensing techniques. The key downsides to such instruments are the significant engineering challenges involved in operating such devices in the extreme temperature and turbulence conditions encountered within clouds, difficulties in physically making contact with a cloud and limited spatial and temporal resolutions as compared to remote sensing techniques.

Various techniques are utilised to reach typical cloud heights including research aircraft flights[21, 130, 131], ground based observations on mountains[51, 52, 132] and balloon borne instruments[133–136]; however, each approach has inherit limitations. Research aircraft flights allow sampling within the entire volume of a cloud; however, flights are expensive and can be dangerous during extreme weather events which limits the amount of data obtained from this approach. Ground based observations allow measurements with large temporal resolutions, yet are unable to measure the vertical distribution of cloud properties. Balloon observations allow frequent measurements to be made, both spatially and temporally, given the low cost nature of the technique; however, there is an inherit risk of loss of the instrument and hence low cost instruments must be designed for this particular platform. A large uncertainty associated with any in situ technique, particularly those on research aircraft due to the large flight speeds, are the sampling biases induced by interaction of the instrument with the environment, such as the shattering of ice crystals on the tips of

instrument probes[137]. Ice crystal shattering leads to anomalously large distributions of small ice crystals and must be avoided via design choices or corrected for in analysis.

2.3.2.1 Impaction Techniques

Ice crystals can be directly sampled in clouds and studied in the lab using single impaction techniques[110]. Ice crystals are captured on a cover glass or emulsion coated surface and then shape and size properties are determined individually using microscopy techniques. Particles larger than roughly 100 microns can not be reliably sampled using this technique due to shattering problems. Freezing of ice crystal samples in liquid nitrogen allows high resolution scanning electron microscopy imaging to be performed[138] providing insight into the roughness and 3D information of single ice crystals. A key drawback to these techniques is that information about the spatial and statistical properties of the cloud is lost with single particle measurements and hence instruments that sample an entire particle field are also required. Analysis of impaction data is difficult to automate due to the use of physical glass slides and hence large datasets are particularly challenging to study with this approach.

2.3.2.2 Optical scattering Probes

Optical scattering probes relate measurements of scattering intensity to particle size using the results of scattering theories such as the Mie scattering theory[139, 140]. Scattering probes are capable of measuring very small particles on the order of half a micron[141]; however, they are unable to accurately size large particles greater than a few hundred microns[142]. Scattering detectors such as the FM-100 fog monitor[143], Forward Scattering Spectrometer Probe (FSSP)[46] and Cloud Droplet Probe (CDP)[144] assume spherical scattering targets and hence tend to underestimate the size of aspherical ice crystals resulting in ambiguous measurements[145], particularly in MPC[146]. The Cloud, Aerosol and Precipitation Spectrometer with depolarisation (CAS-DPOL)[47] and Polarsonde are new scattering instruments that allow discrimination between particle shapes based on the scattering angle and depolarisation of backscattered light; however, complex Monte Carlo modelling is needed to interpret the scattering properties of multiple particles of varying shape and phase within a given field of view.

2.3.2.3 2D Imaging Probes

Imaging probes directly record the shape and size of particles within a defined field of view and depth of field that determines the sampling volume for the instrument. Measurements derived from images are typically less restricted by particle properties such as shape, size

and refractive index than with scattering probes as these parameters can be directly inferred from the image with few assumptions. This improved determination of size and shape properties allows imaging devices to resolve particles over a larger size range than scattering probes; however, the lower resolution limit is typically poorer due to the large pixel sizes in current CCD and CMOS cameras. Detectors that use conventional 2D imaging such as the Cloud Particle Imager (CPI)[45] and Cloud Imaging Probe (CIP)[147] suffer a number of key limitations. The sampling volume within these devices is difficult to accurately constrain, resulting in significant uncertainties in the calculation of number densities of particles[110, 148, 149]. The challenges in defining the sampling volume of these instruments requires many images to be used to build up a statistically significant number of cloud particle observations. This reduced statistical sampling poses a challenge for airborne measurements. As the balloon or aircraft is non stationary, multiple images are recorded at different spatial locations and hence spatial homogeneity within the cloud must be assumed to derive statistical distributions, which is a major source of uncertainty inherent in this technique[53].

2.3.2.4 3D Imaging Probes

Three dimensional (3D) imaging devices, such as stereoscopic[150] and holographic[151] detectors, offer a much larger sampling volume than in conventional two dimensional (2D) imaging detectors. This enhanced sampling volume allows statistically significant sampling of particle distributions within a single image acquisition step[50] without the need for assumptions of spatial homogeneity within the cloud. 3D imaging techniques allow the spatial distribution of particles within the enhanced sampling volume to be compared and sub volumes (voxels) can be searched for unusually high concentrations of small particles, allowing discrimination and correction for ice crystal shattering effects in the dataset[152]. The measurement of the entire 3D volume allows analysis of the spatial correlation properties of particles within the cloud. This parameter is related to microscale turbulence[27] which can significantly affect the overall radiative properties of the cloud and can presently only be measured using 3D imaging devices[153].

Digital stereo imaging is a well established technique in many disciplines[154–158] that has been widely used in the measurement of macrophysical cloud properties[159, 160] and more recently in the study of cloud microphysics[161, 162]. These techniques typically use a paraxial ray optics model for light incident on an array of spatially separated cameras. Sophisticated reconstruction algorithms incorporating geometric triangulation and focussing criterion are then used to reconstruct the 3D properties of the target using the individual images[163]. The accuracy of this technique is dependent on the relative distance of the objects to the cameras which can be difficult to account for[164, 165]. Increasing the number

of cameras used in the detector significantly improves the accuracy of this method; however, it comes with a significant increase in computational time, making real time measurements challenging. Photogrammetry[166] can be used to measure the sizes and number densities of particles in the sampling volume; however, this requires careful calibration of the camera geometry[167] and the inclusion of known reference objects in the field of view adding complication to measurements.

Stereo imaging devices have further drawbacks when designing low cost imaging systems that are required for widespread deployment and application in remote environments. Low cost digital cameras typically use CMOS type imaging sensors rather than more sophisticated CCD arrays, due to their reduced production costs. These cameras are prone to read noise errors, large dark currents and optical aberrations due to low quality optics. The random nature of these noise sources make integration of multiple CMOS camera measurements complicated due to the uncorrelated noise between them. CMOS cameras typically incorporate a rolling shutter readout mechanism[168] as opposed to the global shutter mechanism commonly used in CCD arrays. A rolling shutter reads the state of the camera frame by recording and resetting the charges stored on each row of pixels, starting from the top and progressing to the bottom of the frame. As each row is read out at a different time, this mechanism leads to unphysical artefacts in rapidly varying object fields. The rolling shutter artefact, limited hardware control and poor electronic response times of CMOS cameras make synchronisation between multiple cameras challenging. Reconstruction algorithms require simultaneous measurements from each camera and hence this poses a major problem for using stereo imaging methods in low cost measurement devices.

2.3.2.5 Digital Holography

Holography is a wavefront sensing technique that allows both the amplitude and the phase of a coherent optical wavefront to be recorded via a single 2D image acquisition[169]. The technique was originally developed to overcome the limitations of lens aberration in microscopy and x-ray crystallography[170] and is now used in a wide range of disciplines[171–181]. By recording the scattered wavefronts from a field of objects, this technique allows 3D images to be reconstructed[182, 183] with diffraction limited resolution, making it an appealing method for the study of cloud particles. The holographic imaging technique has been demonstrated over a broad range of the electromagnetic spectrum[184–188] ranging from infrared to gamma ray wavelengths, allowing image reconstruction to nanometer scale precision[189, 190]. Holographic imaging was originally performed using photographic emulsions[191–193] which required extensive processing times; however, considerable effort in recent times has led to the development of digital holography[48] in which the images are

recorded using electronic CCD or CMOS sensors. The instrument designed in this project is a digital holographic imager and hence a more extensive review of the theory is outlined in the following chapter.

Both analogue[194–197] and digital[51, 148, 198–200] holographic probes have been previously developed for the study of climate science and cloud microphysics. Many of these instruments are no longer in use, possibly as a result of the expensive operational costs involved, large datasets and computational burdens required for holographic reconstruction. Computational technology has advanced rapidly in recent years and as a result, digital holography has become an increasingly more feasible technique. The holographic devices that are still in use for atmospheric studies have successfully been used for the measurement of particle size distributions and ice crystal habit retrieval; however, these instruments are expensive and heavy, limiting their use to ground based applications[51, 52] and airborne measurements via expensive research aircraft flights[53]. The significant costs involved has severely limited the amount of observations obtained from these instruments, particularly over widespread and remote regions where in situ observations are critically needed. For this reason, there is a need for a low cost, light weight holographic detector that can be regularly deployed on standard weather balloons or stationary tower structures in remote regions. The development of such an instrument is outlined in this thesis.

Chapter 3

Digital Holographic Imager Design and Optimisation

3.1 Introduction

Holography is a wavefront sensing technique in which the amplitude and phase of coherent optical wavefronts can be recorded from a single acquisition of a diffraction pattern. Present day CMOS and CCD based cameras can only directly measure the intensity of optical wavefronts as the phase of such waves oscillates at frequencies on the order of hundreds of terahertz, which is far greater than the bandwidth of current electronic devices. In holographic imaging, coherent scattered wavefronts from a field of objects are interfered with a well constrained reference wavefront and the resultant interference pattern encodes information about the scattered wavefront amplitude and phase. The shape of a wavefront is determined by the phase factor and when applied to light scattered from a field of objects, it is this wavefront shaping that encodes information about the propagation distance as required for a three dimensional imaging system.

Digital holography is a recent extension of the holographic technique whereby an interference pattern, or hologram, is recorded on a CCD or CMOS camera and the three dimensional image is reconstructed numerically using electromagnetic diffraction theory. Applications of this technique to the study of cloud microphysics have been severely limited owing in part to the extreme temperature, condensation and turbulence conditions encountered within a cloud and the corresponding design challenges that must be overcome. The large datasets produced by holography provide further challenges, necessitating the development of robust automated analysis routines to extract microphysical observables from the raw three dimensional images.

As a result of these challenges, previous instruments have been expensive and heavy, limiting their use to aircraft observations or ground based studies with very few instruments presently in use. The cost of such instruments prohibits their deployment over widespread and remote regions which presents severe sampling biases in the study of global cloud properties, particularly over remote regions where the data is most needed due to the large discrepancies seen between climate models and existing observations. Research aircraft flights are also expensive and can be dangerous in extreme weather conditions, which further limits the deployment of such instruments. There is therefore a need for a low cost, autonomous and robust holographic imager that can be deployed routinely on weather balloons or tower structures to significantly increase the available data and provide unique insights into the microscopic cloud physics processes as required for a robust understanding of overall cloud properties.

In this chapter, the background theories of electromagnetic diffraction and holography are outlined, along with the design and optimisation considerations involved in the development of a robust digital holographic imager suitable for deployment on a weather balloon or tower structure for the study of cloud microphysics.

3.2 Digital Holographic Imaging Theory

The holographic technique can be used to record a three dimensional image of a scene of objects from a single recording of a diffraction pattern. The theory behind this process as applied to the detector geometry of the imaging device designed in this project, a coherent spherical wave light source placed coaxially with a CMOS camera sensor, can be derived as follows[201]. Light can be modelled as an electromagnetic wave, with the transported energy contained in the oscillating magnetic and electric fields of the wave. The operation of Silicon based camera sensors is based on the interaction of electric dipoles with the incident light and hence it is sufficient to only consider the electric field component in deriving the holographic theory. To simplify this discussion only monochromatic, fully coherent waves will be considered; however, it can be shown that the following argument also applies to more general cases[202]. Such an electric field can be mathematically described by the following relation

$$\widetilde{E} = E_0(x,y)\cos(\omega t + \phi(x,y)) = \mathrm{Re}\{E_0 e^{i\omega t} e^{i\phi}\} \tag{3.1}$$

where E_0 is the amplitude of the wave, ω is the optical frequency, ϕ is the phase and the spatial dependence has been made implicit in the definition of each term. For simplicity, the frequency dependence will be ignored and the real component assumed implicitly. Consider now the superposition of two mutually coherent optical waves; a reference wavefront ($\widetilde{E_R}$) and a scattered wavefront from a point source scattering target ($\widetilde{E_O}$). The superposition of these waves is recorded with a camera sensor as shown in Figure 3.1 which illustrates the in line detector geometry used in this project. As the oscillation frequency of the optical waves is too fast for the camera electronics, only the time averaged intensity of this superposition is recorded on the camera as described by the following relations

$$\begin{aligned} I &= \left|\widetilde{E_R} + \widetilde{E_O}\right|^2 \\ &= \left|E_R e^{i\phi_R} + E_O e^{i\phi_O}\right|^2 \\ &= \left(E_R e^{i\phi_R} + E_O e^{i\phi_O}\right)\left(E_R e^{-i\phi_R} + E_O e^{-i\phi_O}\right) \\ &= E_R^2 + E_O^2 + E_0 E_R e^{i(\phi_R - \phi_O)} + E_0 E_R e^{i(\phi_O - \phi_R)} \\ &= E_R^2 + E_O^2 + 2E_0 E_R \cos(\phi_O - \phi_R) \end{aligned} \tag{3.2}$$

where I is the intensity of the interference pattern, referred to as a hologram, recorded by the camera. The first two terms in equation 3.2 represent a DC background intensity in the hologram which can be filtered out to improve the Signal to Noise Ratio (SNR). The third term represents an oscillating intensity pattern across the hologram with the modulation intensity and frequency containing information about the amplitude and phase of the object wavefront. Since the optical wavefronts obey the superposition principle, this argument can be extended to an arbitrary distribution of spherical wave point sources and hence the complex optical wavefronts for an arbitrary distribution of objects can be recorded by this technique. This recording constitutes the first stage in a two stage holographic three dimensional imaging system and is equivalent for both analogue holography, using photographic emulsions for recording and optical image reconstruction, and the more recently developed digital holography using CCD/CMOS cameras and numerical image reconstruction.

The second stage of a digital holographic imaging system is the numerical reconstruction of the original object wavefront and hence a three dimensional image of the object field. According to the scalar theory of diffraction, the amplitude and phase of an optical wavefront can be calculated at an arbitrary propagation distance provided the amplitude and phase are recorded within some aperture[203]. To extract this amplitude and phase information

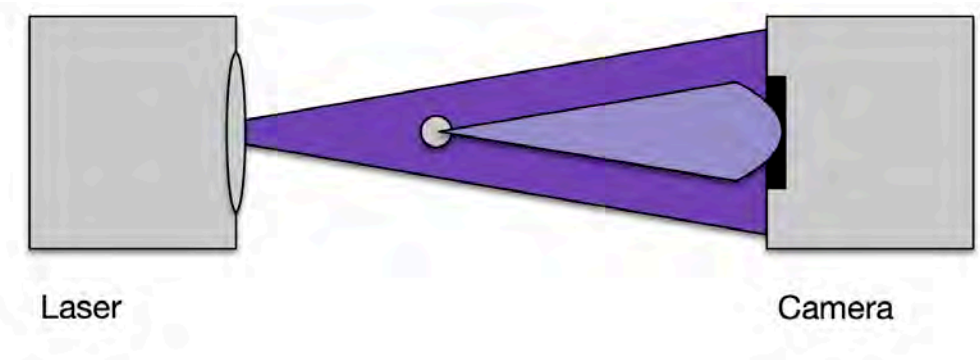

Fig. 3.1 In line holographic recording geometry. The laser produces a coherent wavefront which is then scattered from the object to be imaged. The interference pattern between the scattered object wavefront and the background reference wavefront is then recorded on the camera detector placed in line with the laser and objects.

from the recorded hologram, it is sufficient to multiply it by a numerical reference wavefront equivalent to the recording reference wave as shown

$$\begin{aligned} E_R e^{i\phi_R} I &= E_R e^{i\phi_R}\{E_R^2 + E_O^2 + E_0 E_R e^{i(\phi_R-\phi_O)} + E_0 E_R e^{i(\phi_O-\phi_R)}\} \\ &= \{E_R^2 + E_O^2\}E_R e^{i\phi_R} + E_O E_R^2 e^{i2\phi_R} e^{-i\phi_O} + E_R^2 E_O e^{i\phi_O}. \end{aligned} \tag{3.3}$$

The first term in equation 3.3 is the zero order diffraction of the reference wavefront which can be filtered out during the reconstruction process to improve the SNR. The second term is a reconstructed object wavefront with conjugate phase representing a virtual twin image term in the reconstruction. This term is modified by the phase of the reference wavefront and is therefore treated as a noise term due to this wavefront distortion. Various techniques have been developed to deal with this term, such as spatial filtering in an off-axis recording geometry[204] or iterative procedures based on the conservation of energy[205]. It can be shown that this error term is only dominant for inferring internal structure of large objects such as ice crystals and so for many applications it is not necessary to correct for the effects of this term[206]. The final term is an undistorted reconstruction of the original complex object wavefront in both amplitude and phase and it is this term that can be propagated via diffraction theory to reconstruct the object field at arbitrary depth positions.

The numerical diffraction of this object wavefront to a range of depth positions allows both the spatial intensity and phase distribution of the object wavefront to be reconstructed at each depth, which constitutes the three dimensional image reconstruction stage of the holographic process. Numerical diffraction is carried out in software by application of the Rayleigh-Sommerfeld (RS) diffraction theory[207] which allows the complex optical wavefront to be reconstructed at arbitrary depth positions, provided the complex wavefront is recorded in some aperture plane. This condition is satisfied by the final term in equation 3.3. The complex wavefront at an arbitrary depth is given by the Huygens-Fresnel relation

$$U(x,y,z) = \frac{z}{i\lambda} \iint_{\Sigma} U(\xi,\eta) \frac{e^{i\frac{2\pi}{\lambda}\sqrt{z^2+(x-\xi)^2+(y-\eta)^2}}}{z^2+(x-\xi)^2+(y-\eta)^2} d\xi d\eta \tag{3.4}$$

where $U(x,y,z)$ is the reconstructed wavefield at position (x,y,z), λ is the optical wavelength, Σ is the diffracting aperture and $U(\xi,\eta)$ is the wavefield in the aperture plane. By evaluating this integral at a range of depth positions, the three dimensional intensity and phase of the object wavefront can be reconstructed within a given sampling volume. The calculated intensity distribution provides a direct reconstruction of the object field and this constitutes the holographic imaging process.

3.3 Software Development

A key element to a holographic imaging device is the numerical reconstruction process which must be implemented in an efficient and robust manner for a given detector geometry. The direct computation of equation 3.4 is inefficient and so in practice this equation is simplified via use of the Fresnel approximation or by use of an alternate formulation of diffraction known as the Angular Spectrum (AS) method to reduce the computational burden[208]. Both approaches were implemented and characterised for the imager designed in this project and software was implemented to efficiently carry out the numerical image reconstruction process as outlined in the following section.

Typical cloud particle number densities within clouds have been observed to be upwards of a few hundred per cubic centimetre[209, 210]. For holographic sampling volumes on the order of a cubic centimetre or greater, as required to obtain statistically significant observations, this corresponds to the detection of hundreds of cloud particles or more in a single hologram. If a hologram is recorded every few seconds or even faster, this can become challenging to analyse manually. Automated analysis techniques must therefore be

developed to extract relevant observables such as the particle size distribution, ice crystal shape distribution and spatial homogeneity measures. Various computer vision techniques were implemented based on edge detection methods and intensity thresholding and a suitable software routine was developed and tested in this work.

3.3.1 Image Reconstruction Software

The reconstruction software developed in this project was designed to be modular and efficient, allowing simple adaptation to different system geometries. The relevant system parameters such as laser wavelength, sensor size, pixel size, reconstruction depth resolution, filtering and output display format can all be independently controlled in a simple manner. Both the AS and Fresnel theories of diffraction were implemented and can be selected with a switching variable in the code implementation. These implementations have different Nyquist sampling limits on the depths to which they can accurately be used for wave propagation and hence both methods have been included to provide accurate reconstructions throughout the sampling volume[211]. Including both diffraction methods also allows a trade off between the accuracy of the reconstruction and efficiency as discussed below. This code, as implemented in Matlab, is included in Appendix A.

The Angular Spectrum method is an alternate formulation of diffraction that provides exact reconstructions within the standard assumptions made in scalar diffraction theory. The AS diffraction theory leads to the following result for the calculation of a diffracted wave

$$\begin{aligned} U(x,y,z) &= \iint_{-\infty}^{+\infty} U(x,y,0) e^{i\frac{2\pi}{\lambda}\sqrt{1-(f_x\lambda)^2-\left(f_y\lambda\right)^2}}\, dxdy \\ &= \mathrm{FFT}^{-1}\{\mathrm{FFT}\{U(x,y,0)\} e^{i\frac{2\pi}{\lambda}\sqrt{1-(f_x\lambda)^2-\left(f_y\lambda\right)^2}}\} \end{aligned} \tag{3.5}$$

where $U(x,y,z)$ is the diffracted wavefront at arbitrary depth z, $U(x,y,0)$ is the complex wavefront in the aperture plane, f_x and f_y are the spatial frequencies and FFT is the two dimensional Fast Fourier Transform.

The Rayleigh-Sommerfeld diffraction theory can be simplified by use of the Fresnel approximation to give

$$U(x,y,z) = \frac{e^{i\frac{2\pi z}{\lambda}}}{i\lambda z}\iint_{-\infty}^{+\infty} U(\xi,\eta)e^{\frac{i2\pi\left[(x-\xi)^2(y-\eta)^2\right]}{2\lambda z}}d\xi d\eta$$
$$= \frac{e^{i\frac{2\pi z}{\lambda}}}{i\lambda z}\mathrm{FFT}\{U(\xi,\eta)e^{\frac{i2\pi\left[(x-\xi)^2(y-\eta)^2\right]}{2\lambda z}}\} \tag{3.6}$$

where ξ and η are the co-ordinates in the hologram plane and the other symbols are defined as above. It can be shown that the reconstructed pixel size varies as a function of depth and hence the output image must be scaled for simple comparison between different reconstructed depths and this has been implemented in the developed software.

To determine which diffraction theory should be implemented for a given system geometry, it is necessary to consider the limitations imposed by the Nyquist sampling theory. It can be shown that the Angular Spectrum propagation kernel will be adequately sampled for propagation depths satisfying the following relation[211]

$$z \leq \frac{N\Delta x\sqrt{(N\Delta x)^2 - \lambda^2 N^2}}{\lambda N} \tag{3.7}$$

where z is the propagation depth, N is the number of pixels in a row or column, Δx is the pixel size and λ is the wavelength. This constraint imposes an upper limit on the propagation depth to which the Angular Spectrum method can be used to avoid aliasing of the reconstruction.

Due to the scaling with depth of the reconstructed Fresnel diffraction pattern, at short propagation distances the reconstructed image becomes undersampled and hence it can be shown that the Nyquist sampling condition is given by[211]

$$z \geq \frac{N\Delta x^2}{\lambda} \tag{3.8}$$

where the variables are defined as above. The constraints imposed by equations 3.7 and 3.8 suggest that both implementations of diffraction are required, dependent on the size of the sampling volume. The sampling volume for this system can be varied and so to ensure that the reconstruction obeys the Nyquist limits for all sampling depths, both diffraction theories have been implemented in the developed software. The AS method is an exact theory whereas the Fresnel approximation will introduce sizing errors for particles that do not satisfy the Fresnel condition; however, for typical cloud particle sizes, accurate results are

Angular Spectrum Diffraction	Fresnel Diffraction
Exact theory	Approximate theory
Short propagation distances	Large propagation distances
Computation of two FFT's	Computation of one FFT
Reconstructed image extent same at all depths	Reconstruction image extent scales with depth

Table 3.1 Differences between the Angular Spectrum diffraction method and Fresnel diffraction method.

still obtained[211, 212]. The calculation time for each approach is relatively fast due to the efficiency of the Fast Fourier Transform (FFT); however, the AS method is less efficient as it requires two such operations as opposed to one for the Fresnel method. These differences are summarised in Table 3.1. Despite the efficiency of the algorithms, the large array sizes to be reconstructed for typical camera pixel grids still impose significant constraints on the feasible number of reconstruction depths possible for real time analysis. This can readily be improved through the use of Graphics Processing Unit (GPU) based processing and parallel processing on computer clusters.

3.3.2 Holographic Imaging Simulation

Software was developed in this project to test and validate the reconstruction software and holographic theory outlined in the previous sections. The diffraction based reconstruction software was tested by simulating known input apertures in the recording plane and checking that the reconstruction software produced the known diffraction results. The holographic imaging theory was tested for the detector geometry used in this project by simulation of the hologram produced by an arbitrary set of objects and confirming that the reconstructed three dimensional image reproduced the original input object field.

The reconstruction software was validated by comparison of the generated diffraction patterns to known diffraction results for a range of simple aperture distributions. The generated diffraction from a double slit aperture is shown at a near field reconstruction distance in Figure 3.2a and a far field distance in Figure 3.2b. A vertical and horizontal cut is included adjacent to the full diffraction image to compare directly with the analytical diffraction results. These diffraction patterns agree with the expected results in both the Fraunhofer and Fresnel limiting diffraction regimes and similar agreement was seen for

the other apertures tested such as the square aperture and circular aperture. The near field result shows the two slits acting essentially as independent sources of light with diffraction at their edges. As the observation distance increases, the spreading of the light results in more overlap between the light sources and hence the well known double slit interference pattern is seen to emerge in the far field. This validation provides confidence in the reconstruction software developed; however, further experimental testing was performed to further validate the software as outlined in the following chapter.

A key feature to note in the generated diffraction patterns is that the number of pixels and pixel sizes of the reconstructed image directly affects the image reconstruction quality. This can be seen in the jagged appearance of the generated diffraction pattern in Figure 3.2b towards the edge of the image. The fringe spacing decreases as a function of distance from the camera centre and the fringes have become under sampled towards the edges due to the coarse pixel size of the simulated camera grid. The Nyquist sampling condition is no longer maintained, leading to aliasing artefacts in the generated diffraction pattern. As the pixel size is decreased and the number of pixels is increased, the diffraction pattern is more accurately sampled and hence aliasing is avoided in the reconstructed image. The downside with sampling more finely is the significant increase in computation time and hence there will always be a trade off between these effects. It was found that for this project, reconstruction at the same grid resolution as the camera grid led to no violation of the Nyquist sampling constraint for typical cloud particle sizes and reconstruction distances within the sampling volume; however, this optimisation would need to be considered for systems with a larger sampling volume.

To independently validate the holographic imaging theory for the detector geometry designed in this project, software was written to first simulate a hologram produced by an arbitrary set of objects recorded on a camera pixel grid and then the independently validated reconstruction software was used to reconstruct the three dimensional image according to the theory outlined above. The simulation used the physical parameters of the developed imaging device such as laser wavelength, pixel size, camera size, reference wavefront curvature and laser power. The hologram was constructed by use of equation 3.2 where the phase difference term between the spherical reference wave and spherical scattered waves from the point source objects was calculated by use of the analytical result for diffraction from a point source in the geometric optics limit[213]

$$\phi\left(x,y\right)=\frac{2\pi}{\lambda}\left(\frac{x_o x}{z_o}+\frac{y_o y}{zo}-\frac{x^2+y^2}{2z_o}\right) \tag{3.9}$$

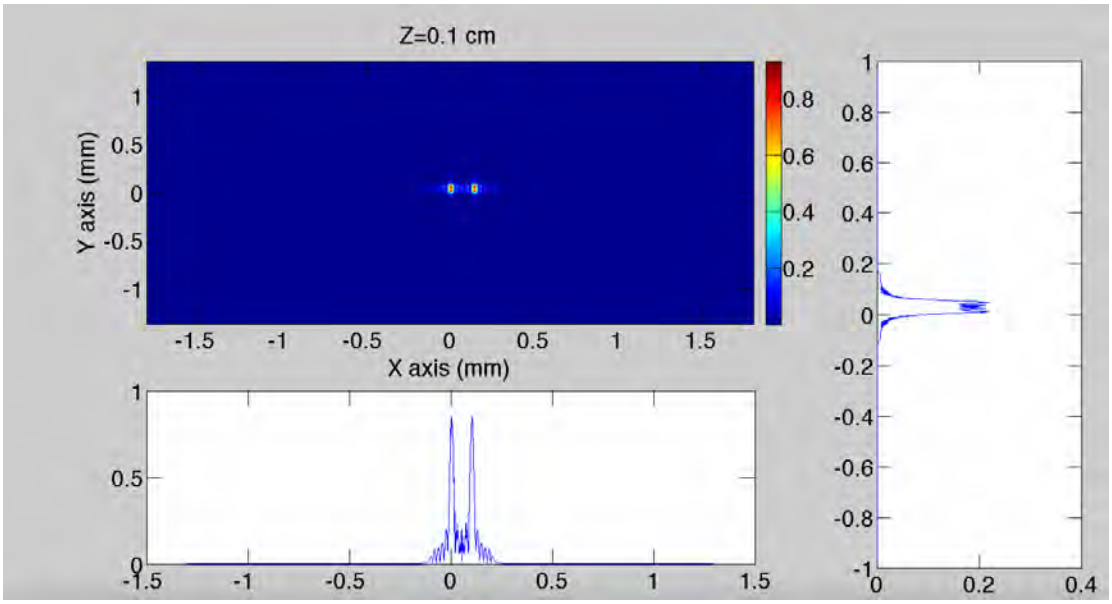

(a)

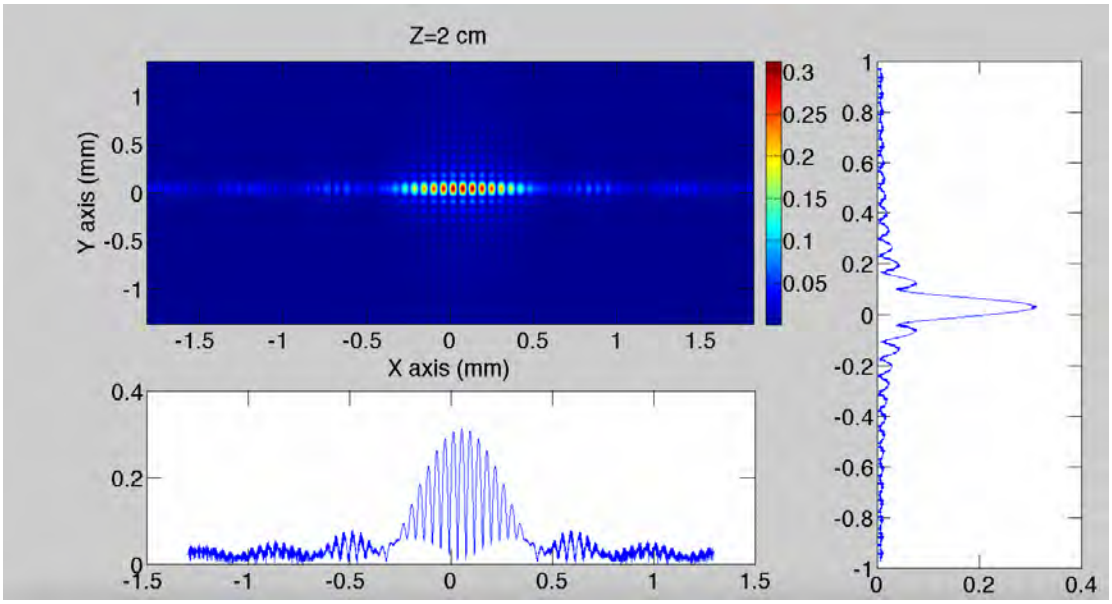

(b)

Fig. 3.2 Generated double slit aperture diffraction patterns using the reconstruction software for: (a) a near field observation distance and (b) a far field observation distance.

where x, y are the camera pixel grid co-ordinates, λ is the laser wavelength and x_o, y_o, z_o are the three dimensional co ordinates of the point source object. A hologram of an arbitrary object distribution can then be simulated by superposition of these individual point source diffraction terms.

A simple point source object distribution is shown in Figure 3.3 where two point sources are placed at a distance of 1cm from the camera, one is placed at a distance of 1.2cm and another is placed at 1.4cm. The hologram for this object distribution was then computed and the reconstructed object wave intensity was calculated at a range of depth positions, as shown in Figure 3.4. It can be seen that all of the original objects have been successfully reconstructed at their correct three dimensional positions. The reconstructed intensity at a depth where no objects were placed is included in the fourth panel of Figure 3.4 to show the clear discrimination between the in focus reconstructed objects and the out of focus diffraction patterns at depths which do not correspond to the true object locations.

3.3.3 Automated Analysis Software

The sampling volume of a holographic instrument can be on the order of a cubic centimetre or larger and for typical cloud particle number densities, a given hologram can contain information about hundreds of cloud particles. If a hologram is recorded every few seconds, this can become challenging to analyse manually and hence automated analysis methods must be used to extract the microphysical observables such as the particle size distribution, particle shape distribution and spatial clustering information. A number of approaches have been suggested to overcome this issue, including the use of neural networks and computer vision algorithms; however, the optimum solution to this problem remains open[214–218]. In this work a set of computer vision algorithms[219–223] were implemented and tested based on intensity thresholding, edge detection and the Hough transform[224] for the identification of spherical particles.

The software begins by calculating the reconstructed three dimensional image intensity from a recorded hologram at a specified range of depth positions by use of the theory outlined in the previous section. The reconstructed three dimensional image is then stored as a 3D array and the maximum intensity as a function of depth is calculated at each image pixel position. This maxima operation makes use of the result that the in focus image of a reconstructed object will correspond to a maximum in intensity[225]. An intensity threshold is then applied to this maximum intensity 2D projection image to separate real particles from background noise and out of focus interference fringes. Otsu's method[226] was applied to automatically calculate a suitable value for this threshold; however, it was found that to completely remove the background contributions, a larger threshold was required dependent

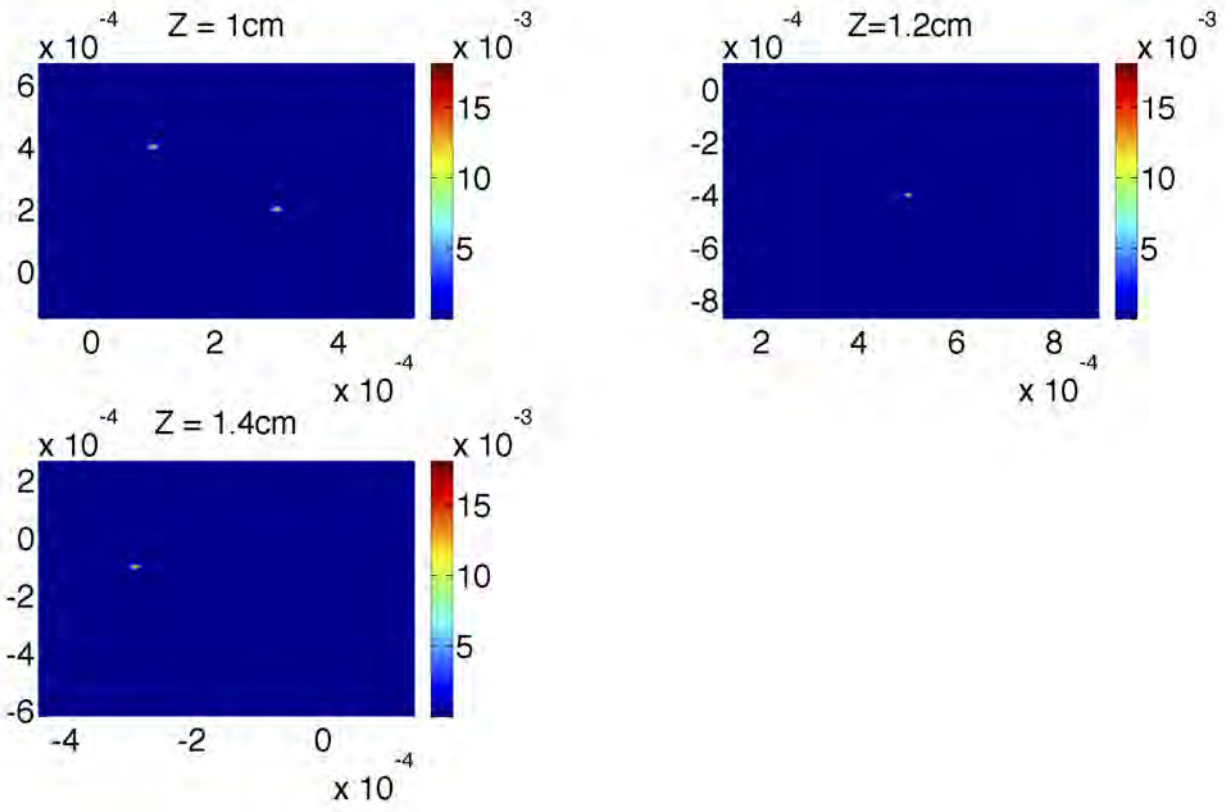

Fig. 3.3 Simulated three dimensional object distribution for validation of the holographic imaging theory for the detector designed in this project. The colour bar shows the image intensity and the x and y axes are the physical size of the camera grid in units of metres. Two particles are placed at a depth of 1cm from the camera, one is located at a depth of 1.2cm and another is placed at a depth of 1.4cm.

on the object size. Further testing is therefore required with real cloud particles in the field to better constrain the choice of this threshold but for the purpose of this work, a suitable limit was selected manually.

Once the particles have been separated from the background, the algorithm individually loops over each identified particle to be processed. The in focus particle image is saved by applying the edge detection algorithm to the image to identify the extent of the particle, and to separate potentially nearby particles, at the corresponding depth position of the maximum intensity identified in the previous stage. This image is then binarised and the particle size and shape parameters such as the Circularity Factor (CF) are calculated where CF is defined by the relation

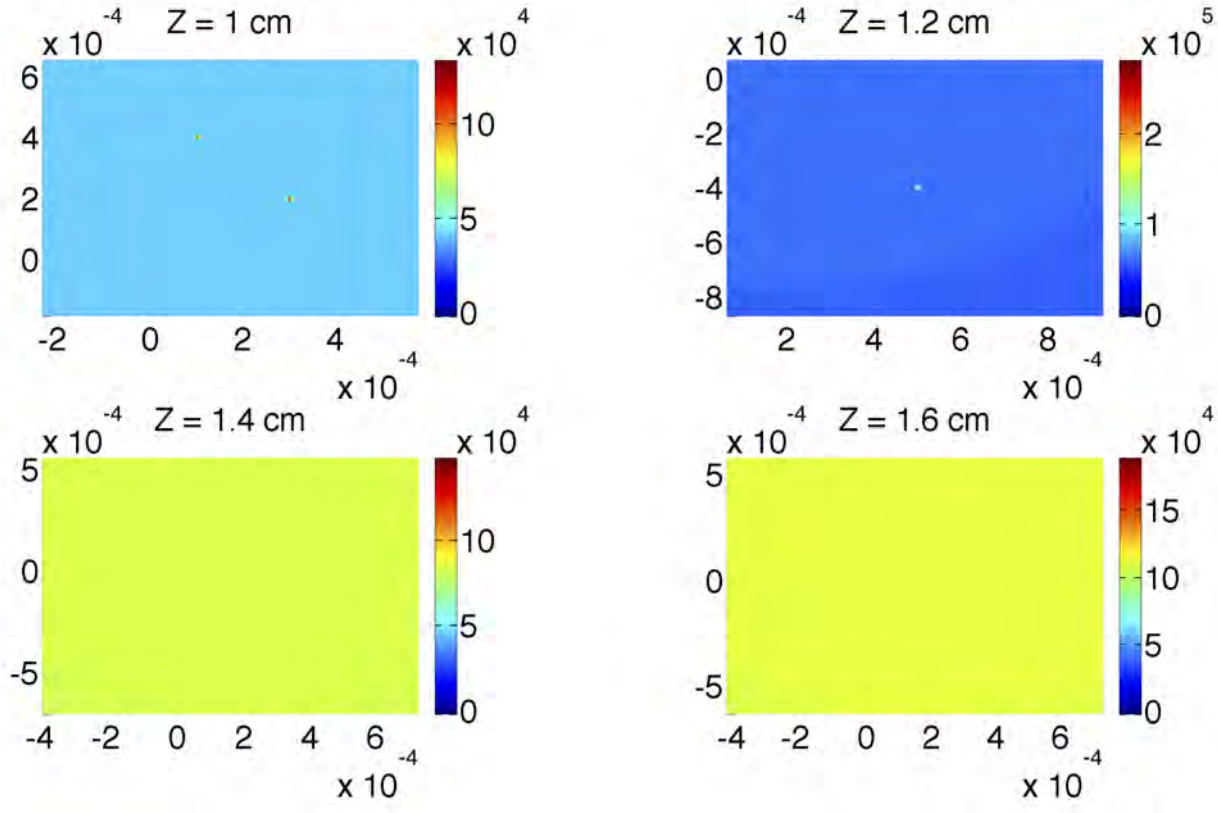

Fig. 3.4 Reconstructed object wavefront at a range of depth positions. The original object field has been reconstructed successfully at the appropriate depths of 1cm, 1.2cm and 1.4cm. The field at 1.6cm highlights the clear difference between true reconstructed objects and out of focus background diffraction terms.

$$CF = \frac{4\pi A}{P^2} \tag{3.10}$$

where A is the particle area and P is the perimeter determined by counting the number of pixels in the binary image. By looping over each identified particle in the image, a histogram can be constructed to display the microphysical properties such as the particle size and shape distributions. The performance of this algorithm was tested experimentally as discussed in Chapter 4.

3.4 Resolution and Design Constraints

The resolution of an imaging system is a limit on the smallest unambiguously resolvable object that the system can reliably record in an image. Given the ambiguity in defining what is meant by a resolved object, there are a range of definitions and criteria that can be used to constrain the performance of a given imaging system. The major factors that contribute to the overall image resolution in a holographic system are the spectral response of the camera, image compression, number of interference fringes recorded, the limit imposed by diffraction, geometric magnification effects, sensor size, temporal and spatial coherence of the light source, exposure time and image noise. These major sources of uncertainty have been characterised for this instrument as summarised in the following discussion and suitable components were selected that provide a balance between a low cost and optimal performance based on these constraints.

Modern low cost cameras such as webcams typically have a Bayer colour filter placed over the sensor array to generate colour images. This bayer pattern means that a given set of four pixels will have two sensitive to green light, one to red and one to blue. As a result of this geometry, a maximum of only half the overall number of pixels are available for recording light of a single wavelength produced by a laser source and this can significantly degrade the image resolution. A method was developed for removing this colour filter array using an abrasive technique and a microscope and the results of this technique are shown in Figure 3.5. The sensor has been illuminated by a red LED with a narrow frequency distribution. The left side of the image has had the colour filter removed and the intensity is relatively uniform with all of the pixels responding to the incident light. The right side of the image has the original colour filter in place and only a quarter of the pixels are sensitive to the input light as expected. This improved resolution highlights the need for a monochrome camera to be used, either by conversion of a low cost colour filter camera or by direct purchase of a more expensive monochrome camera.

The output format of the camera is important when determining the resolution of a given camera system, as various levels of compression will reduce the information content of the dataset. Some lower cost cameras only allow images to be output in a compressed format such as JPEG rather than the raw file format containing the full sensor information. Compressed files have the advantage that due to their small file size, an order of magnitude increase in the number of images stored on a given hard drive can be achieved whilst also allowing the use of cheaper commercial grade cameras that do not support the raw output format. Typical holograms with spatial frequencies appropriate for the measurement of cloud particles were recorded with both JPEG and raw output formats. It was found that for typical cloud particle sizes and depth positions, the produced interference patterns were not faithfully preserved in

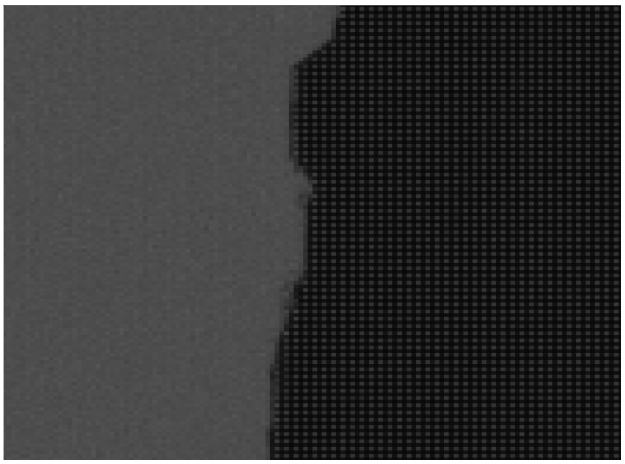

Fig. 3.5 Spectral response at a single wavelength with the colour filter on the sensor (right of image) and with the filter removed (left of image).

a compressed image output and hence the full raw format files were required. This effect is demonstrated in Figure 3.6. A noticeable decrease in the total number of interference fringes resolved is seen in the compressed JPEG image with a corresponding decrease in resolution of the reconstructed three dimensional image.

The number of interference fringes recorded in a hologram directly relates to the resolution of the reconstructed image[211]. The spatial extent and depth information of a particle is encoded in the spacing of the interference fringes along with the spatial intensity modulation of the fringe pattern[227]. If too few fringes are recorded, information about the phase of the object wavefront is lost and hence the three dimensional object position cannot be reconstructed accurately. For particles in a far field in line holographic geometry, such as the one used in this project, the fringe spacing of light diffracted from a spherical particle can be shown to obey the following relation[228]

$$\delta r = \frac{2Ma}{1+m} \tag{3.11}$$

where δr is the fringe spacing, M is the system magnification, a is the particle radius and m is the fringe order. A minimum of three interference fringes is generally accepted as being sufficient for accurate image reconstruction[199]; however, as the number of fringes increases so too does the accuracy of the image reconstruction. This criteria suggests a sensor must be chosen with a pixel size that is smaller than this fringe spacing for a given particle size of interest to obey the Nyquist sampling limitations and an overall sensor size

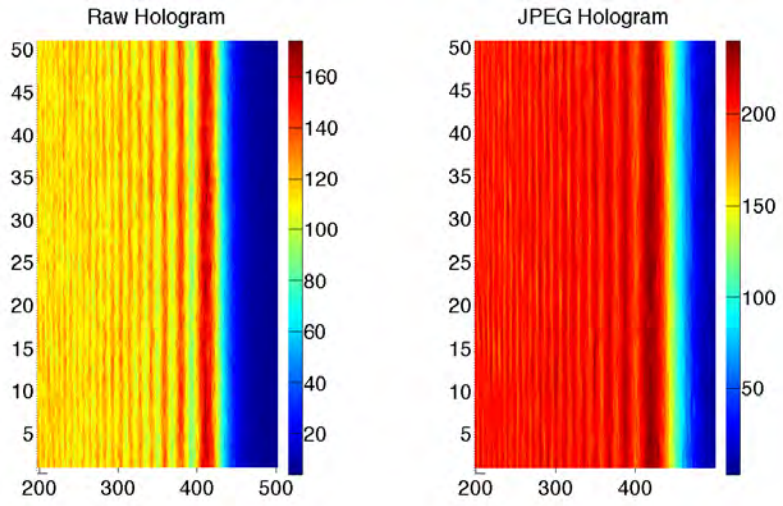

Fig. 3.6 The left image shows the hologram recorded in the uncompressed raw file format, the right image shows the output using JPEG compression. A clear reduction in the overall number of resolvable interference fringes is observed in the compressed output.

large enough to accommodate at least three interference fringes for objects throughout the sampling volume. A detectable particle size of 5 microns was aimed for with this instrument to coincide with the size of typical water droplets in a cloud and hence suitable cameras were investigated with small pixel sizes to accommodate this goal.

A point source spherical object will produce a diffraction pattern, or in line hologram, that scales in extent as the spacing between the object and the camera is varied. The superposition of diffraction patterns produced with a spherical wave source from two adjacent point source particles can be modelled via the following expression

$$I = 2\sqrt{I_1 I_2}\cos\left\{\frac{2\phi_0 - \phi_1 - \phi_2}{2}\right\}\cos\left\{\frac{\phi_1 - \phi_2}{2}\right\} \tag{3.12}$$

where:

$$\phi_0 = \frac{2\pi}{\lambda}\left\{\sqrt{x^2 + D^2}\right\}$$
$$\phi_1 = \frac{2\pi}{\lambda}\left\{\sqrt{x^2 + d^2} + (D - d)\right\}$$
$$\phi_2 = \frac{2\pi}{\lambda}\left\{\sqrt{(D-d)^2 + t^2} + \sqrt{d^2 + (x-t)^2}\right\}$$

and the other variables are defined according to Figure 3.7. This representation suggests that the second modulation term in the equation contains information about the spacing of adjacent objects (t) and hence by requiring that this modulation is adequately sampled, a

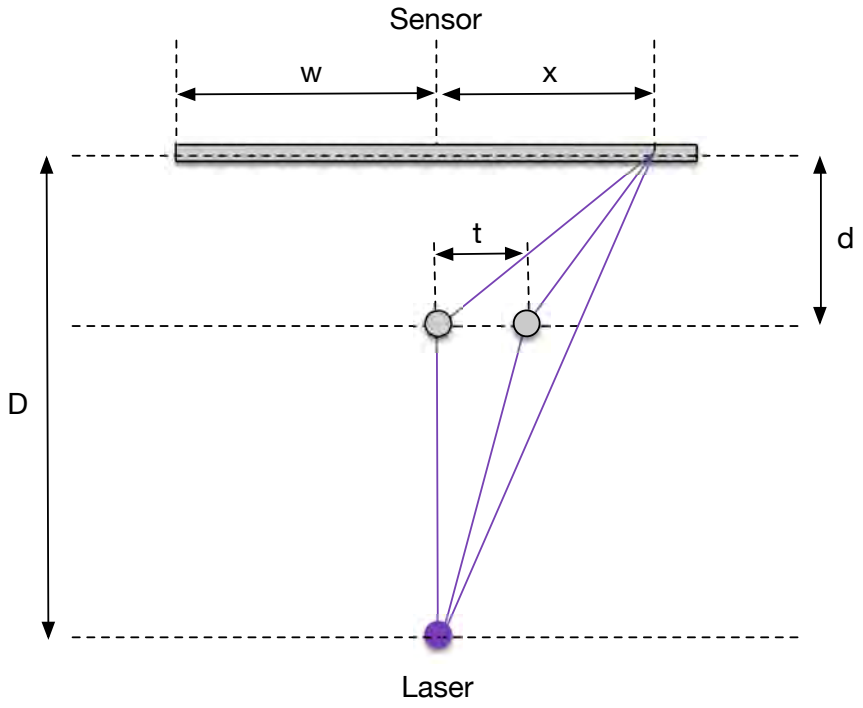

Fig. 3.7 Geometry used in the resolution simulation. Figure adapted from Jericho et al. (2006).

direct limit on the resolution can be determined[229]. A one dimensional cut of the simulated hologram is plotted as a function of particle distance from the sensor in Figure 3.8 and it can be seen that at larger particle depths, fewer modulation cycles are recorded on the sensor suggesting a loss of information. This criteria suggests that a smaller geometric magnification is actually preferable in a given system as this will allow more modulation fringes to be recorded; however, magnification is still useful to overcome the fringe spacing limit imposed by equation 3.11.

By requiring that the first modulation minimum be recorded on the sensor surface, it can be shown that the standard diffraction limit of a conventional microscope also applies to a holographic imager as given by the relation[51, 230]

$$\begin{aligned} D_{\text{res}} &\geq \frac{\lambda}{2\,(\text{NA})} \\ &\geq \frac{2.44\lambda z}{D} \end{aligned} \tag{3.13}$$

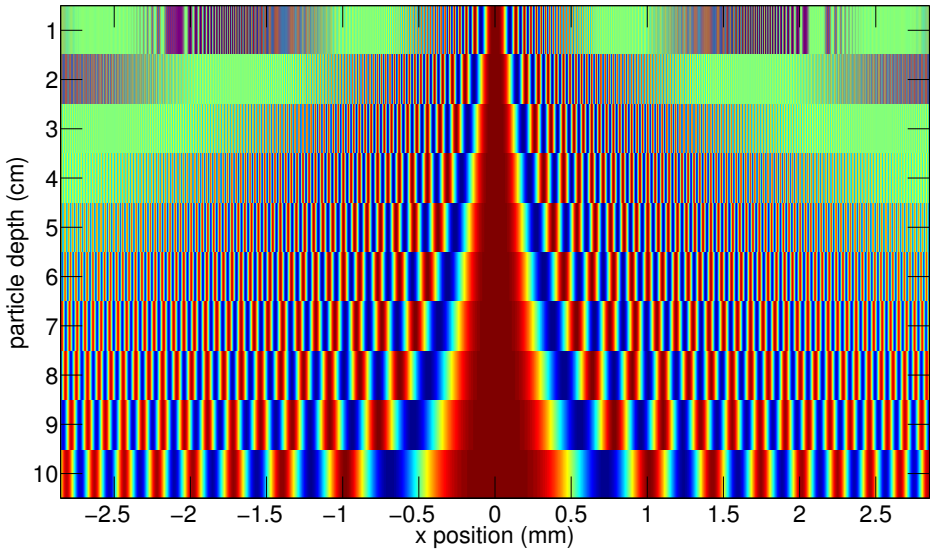

Fig. 3.8 One dimensional simulated hologram from adjacent point source scatterers as a function of particle distance from sensor. Note that at larger distances, information about the interference modulation is lost.

where NA is the numerical aperture of the detector, D_{res} is the smallest resolvable particle diameter, z is the depth of the object relative to the camera sensor and D is the camera sensor size. A similar relation can be derived for the depth resolution as given by

$$Z_{\text{res}} \geq \frac{\lambda}{2\,(\text{NA})^2} \tag{3.14}$$

where Z_{res} is the depth resolution. These relations imply that the ultimate diffraction limited resolution of the system is dependent on both the laser wavelength and the size of the sensor used, where optimum resolution is achieved with a short laser wavelength and large sensor area. For this reason, a L405P20 laser diode with a centre wavelength of 405nm was selected for this instrument as it provided the best trade off between short wavelength, relatively high beam quality and low cost. The depth resolution goes as the inverse square of the numerical aperture whereas lateral resolution scales inversely with the numerical aperture. A given holographic system will therefore have a poorer depth resolution than the lateral resolution. The overall resolution also scales proportionately with the axial distance of the object from the camera sensor and hence this must be considered when calculating

Camera Feature	See3 Camera	Raspberry Pi Camera
Pixel Size	2.2 μm	1.4 μm
Sensor Size	5.7mm x 4.3mm	3.7mm x 2.7mm
External Triggering	Yes	No
Frame Readout	Global Reset Release	Rolling Shutter
Pixel Bit Depth	12 bpp	10 bpp

Table 3.2 Comparison between the See3 camera and Raspberry Pi camera features.

observables such as the particle size distribution throughout a given sampling volume to avoid statistical biasing of the results.

The sampling constraints imposed by equations 3.7 and 3.8 and resolution limits from equations 3.11 and 3.13 are plotted for the two main cameras considered in this project, the Raspberry Pi camera (RPICam) and the See3Cam_CU51 (See3Cam), in Figure 3.9. The diffraction limit for the See3Cam is significantly better than the RPICam due to the larger sensor extent. The lower resolution limit imposed by the pixel size is slightly smaller for the RPICam; however, this is only relevant for object depths less than roughly 1cm at which point the diffraction limited resolution becomes dominant. The See3Cam was selected for use in this project due to the superior resolution throughout the sampling volume which begins at a depth greater than 1cm from the sensor. This camera also allowed external triggering with a global shutter acquisition mode which was necessary for minimising motion blur in recorded images. The differences between these cameras are summarised in Table 3.2.

This instrument is intended for use on a weather balloon and hence blurring effects due to the motion of the balloon must be considered in the design of the system. The required image exposure time for a given amount of blurring can be calculated from the relation

$$\delta t = \frac{D}{fv} \tag{3.15}$$

where δt is the required exposure time, D is the particle size of interest, f is the percentage of blurring relative to the particle size and v is the relative velocity between the particle and the sensor. For typical weather balloon ascent rates of 5 m/s and a tolerable motion blur of 10% of the particle size, a 15 micron cloud particle will require an exposure time that is no greater than 300ns. This constraint can be relaxed somewhat if magnification is included and when sampling on a stationary ground based structure due to the typically lower particle velocities relative to the stationary camera.

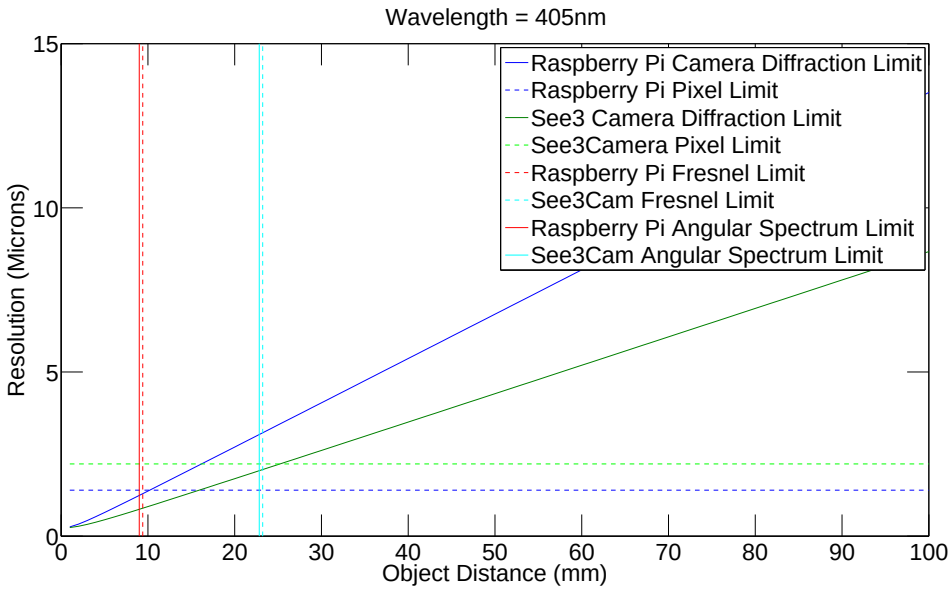

Fig. 3.9 Resolution and sampling limit comparison between Raspberry Pi and See3 cameras. Resolution is the size of the smallest resolvable particle and object distance is defined relative to the camera sensor. Vertical lines show the sampling limits for each diffraction implementation.

Multiple interference fringes from each particle must be recorded to adequately reconstruct a three dimensional image. This requires that the interference fringe visibility be greater than the noise floor of the system. Fringe visibility is dependent on the shape and size of the scattering particle, along with the temporal and spatial coherence properties of the illumination source[228]. Low cost laser diodes were selected for use in this system, with relatively low coherence lengths. This required an in line geometry to be used, with the camera, laser and sampling volume collinear with each other, to minimise the path length differences between scattered object wavefronts and unscattered background light and hence maximise the interference fringe visibility. This geometry is illustrated in Figure 3.10 for this system. The in line configuration has the advantage that the interference fringes have the greatest fringe spacing of any recording geometry[213] and hence the relatively coarse pixel spacing of the camera sensor is less of a problem. This configuration is also less sensitive to vibration blurring effects and does not require extra optical components such as lenses and beam splitters which would add significant cost and alignment challenges to the system. A key disadvantage of the in line geometry is the overlap between the reconstructed particle image and the out of focus twin image as described by equation 3.3. This twin image can obscure information about the phase and fine structure of the reconstructed object wavefront;

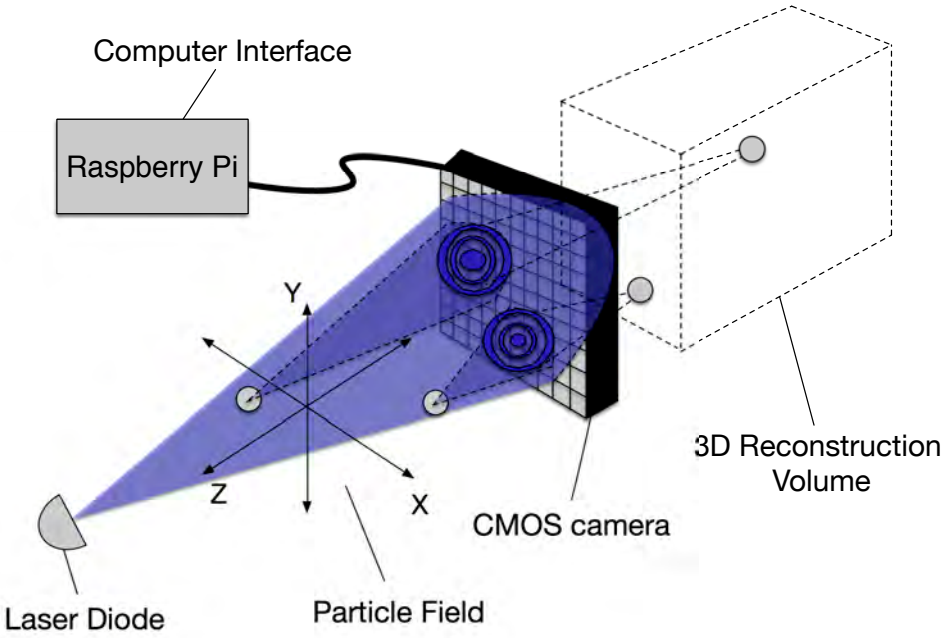

Fig. 3.10 Summary of the in line recording geometry used in this system. The laser, sampling volume and camera are collinear and holograms are recorded by a low cost Raspberry Pi computer for further processing and analysis.

however, numerical techniques have been developed to reduce the effect of this issue. The twin image term is in focus at an equal depth position as the reconstructed particle image but on the other side of the sensor. Due to the relatively small cloud particle sizes, relative to their separation from the sensor, this causes the twin image to be spread over a large area in the reconstructed image plane and hence this is not a major concern for cloud particle studies.

The image reconstruction process is sensitive to the wavelength of the light used to record the image. If this wavelength is not correctly specified in the code, there will be a corresponding angular magnification of the image proportional to the ratio of the reconstruction wavelength to the recording wavelength. It is therefore important to either actively measure this laser wavelength as a function of time or control the parameters that affect the wavelength such that it remains constant at a known value.

The wavelength of a laser diode can be affected by temperature due to thermal expansion effects of the gain medium. This dependence could not be measured directly for the L405P20 diode used in this project as the available spectrometer was not sensitive to wavelengths below 445nm. As an alternate approach, the dependence was taken from the L405P20

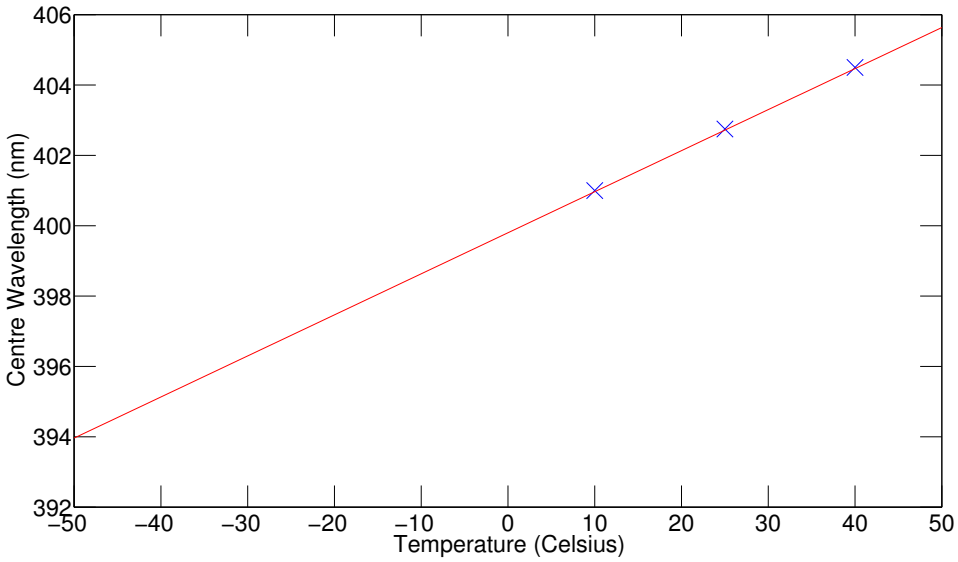

Fig. 3.11 Temperature dependence of the L405P20 laser diode as extrapolated from datasheet values.

datasheet which provides centre wavelength measurements at three different temperatures as shown by the blue crosses in Figure 3.11. The central wavelength at other temperatures was then calculated by assuming a linear dependence; however, the results are only approximate as this analysis does not take into account effects such as mode hopping. The slope of this fit is approximately 0.1 nm per degree. For a reconstruction wavelength of 403nm, the quoted value at room temperature from the datasheet, a wavelength change of 4nm will correspond to a change in angular magnification of 1.1% in the reconstructed image. This corresponds to a temperature change of 40 degrees Celsius and should be accounted for given that cloud temperatures can be more than 50 degrees below room temperature. This can be achieved by either controlling the laser temperature actively or by measuring the laser temperature and applying a temperature correction in software. Both approaches were implemented in this project as discussed in the next chapter.

The theoretical resolution constraints outlined above are useful in the design and selection of components for a given system; however, the overall resolution of the system is made complicated by various other factors such as shot noise, fringe visibilities dependent on the scattering target shape, chromatic aberration due to the laser bandwidth, interference fringe backgrounds from multiple reflections in the sampling windows and wavefront distortion in the low quality laser diode beam. These effects are clear in Figure 3.12 which shows the comparison between the simulated hologram for a spherical point source particle and the

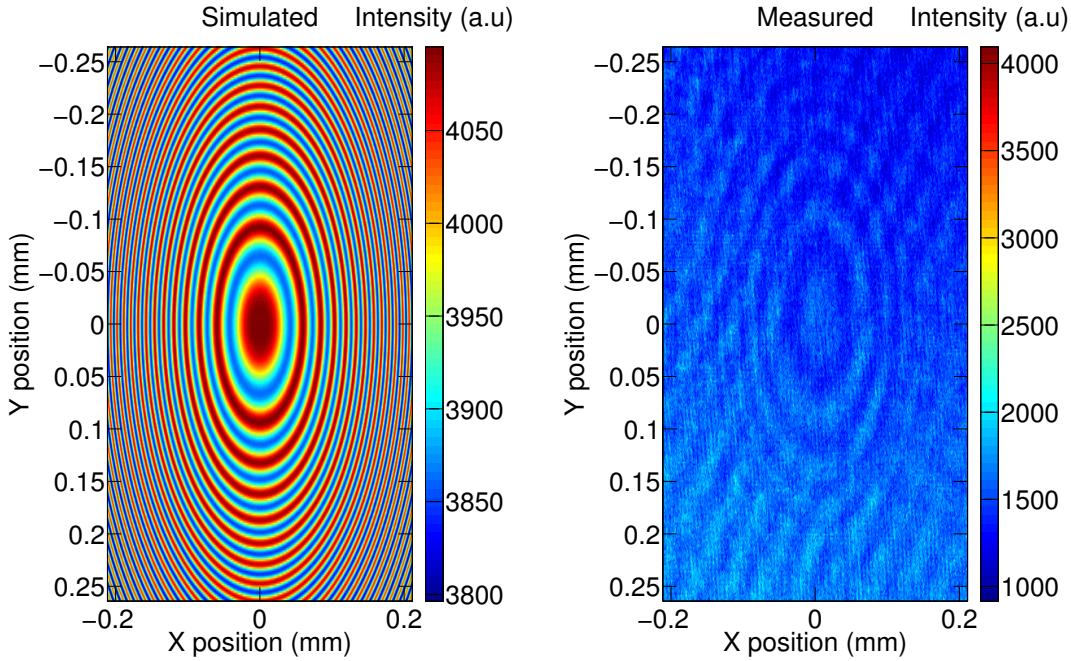

Fig. 3.12 Comparison between the simulated hologram of a spherical point source (left) and experimental measurement of the hologram of a spherical scattering particle recorded under the same conditions (right).

recorded hologram from a calibration test sphere recorded with the same wavelength and depth positions as the model. The properties of the hologram such as the fringe spacing agree well; however, the experimental results show that far fewer interference fringes have been recorded before the fringe visibility becomes comparable to the noise floor of the system. As a result of these more complicated noise effects, the resolution of the system must be characterised experimentally using known standards such as calibration spheres and USAF resolution test charts as summarised in the next chapter.

Chapter 4

Instrument Characterisation

4.1 Introduction

The resolution and overall performance of a holographic imaging system depend on many factors and in practice the performance aspects must be measured experimentally and characterised for a given system. The performance and stability of the system depend on non ideal effects, not considered in the analysis of the previous chapter, such as laser spectral width, laser central wavelength, laser intensity, laser pulse properties, sensor noise, performance of the temperature controller, condensation effects, system stability and enclosure properties. In this chapter the results of experimental testing of the performance and resolution of the system will be presented, along with an overview of the hardware systems that were designed and developed as guided by the analysis in the previous chapter.

4.2 Electro-optical Performance

Two laser diodes were selected for use in this project; a 405nm wavelength L405P20 (L405) and an 830nm wavelength HL8325G (L830). The L405 was selected primarily to provide the best diffraction limited resolution and the L830 was chosen for its larger power, allowing larger sampling volumes at the cost of a poorer resolution. To minimise motion blur in the recorded images, a global reset release sensor was selected which requires careful synchronisation between the laser pulse duration and the camera exposure time. The spectral and electrical properties of these diodes are characterised in this section along with the laser pulsing performance.

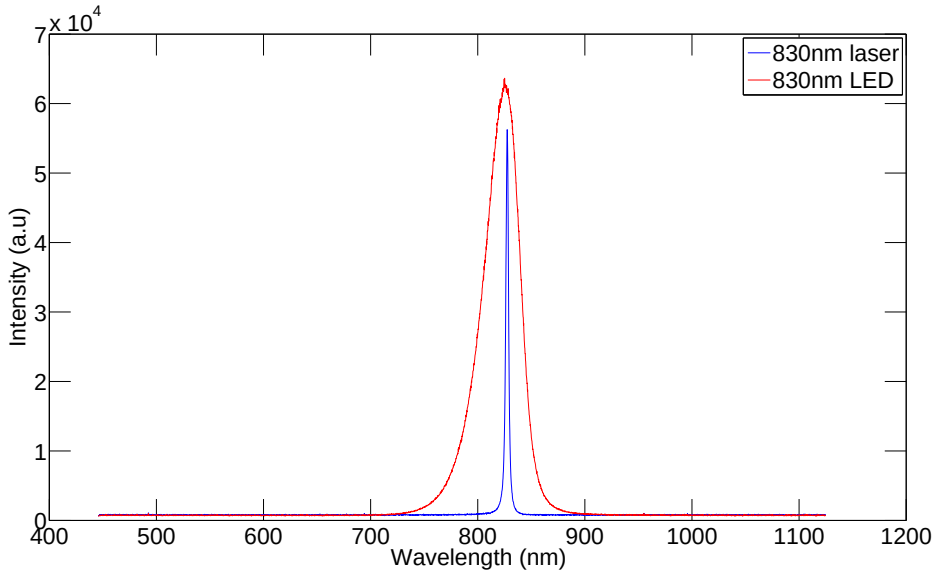

Fig. 4.1 Intensity spectrum for the L830 laser diode along with an 830nm LED for comparison.

4.2.1 Laser Diode Characterisation

The laser intensity spectrum was measured using an Ocean Optics USB4000 spectrometer. The spectrometer cannot be used for wavelengths below 445nm and hence only the L830 spectrum could be measured as shown in Figure 4.1. The blue trace shows the laser diode spectrum and the red shows the spectrum of an 830nm LED that was also considered for use as a light source. The coherence length defines the path difference between light beams that results in a drop of coherence by a factor of 1/e and is defined by the relation

$$L_c = \frac{\lambda^2}{\pi \Delta\lambda} \tag{4.1}$$

where λ is the laser peak wavelength and $\Delta\lambda$ is the Full Width Half Maximum (FWHM) of the spectrum. The peak wavelength of the L830 was 827.5nm and the FWHM was 2.9nm which corresponds to a coherence length of 75 microns. This is on the order of the size of large ice crystals and so for an inline geometry that minimises the path difference between beams, a suitable interference pattern is expected. The coherence length of the LED was only 5.7 microns which is smaller than most ice crystals and hence the more expensive laser diode was required for use in this project. Similar results were obtained for the L405 based on the peak wavelength and spectral width values obtained from the datasheet.

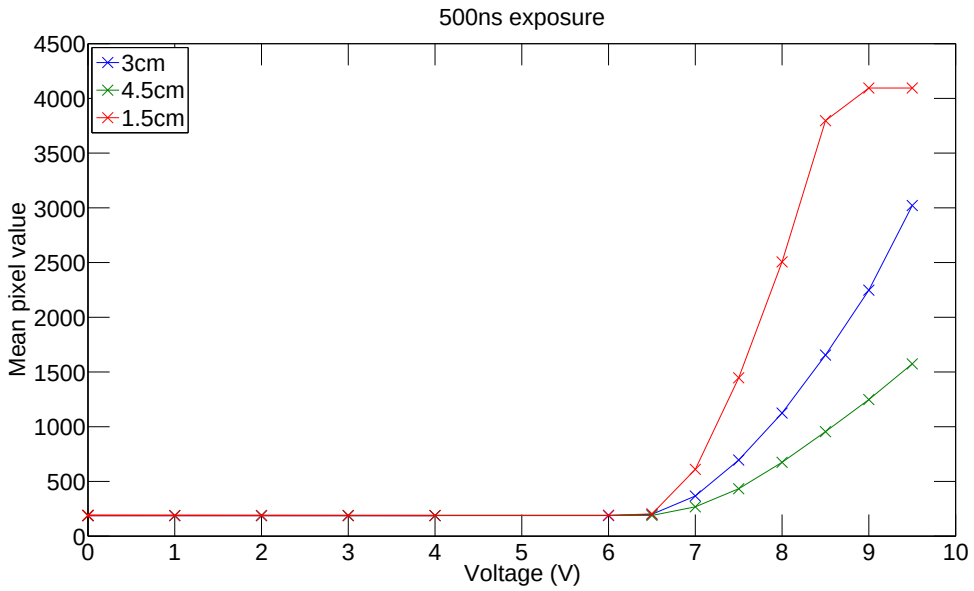

Fig. 4.2 Mean camera pixel value for illumination from the L405 laser diode as a function of applied voltage to the laser diode driver circuit and distance between the laser and camera. Measurements are taken with a 500ns exposure time.

The mean pixel value recorded by the See3Cam for direct illumination from the laser diodes was measured as a function of input voltage to the laser diode driver circuit and distance of the laser from the sensor. The results of this testing for the L405 are shown in Figure 4.2. The pixel values represent the output from the Analogue to Digital Converter (ADC) for each pixel and provide a measure of the optical intensity incident on the camera sensor. A clear threshold behaviour is observed at approximately 6.5V, as expected for the laser diode. It was found that a minimum mean pixel value of approximately 700 was required to obtain clear interference fringes from test spheres throughout the sampling volume. Larger intensities produced clearer fringes, provided that the image did not become saturated at the maximum value of 4096 for the 12 bit pixels. The incident laser power follows the inverse square law as expected and hence the operating voltage must be varied as a function of sample volume depth to ensure that this mean image intensity criterion is met.

The mean intensity, as parametrised by the mean pixel value, is also plotted as a function of laser pulse width, a measure of the exposure time since the laser pulse is synchronised with the camera exposure, in Figure 4.3. This relationship shows the expected linear dependence of intensity on exposure time with nonlinear effects at large intensities due to saturation of the sensor and at low intensities due to the laser power falling below the noise floor of the camera. By increasing the laser pulse width, the system can be operated at a lower input

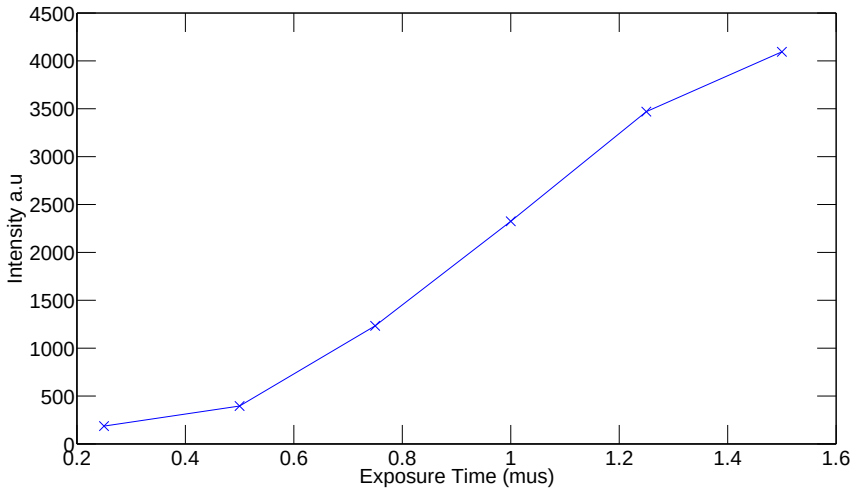

Fig. 4.3 Mean intensity as a function of exposure time measured in microseconds. Nonlinear effects are due to pixel saturation and the noise floor of the system.

voltage for a given sampling distance; however, this comes at the cost of increased motion blur in the recorded image.

4.2.2 Pulsing Characterisation

A pulsing circuit was designed to synchronise the camera exposure with the pulsed laser output as shown by the circuit diagram in Figure 4.4. Synchronisation was necessary due to the Global Reset Release (GRR) pixel readout scheme of the See3Cam in which all pixels are exposed to light simultaneously and read out individually. If light is incident on pixels at the bottom of the image whilst the top pixels have already been read out, rolling shutter streaks in the output image will be observed. As discussed in the previous chapter, the exposure time must also be on the order of hundreds of nanoseconds to minimise fringe blurring due to moving particles. The See3Cam was found to have a minimum exposure time of approximately 100 microseconds, which is significantly larger than the desired limit. The synchronisation circuit overcomes both of these issues by restricting the effective image exposure time to the duration of the laser pulse, which can be on the order of nanoseconds. The laser pulse is synchronised to occur within the exposure time of the camera and the laser pulse width then determines the effective exposure time. Since the sensor is still sensitive to background sunlight during the camera exposure time of 100 microseconds, an optical bandpass filter with a 10nm bandwidth was incorporated to only allow light from the laser diode to contribute to the image over the short laser pulse duration.

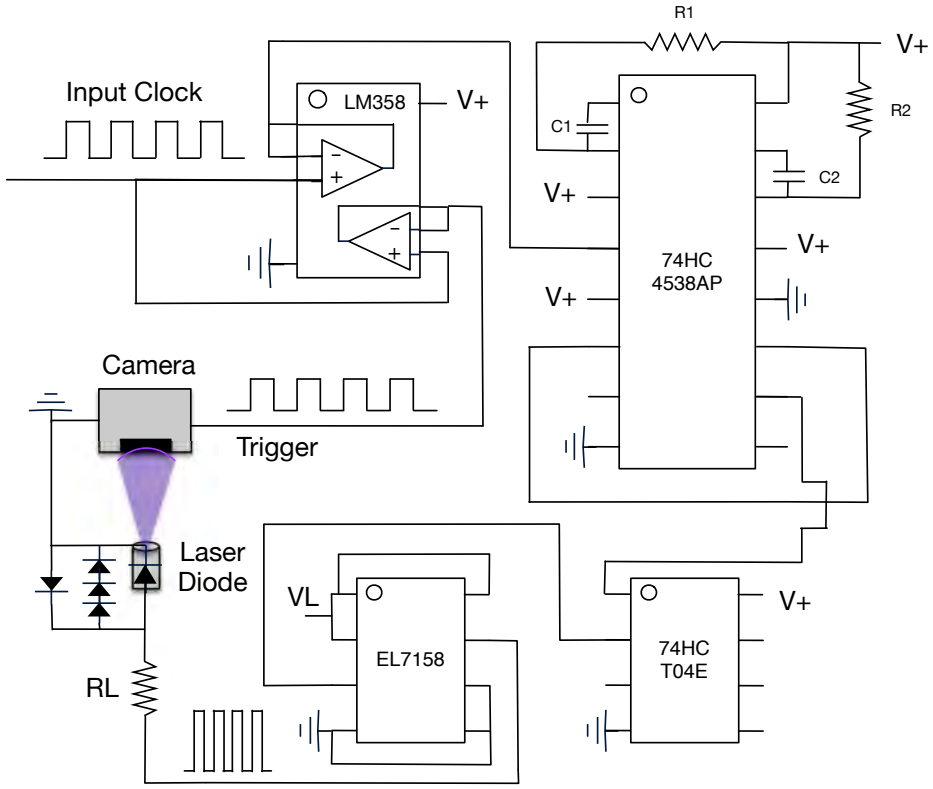

Fig. 4.4 Circuit diagram for the pulsing circuit which consists of a high speed triggering circuit and a laser pulse amplifier. The connections to the camera and laser diode are also shown to highlight the operation of this circuit.

A clock signal provided by an Arduino microcontroller or crystal oscillator is first input to the dual LM358 op amp Integrated Circuit (IC) to buffer the trigger signals. One of the outputs is sent directly to the camera trigger pin to begin the camera exposure when the clock signal goes high, allowing the camera exposure time to be set by the pulse width and the sampling rate to be controlled via the pulse repetition frequency. The other output of the LM358 is then input to a 74HC4538 dual monostable multivibrator IC. R1 and C1 can be selected to delay the output of the first monostable relative to the trigger pulse by a fixed amount. These values were selected to ensure that the laser pulse occurs halfway through the camera exposure duration. The output of the first monostable is then input to the second monostable, which produces a pulse beginning after the delay time. The pulse width can be varied by choosing R2 and C2 and pulses widths of less than 100ns were obtained using this method. The pulse polarity is then reversed using the high speed 74HCT04E inverter logic gate, as required for operation with the EL7158 MOSFET gate driver IC. This inverted pulse

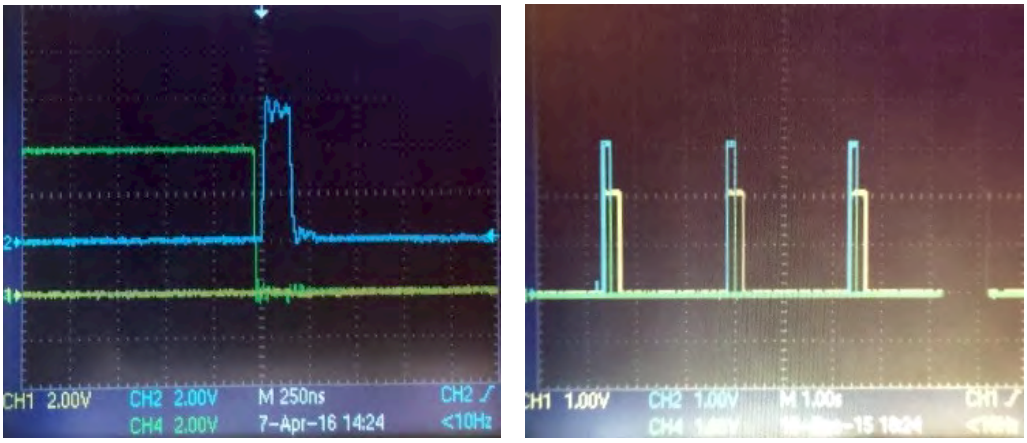

(a) (b)

Fig. 4.5 a) Oscilloscope display of the laser diode pulse shown on the blue trace and the pulse used to delay the laser pulse relative to the camera exposure pulse is shown on the green trace. b) Oscilloscope output of a train of pulses generated by the triggering circuit. The laser pulse on the green trace is synchronised to the centre of the camera exposure pulse on the yellow trace. The time between pulses determines the sampling frequency of the system.

is then amplified using the high speed EL7158 and then output to the laser diode via the load resistor (RL) which controls the laser current. Forward biased signal diodes are placed over the laser diode to clamp the laser voltage at the threshold value and to avoid transient spikes due to effects such as electrostatic discharge which could damage the laser. A reverse biased diode is also included to avoid laser damage if it is connected with the wrong polarity.

The laser diode pulse produced by this circuit is shown in Figure 4.5a. The laser diode pulse is displayed via the blue trace on the oscilloscope output and the signal delay pulse is the green trace. The laser pulse rise time was measured to be 10ns and the rise delay offset was 50ns relative to the delay pulse. The absolute timing accuracy of this circuit was therefore sufficient to ensure the laser pulse occurred within the 100 microsecond camera exposure duration. The sampling rate of the system is controlled by the pulse repetition frequency set via the Arduino clock output or a crystal oscillator. The overall sampling rate is limited by the data transfer rate of the Raspberry Pi computer interface at 2 frames per second (fps); however, this can readily be improved by use of a more powerful mini computer system. A sample pulse train is shown in Figure 4.5b which shows the camera trigger pulse on the yellow trace, the delay pulse on the blue trace and the laser pulse on the green trace. It can be seen that the laser pulse occurs in the centre of the camera exposure pulse duration as desired.

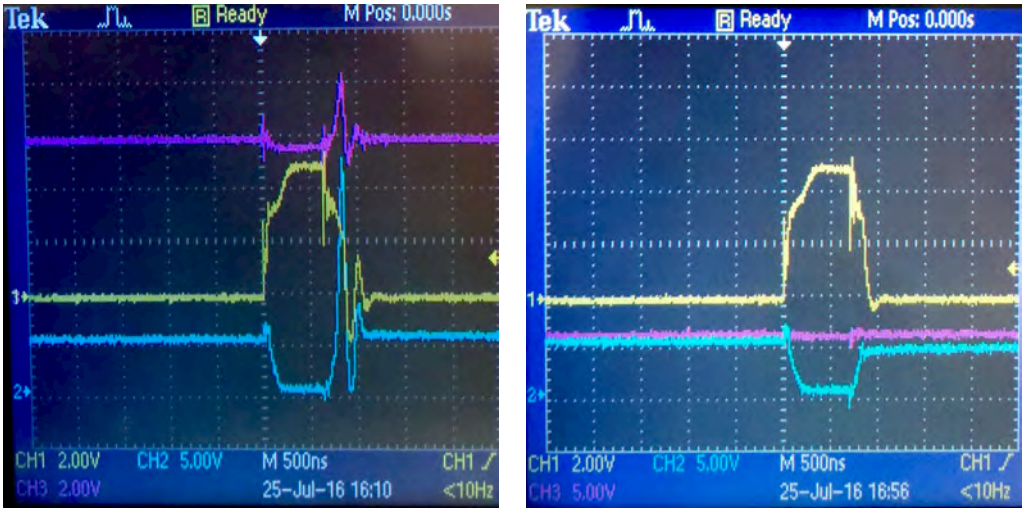

Fig. 4.6 Effect of wire length on the output laser voltage pulse shape shown on Channel 2. The left image shows the laser pulse with large wires used to connect the laser diode to the pulsing circuit and the right image is with shorter wires. A significant reduction in pulse ringing is seen in the image on the right.

The circuit layout was designed to minimise wire lengths, to avoid stray inductive effects and a large copper ground plane was chosen to avoid ground loop issues. At nanosecond scale pulse durations, even small stray inductances can cause large ringing and overshoot in the laser pulse, which can potentially damage the sensitive laser diode. This effect is demonstrated in Figure 4.6 which shows the laser voltage pulse when connected with long wires in the left image and shorter wires in the right image. It can be seen that the ringing in the pulse is significantly reduced when using the shorter wires. Reverse biased signal diodes were also included to further mitigate this effect. The small form factor of the circuit boards also allowed a smaller overall instrument enclosure to be designed to minimise the weight of the overall system, as required for balloon deployment.

4.3 Resolution Testing

The overall system resolution was experimentally tested and constrained using a 1951 USAF resolution test target as well as a range of microscopic calibration test spheres with known sizes. The test target was used to confirm that the system was operating at the expected diffraction limit and the calibration test spheres were used to constrain the geometric magnification factor, along with the overall image reconstruction performance.

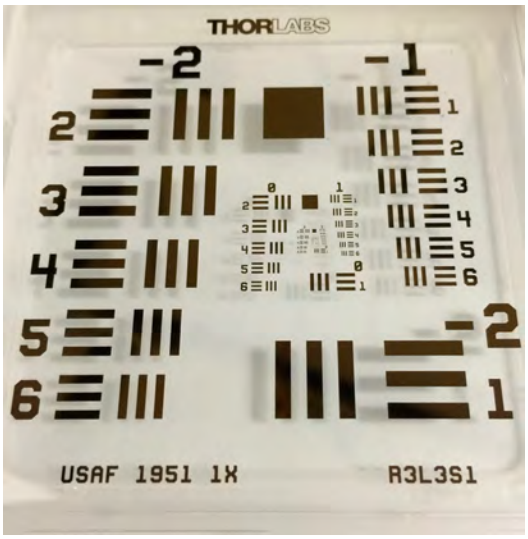

Fig. 4.7 Standard USAF resolution test target used for resolution testing.

4.3.1 USAF Resolution Target Testing

A photograph of the USAF test target is included in Figure 4.7. The target consists of a series of horizontally and vertically spaced parallel lines with consecutively smaller line spacings in each group. The smallest resolvable line spacing in an image of the target provides a measure of the horizontal and vertical resolution of the imaging system under test. As outlined previously, the resolution of the holographic imager is expected to be diffraction limited and hence the resolution should be proportional to the laser wavelength used in recording the interference pattern. This dependence was tested by recording a hologram of the test target for both the 405nm and 830nm laser diodes, whilst keeping the relative camera, object and laser spacing constant to maintain a geometric magnification of unity. The reconstructed in focus images of the test target for each laser wavelength are displayed in Figure 4.8.

The diffraction limited resolution scales linearly with wavelength according to Equation 3.13 and hence the ratio of the minimum resolvable line widths of the test chart should equal the ratio of the laser wavelengths, to within the experimental uncertainty. The ratio of the two laser wavelengths was determined to be 2.04 ± 0.04 where the uncertainty was derived from the 830nm laser spectral measurements above and by assuming an underlying uncertainty in the 405nm laser centre wavelength of 5nm based on information from the L405P20 datasheet. The horizontal and vertical resolutions were measured from the test chart for each wavelength, as summarised in Table 4.1. The ratios of the horizontal and vertical resolutions were both equal to 2.0 to two significant figures, in agreement with the expected value to within the uncertainty in the wavelength ratio. This confirms that the

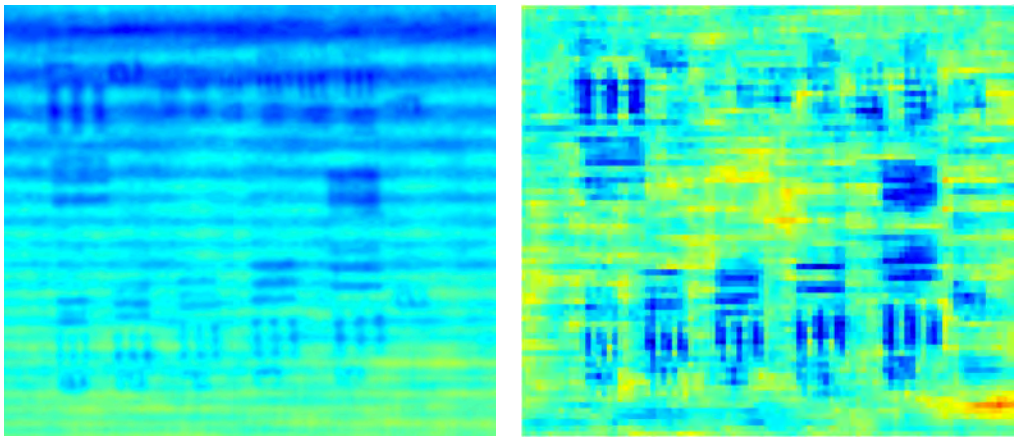

Fig. 4.8 Reconstructed USAF resolution test target recorded with the 405nm laser diode (left) and the 830nm laser diode (right). Note the improvement in resolution obtained by using a shorter wavelength in the left image.

system is operating at a diffraction limited resolution and highlights the need for a shorter laser wavelength to be used in obtaining high resolution measurements.

There was a difference of approximately a factor of two between the horizontal and vertical resolutions for both lasers tested. This could be attributed to the rectangular camera sensor as the resolution is inversely proportional to the sensor extent along a given axis according to Equation 3.13. The ratio of the sensor lengths on each axis is approximately 1.3 and hence this does not solely explain the resolution change. It is possible that the horizontal and vertical axes of the camera were not perfectly aligned to those of the test slide which could explain the differing resolutions. It is also possible that other uncertainties involved in this technique, such as the discrete resolution values used and the visual classification of resolution, will add further uncertainty to this resolution measurement despite the fact that this technique is widely used and accepted[231].

The lower resolution limits from Table 4.1 suggest that the instrument is suitable for the detection of cloud particles with typical sizes ranging from a few microns up to a few millimetres for larger ice crystals. The upper resolution limit of the instrument is determined by the size of the CMOS sensor and was found to be approximately 3 millimetres; however, both the upper and lower resolution limits can be readily improved by varying the image magnification due to the diverging laser diode beam.

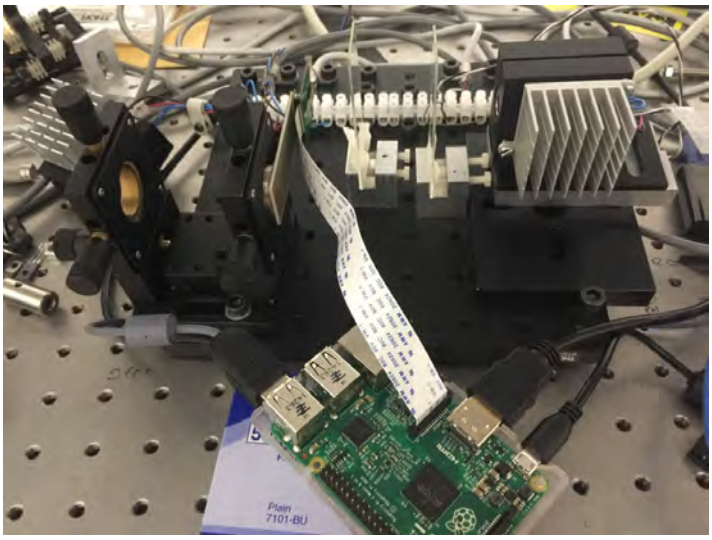

Fig. 4.9 Geometry used to test the 3D image reconstruction software. From left to right: Camera, Raspberry Pi computer, objects on glass microscope slides and a laser diode connected to a thermoelectric heater/cooler.

4.3.2 Calibration Microsphere Testing

A set of monodisperse calibration test spheres was used to both validate the developed reconstruction software and also to constrain the geometric magnification effects of the system. The reconstruction software was validated by placing a set of glass calibration test spheres at two depth positions within the detector sampling volume on transparent glass microscope slides. Spheres with a diameter of 20 microns were selected to simulate typical water droplets in a cloud. A prototype of the imager, along with the geometry used in this testing, is shown in Figure 4.9.

The interference pattern formed between the scattered light from the objects and the unscattered reference wave is displayed in Figure 4.10. The raw hologram and the reconstruction software outlined in the previous chapter were then used to reconstruct the object

Resolution criteria	405nm Laser		830nm Laser	
	Horizontal	Vertical	Horizontal	Vertical
Group+Element	G7 $E4$	G6 $E4$	G6 $E4$	G5 $E4$
Smallest resolvable line width (μm)	2.76	5.52	5.52	11.05

Table 4.1 USAF resolution testing results for the 405nm laser and 830nm laser.

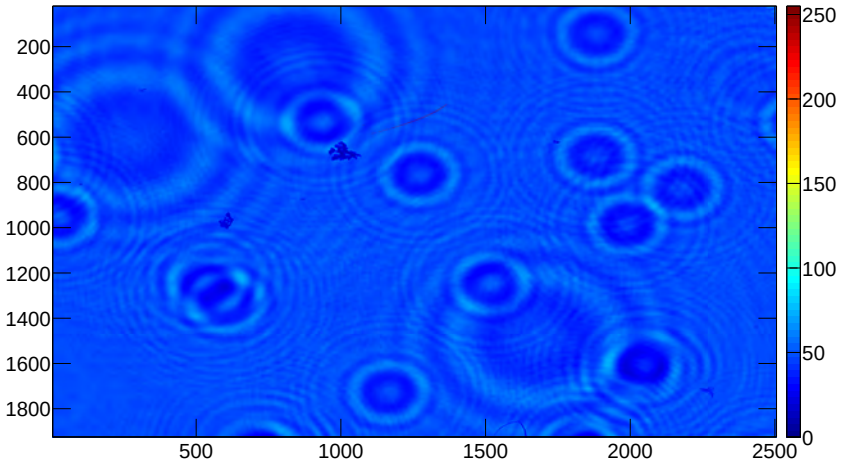

Fig. 4.10 Raw interference pattern recorded for the detector geometry shown in Figure 4.9.

wave intensity at a range of depth positions to produce a three dimensional (3D) image of the objects. A subset of this 3D image is presented in Figure 4.11. Each image in consecutive order shows the reconstructed object wave intensity at a successively greater depth position relative to the sensor. It can be seen that a set of spherical particles come into focus in Figure 4.11.b at a nearby depth, corresponding to those on the first microscope slide, along with another set of particles in focus in Figure 4.11.e at a greater depth position, corresponding to those on the other microscope slide. The reconstructed 3D image is also displayed in Figure 4.12 which shows a front and side perspective view of the 3D image. The particles are seen to be in focus at two distinct depth positions, as highlighted by Figure 4.12b. This also highlights the poorer resolution in the reconstructed depth positions as compared to the lateral object positions, as expected based on equations 3.13 and 3.14.

The particles at the greater depth position in the previous 3D image appear larger than the nearer particles as a result of the geometric magnification of the images, due to the divergent laser wavefront. The output depth positions along the optical axis for the particles are also magnified and this magnification must be corrected for to extract the true object properties. This underlying magnification can be described by the standard holographic imaging equations[213]. If a planar reference wavefront is used to reconstruct the image and a spherical reference wavefront is used to record the image, this magnification can be simplified to the following form

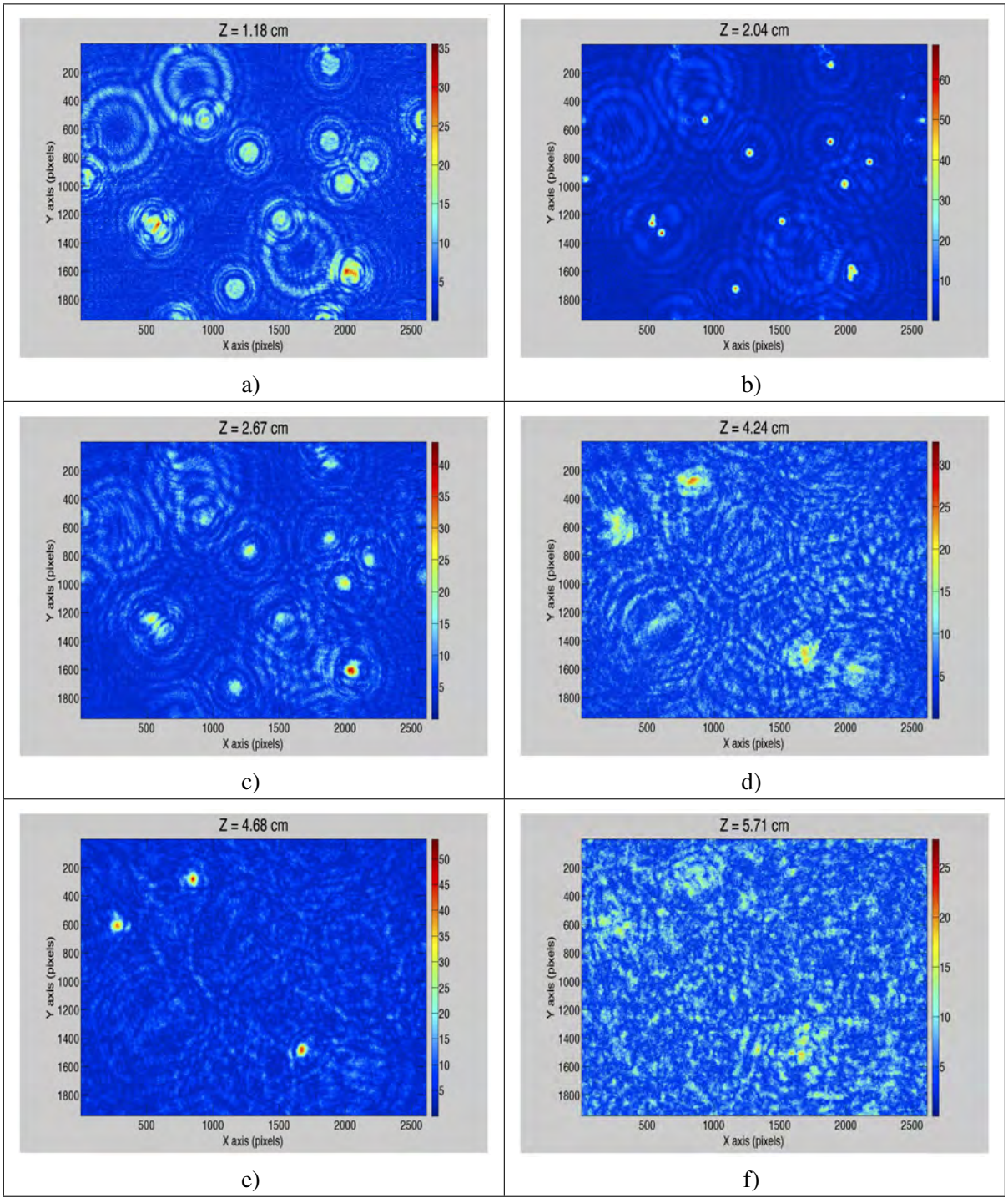

Fig. 4.11 Reconstructed 3D image at a range of consecutive depth positions from image a) through to image f) as displayed by the Z parameter. Images b) and e) show the in focus particle images at locations corresponding to the glass microscope slides in Figure 4.9.

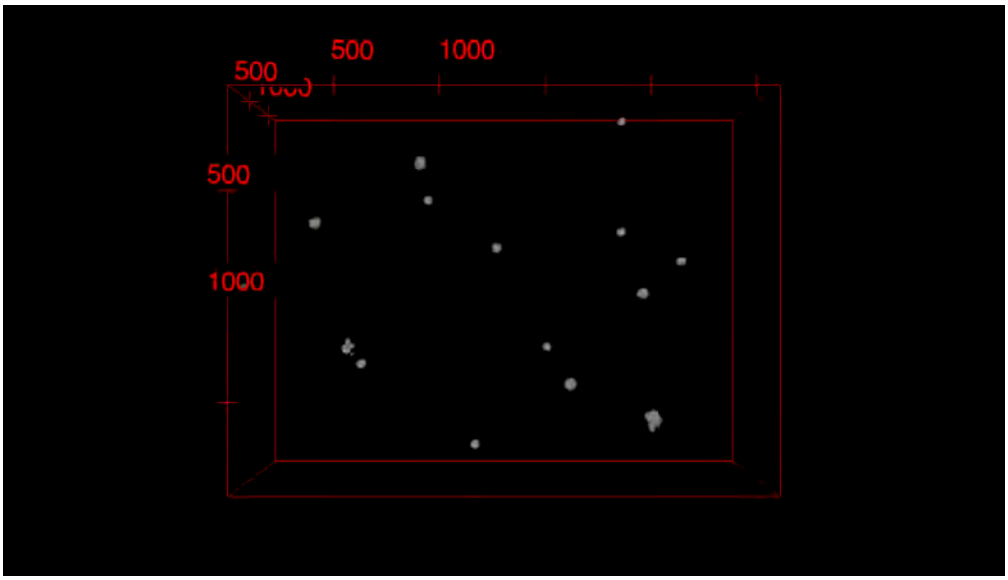

(a)

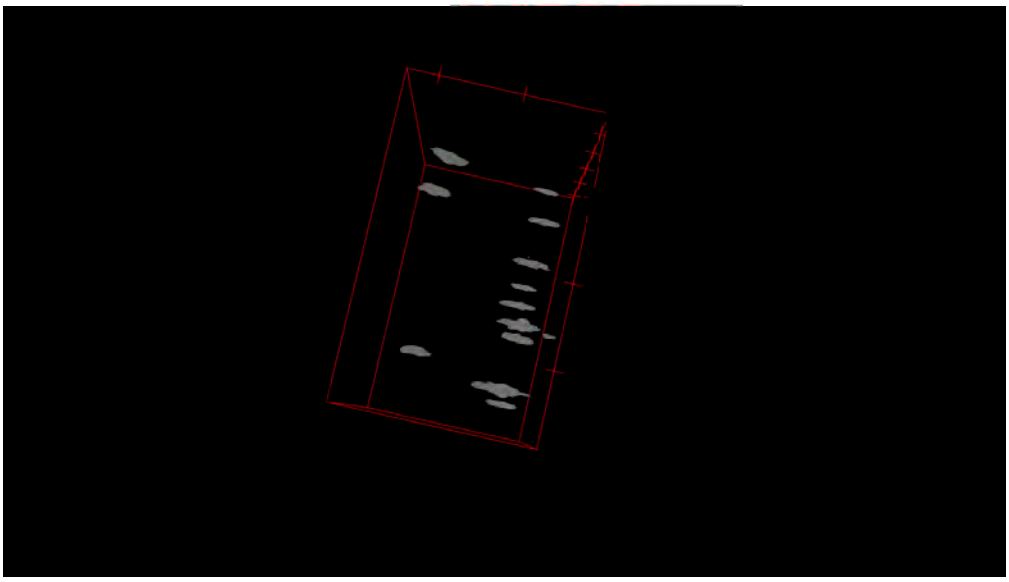

(b)

Fig. 4.12 Perspective views of the 3D image reconstructed from the hologram in Figure 4.10 for a) a front viewing looking down the sampling volume and b) a side view highlighting the different depth positions of the two sets of particles.

$$M = \frac{D_{\text{Image}}}{D_{\text{Object}}} \tag{4.2}$$

$$= \frac{-1}{\frac{\left(\frac{1}{Z_{\text{focus}}}+\frac{1}{Z_L}\right)^{-1}}{Z_L} - 1} \tag{4.3}$$

where M is the magnification, D_{Image} is the size of the reconstructed particle image, D_{Object} is the true size of the object, Z_{focus} is the depth position at which the objects come into focus and Z_L is the depth position of the laser relative to the camera sensor. This formula relies on the assumption that the laser diode beam can be described as a spherical wavefront. If the laser diode wavefront is modelled as a single order TEM_{00} Gaussian beam, then the wavefront will be spherical provided that the observation point is much greater than the Rayleigh Range (Z_{R}) defined by the relation[232]

$$Z_R = \frac{\pi\omega_0^2}{\lambda} \tag{4.4}$$

$$\simeq \frac{\lambda}{\pi\theta^2} \tag{4.5}$$

where λ is the laser wavelength and θ is the far field divergence angle. Using the information from the laser datasheet for these parameters, the corresponding Rayleigh Range distance was calculated to be approximately 10 microns. The distance between the laser and the sampling volume was therefore set at around 2 centimetres, which is multiple orders of magnitude greater than the Rayleigh Range and hence the magnification formula presented above should be suitable for this system.

The magnification was tested by measuring the sizes of a set of calibration test spheres with diameters of 15.5 ± 0.1 microns. These spheres were placed at a range of depth positions and at each depth, the magnification formula was used to measure the true object size. The resultant object sizes as a function of depth are shown in Figure 4.13. The measured particle sizes were in agreement with the expected values to within the uncertainty throughout the tested sampling volume. The measured particle size uncertainty scales with depth due to the depth dependent magnification equation. This depth dependence causes the physical size corresponding to each pixel of the image to scale accordingly. Particle size is determined by counting the number of pixels in the in-focus particle image and then converting to the physical size via the magnification formula conversion and accounting for the physical size of the pixels. The uncertainty is then determined by calculating the change in particle size

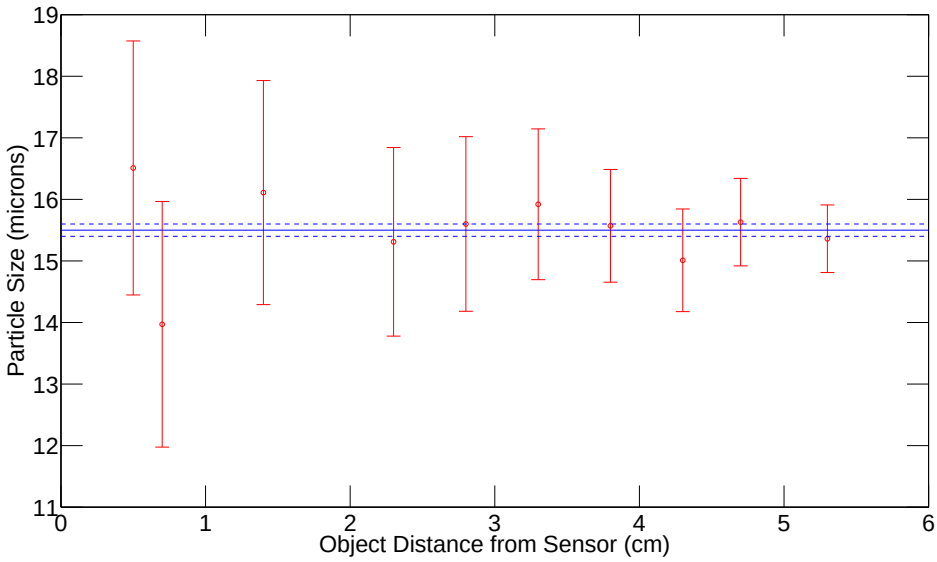

Fig. 4.13 Particle sizes measured by the system as a function of their depth position within the sampling volume. Results agree to the expected value shown by the blue line to within the uncertainty.

introduced by adding or subtracting a single pixel from the measured number of pixels in the image. This measure of uncertainty is an underestimate of the total uncertainty as it does not incorporate the uncertainty associated with the automated analysis technique which must first identify the in focus particle extent in pixels using edge detection and intensity thresholding criteria. These techniques can be made more robust by obtaining realistic intensity thresholds to separate particle images from the background noise, which can be obtained via manual analysis of field results from a field campaign in which the instrument was tested, as discussed in the next chapter.

The agreement between the measured and true particle sizes implies that this system can accurately reconstruct particle sizes throughout the instrument sampling volume. This agreement also provides validation that the far field laser wavefront is spherical, as was assumed in deriving the magnification formula. Future testing should be undertaken to investigate possible systematic errors such as a dependence on the size of the measured particle, particle shape, effects of higher order transverse modes in the laser beam and particle sizing in the presence of overlapping particles. Smaller systematic uncertainties are introduced due to the temperature dependence of the laser wavelength if the temperature control system is not operating ideally and due to the uncertainty involved in measuring the

spacing between the camera and laser as required for the magnification formula; however, these effects are only minor as discussed in the previous chapter.

4.4 Temperature Control and Power Supply

An analogue Proportional Integral Derivative (PID) temperature control circuit incorporating a Peltier thermoelectric heater/cooler (TEC) actuator was designed to maintain a stable system temperature and hence a stable laser wavelength. This was necessary to avoid errors being introduced due to a changing magnification as this depends on the wavelength and also to ensure that the temperature dependent laser spectrum was within the bandpass region of the optical bandpass filter. This was also required to avoid condensation of the sampling windows and icing up of the electronics in the harsh conditions within a cloud. An analogue system was designed rather than a digital one as it had a low cost, low power consumption, high response speed and is not prone to digitisation errors. Drawbacks to the analogue approach include the time consuming trimpot adjustments needed to tune the system to a given thermal load and also the sensitivity to temperature dependent drifts of the electronics. For these reasons, a digital alternative should be considered in future.

The temperature controller circuit diagram is shown in Figure 4.14. The input power supply voltage can be either single sided or dual polarity, depending on whether the thermal actuator is a simple resistive heater or a Peltier thermoelectric heater/cooler. This input voltage is first input to a Ref5010 voltage reference IC to provide a fixed operating voltage for the system. A Wheatstone bridge configuration is then used to set the desired system temperature via the variable resistor (RVar) and sense the system temperature using the thermistor (RT). The temperature can alternatively be measured using the optional LM335 digital temperature sensor and LM741 amplifier. The LM335 sensor allows the temperature measurements to be directly recorded on the Raspberry Pi computer; however, it is less accurate than the thermistor. The voltages corresponding to the set point temperature and measured temperature are then input to an LM358 based difference amplifier to obtain the error signal for the feedback system. This is then buffered with an LM358 amplifier which provides a pre gain stage via the P1 variable resistor. This error signal is then split into three separate branches to produce the proportional, integral and differential components of the PID control system. The integral and differential signals are obtained using integrator and differentiator op amps respectively and the proportional signal is obtained with a simple LM358 amplifier. An FET based OPA2604 op amp was used for the integrator to reduce the impact of input offset current effects on the integrator output signal. The relative strength of each of the PID signals can be varied with the P2, I and D variable resistors and the time

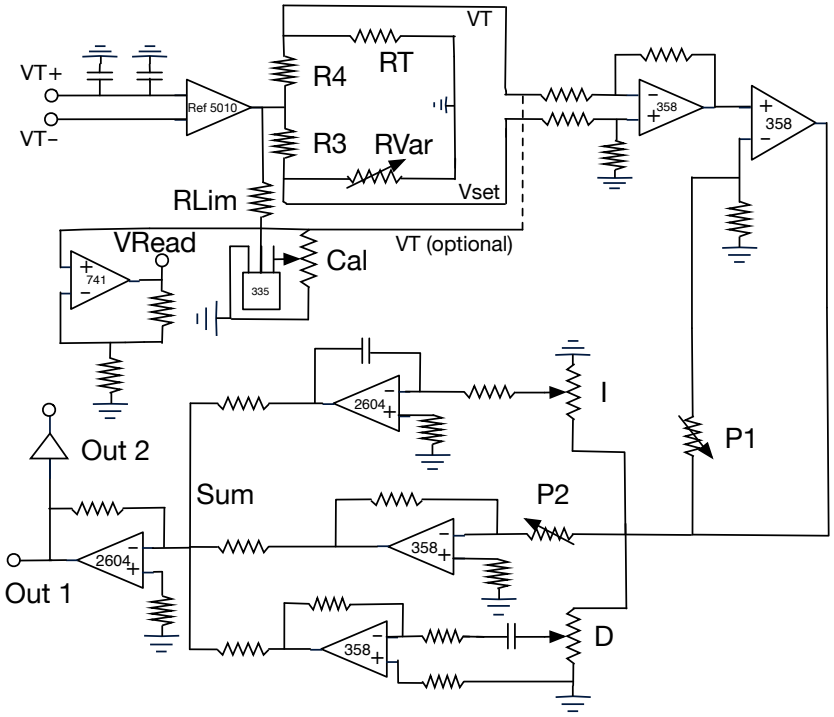

Fig. 4.14 Analogue PID temperature controller circuit diagram. The temperature can be sensed using either a high precision thermistor or a digital 335 temperature sensor. The output control signal is then amplified and applied to the TEC.

constant of each of the stages can be chosen by varying the feedback resistors and capacitors to match the controller to a given thermal load. The proportional, integral and differential signals are then input to a summing amplifier and the output PID signal can then be amplified and applied to the thermal actuator to close the feedback system.

The temperature control system was experimentally tested by placing the actuator TEC inside of a sealed metal box. A TEC operating at half of the maximum output power of the actuator TEC was then placed on the exterior wall of the box and the temperature controller was set to maintain a stable room temperature. Testing was then performed for a range of actuator TEC configurations to determine the overall performance when operated. The system was observed to operate effectively until the effects of self heating of the TEC became dominant. These tests indicated the need for suitable heatsinking to be applied to the system and also the need for carefully matched time constants for each of the PID stages. Future testing will need to be carried out to determine the expected thermal load of the atmosphere in order to optimise the temperature control response. The required heat sinking is also dependent on knowledge of the atmospheric thermal response as this will dictate the

smallest required heat sink size to minimise the overall mass, as required for a balloon borne system. These effects could either be constrained experimentally in a cloud chamber testing environment or through the use of thermal modelling software.

The circuit diagram for the overall system is shown in Figure 4.15. A range of DC input voltages (Vin) are acceptable allowing the instrument to be powered with a battery, as required for weather balloon deployment, or with a floating power supply at an instrument field site. The input supply voltage (Vin) is then input to the LM2596 and LM1084 voltage regulator circuits to provide stable voltages within the acceptable voltage ranges of each of the components, such as the Raspberry Pi computer, pulsing circuit and the PID temperature control signal amplifier as shown. A split power supply is required for the PID controller to allow the Peltier TEC to provide both a cooling and a warming effect as the PID control signal goes from negative to positive. The single sided input voltage (Vin) is converted to a split supply voltage using a circuit based on an LM675 power op amp. The output of the PID controller is then input to an LM675 based power amplifier to boost the drive current which is then applied to the Peltier TEC.

4.5 System Automation and Stability

The instrument was designed to operate autonomously in cloud conditions, over potentially long periods of time if stationed on a tower site. To facilitate this goal, Linux and Arduino code was developed to automatically begin the system processes and start recording data when the instrument is connected to a power supply. The Arduino code outputs the clock signal used to synchronise the camera exposure and laser pulses and also records data from optional internal and external temperature and humidity sensors. This information is then read in by the Raspberry Pi computer and recorded for further analysis. The Linux code is used on the Raspberry Pi to automatically run the modified QT based GUI camera interface and initialises the recording parameters such as output file format. A real time clock is used to provide accurate timestamps for images when taking data in remote locations.

The automated analysis algorithm introduced in Chapter 3 allows the particle size and shape distributions to be automatically extracted from the reconstructed 3D image. This algorithm can be run via a python script to transmit processed observables during a weather balloon flight to a ground station receiver, since bandwidth is a limitation in this application or alternatively, can be undertaken when the data is retrieved from the instrument hard drive for tower deployment. The analysis software is currently not fast enough to be operated in real time for realistic sampling rates on a weather balloon platform due to the limitations of the Raspberry Pi processor; however, the performance could be dramatically improved

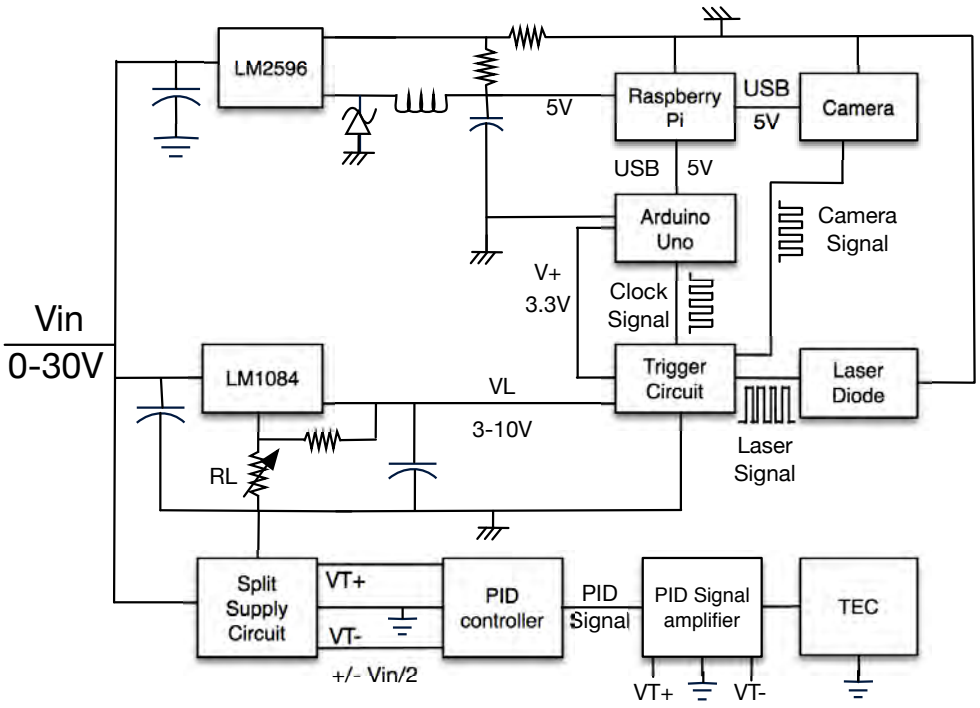

Fig. 4.15 Circuit diagram for the overall system highlighting the power supply componentry along with the connections between each of the system components.

by making use of GPU acceleration and parallel processing techniques available with more modern mini computers.

The automated analysis software performance was tested using a set of glass calibration test spheres of known sizes. An example of this testing is shown in Figure 4.16a which displays the in focus reconstructed intensity image of a set of test spheres with sizes ranging from 63 to 75 microns, all placed at a single depth position within the instrument sampling volume on a glass microscope slide. The red circles identify particles that have been automatically detected by the algorithm and it can be seen that the majority of particles have been located. The corresponding extracted histogram of particle sizes is shown in Figure 4.16b. If the underlying particle size distribution is assumed to be uniform, this result agrees with the expected values with an uncertainty in agreement with that expected from particle counting statistics.

It can be seen that not all particles are successfully identified in Figure 4.16a and a number of particles have been falsely identified. This can in part be attributed to the non ideal intensity threshold used to identify initial particle locations, the resolution constraints involved in

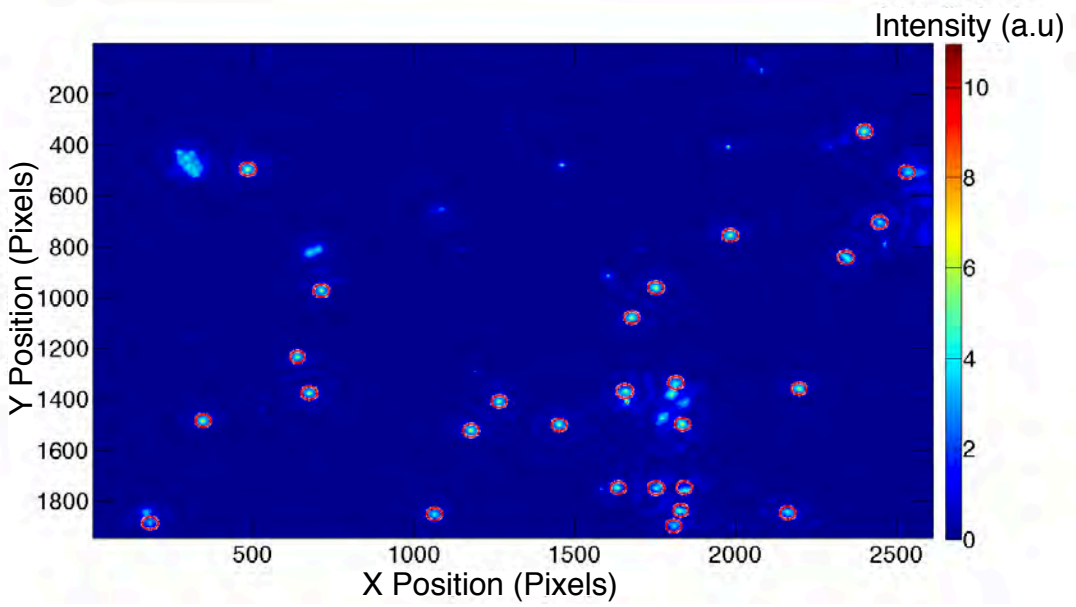

(a)

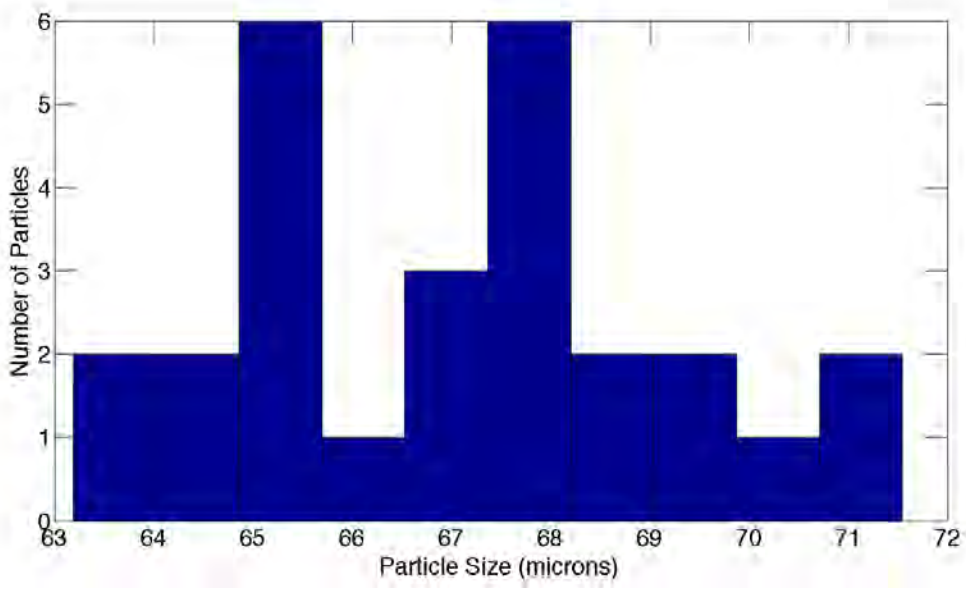

(b)

Fig. 4.16 a) In focus reconstructed intensity image for a set of calibration test spheres placed at a single depth position. Red circles indicate particles that have been successfully identified and sized by the automated analysis algorithm. b) Automatically extracted particle size distribution for the detected spheres in Figure 4.16a.

separating two closely located objects and the underlying noise in the reconstructed image. It was found that all particles could be successfully located by varying the intensity threshold used and hence a more realistic intensity threshold should be determined in future based on the image properties by using a modified Otsu's method[226]. Realistic intensity threshold information can be obtained by manual inspection of real cloud particle data taken in the field and this was one of the goals of the field campaign in which this instrument was tested.

To determine the long term system stability, the instrument was operated for a duration of 55 hours and the times at which each image was saved were recorded. The measured recording times were then compared to the expected recording times for the sampling period of 5 seconds which was expected to be constant by design. It was seen that as a function of time, the observed times deviated from the expected times in a linear fashion as shown in Figure 4.17. The difference between successive images as a function of time is plotted in Figure 4.18a and a zoomed in portion of the time series is seen in Figure 4.18b. It can be seen that the sampling period is oscillating between 5 and 6 second sampling periods, with a 6 second spacing occurring approximately periodically every 130 seconds. Larger sampling periods are also seen intermittently. The source of this oscillating sampling period could be identified in future by testing with different real time clocks and studying the Linux system logs; however, as the effect appears to be temperature independent and easily characterised, the current approach is simply to record the true sampling times of each measurement when comparing observations with other instruments. Aside from this oscillation, the system was seen to operate in a stable fashion for the 55 hour observation period.

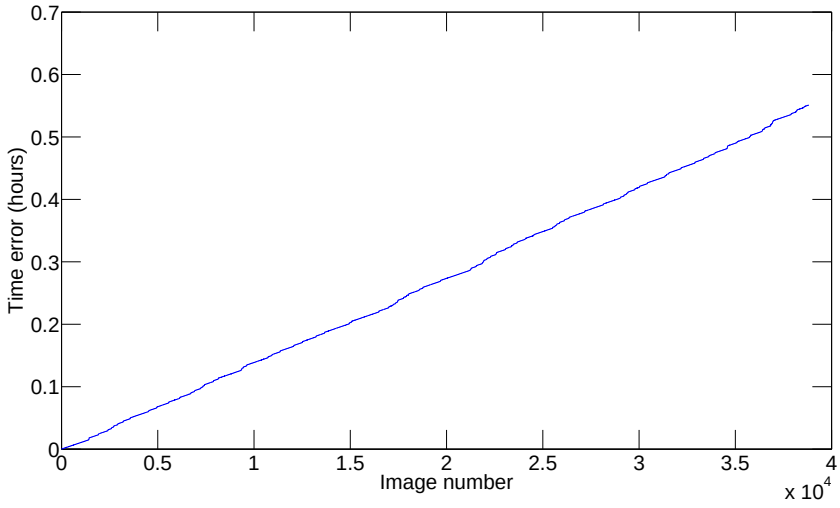

Fig. 4.17 Difference between the observed and expected image recording times for each successive image.

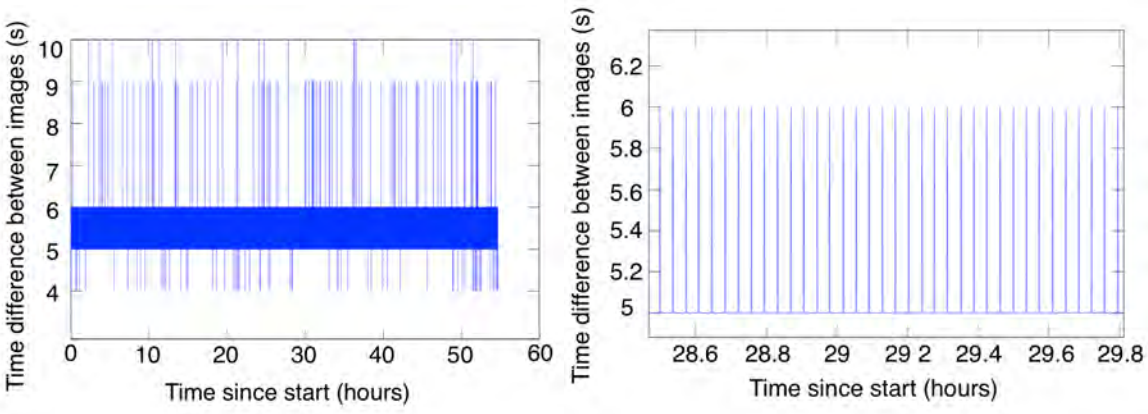

(a) (b)

Fig. 4.18 a) Time difference between successively recorded images as a function of operation time. b) Zoomed in view of Figure 4.18a to highlight the periodicity of the variation in sampling period.

The stability of the pulsed laser wavefront was also measured as a function of time. The laser intensity was seen to fluctuate as a function of time in a deterministic manner, in the form of curved interference fringes overlaying a uniform background. An example of this non uniformity is shown in Figure 4.19a which shows the image intensity recorded from two consecutive laser pulses. A set of curved interference fringes were seen at varying intensities relative to the uniform background, along with a fixed set of diagonal interference fringes. The properties of these fringes are easily distinguished by observing the changes in the two dimensional Fourier transform intensity spectrum, also included in Figure 4.19a, as a function of time. The features that changed between the two spectra were removed, along with the features corresponding to the fixed diagonal fringes, using spatial filtering in the frequency domain and the resultant filtered image is shown in Figure 4.19b. This image is significantly more uniform and hence these background fringes can be removed in the analysis stage. The origin of these fringes was not confirmed but it is likely that the fixed diagonal fringes correspond to Fabry-Perot interference due to the plane parallel glass sampling windows of the instrument and the fluctuating curved fringes could be due to higher order transverse modes in the laser beam due to thermal expansion of the gain medium. The source of these features could be investigated further in future by testing for explicit temperature dependent effects and their effect could likely be mitigated further by use of a pinhole spatial filter.

The effect of these non uniform features was seen to decrease as the camera-laser spacing was increased and the laser pulse power was increased. For most sampling volume and laser power combinations, these varying fringe backgrounds were negligibly small and hence spatial filtering was not required in most cases. This reduced effect is demonstrated in

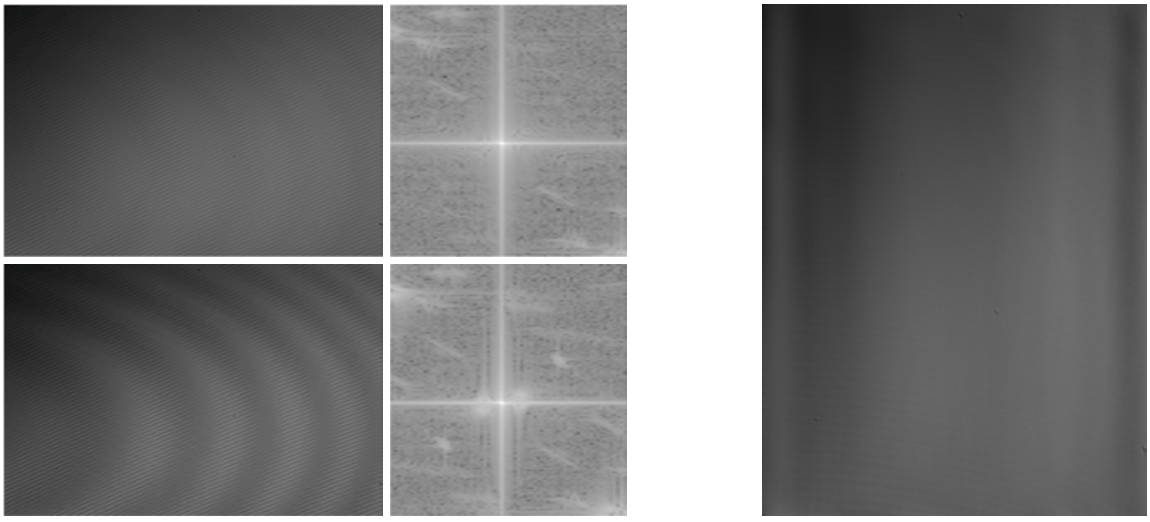

(a) (b)

Fig. 4.19 a) The top row shows the intensity recorded on the camera for a single pulse of the laser diode along with the corresponding two dimensional fast Fourier transform. The bottom row shows the next consecutive pulse recorded from the laser with the corresponding Fourier transform. Note the appearance of curved interference fringes between pulses. b) Laser intensity distribution after applying spatial filtering to remove the time varying curved fringes and fixed horizontal background fringes.

Figure 4.20 which shows the laser pulse intensity between two consecutive pulses with calibration test sphere objects placed inside the sampling volume on glass microscope slides. The circular interference fringes produced by the objects are significantly brighter than the background fringes and hence minimal variation is seen between consecutive images. In summary, the laser wavefront was seen to be acceptably stable for most system geometries and spatial filtering techniques can be used to further reduce the impact of these features if necessary.

4.6 Enclosure Design

The instrument enclosure was designed to be both light weight and suitable for operation in the extreme temperature, condensation and turbulence conditions encountered within a cloud. An image of the final developed instrument is included in Figure 4.21 before the components were sealed within the boxes. A commercially obtained IP56 dust and water proofed plastic box is used to house the main electronic control systems. Each of the electronic components can then be independently assembled and screw mounted onto plastic stand off sheets and these can then be individually screw mounted inside the box. Internally tapped screw threads

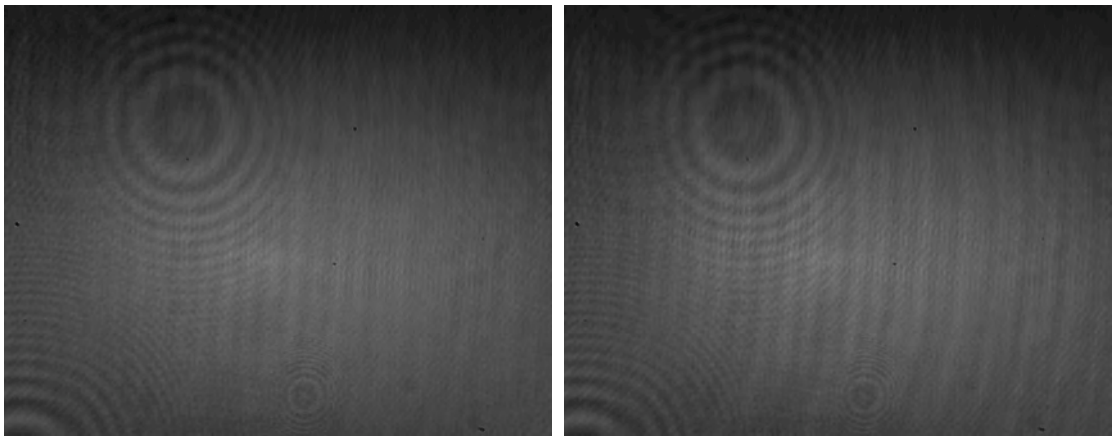

Fig. 4.20 Variation between consecutive laser pulses with a higher laser power and larger sampling volume. The effect of the background fringes is now significantly reduced relative to the fixed fringes produced from the test objects.

were used so that the necessary waterproofing of the box was maintained. Plastic at the bottom of the box was cut away to allow extra space, which was necessary to include all of the components shown in Figure 4.21. An external hard drive and cable gland access are provided for extended ground based deployment and testing purposes. The external hard drive is not required for weather balloon deployment since data obtained within the short flight durations can be stored on a USB or SD card. The space allocated to the external hard drive can instead be used for a battery power supply in this case.

The camera is mounted inside a smaller waterproofed plastic box, as shown in Figure 4.22a. A square aperture was cut into the front of the box and a glass microscope slide was cut to shape and glued over this aperture to allow the laser light to illuminate the sampling volume. A lightweight Delrin mount has been included to allow an optical filter to be installed in front of the camera sensor to minimise the effects of stray sunlight in the images. Resistive heaters are included around the edges of the microscope slide to avoid condensation on the sampling windows. A small hole has been cut into the top of the box to allow power supply wire connections and data transfer between the smaller box and larger box. These wires were strain relieved to ensure that the connections were maintained in turbulent cloud conditions and the hole was sealed using water proofed Silastic.

A similar box design was implemented for the laser diode and pulse amplifier circuit as shown in Figure 4.22b. The laser diode is mounted inside an Aluminium lens tube within a larger Aluminium tube mount that is counter sunk screwed to the bottom of the box. Two lens tubes were designed with sizes conforming to the commonly used $\phi 5.6$ mm and $\phi 9$ mm laser

Fig. 4.21 Image of the final developed instrument before the boxes were sealed. Each of the electronic control stages can be independently adjusted and then all components are mounted within water proofed plastic boxes.

diode aperture sizes. The lens tube design also allows for future inclusion of a collimating lens to enable large sampling volumes to be used without the need for an increased laser power to compensate for a decreasing beam intensity from a diverging beam. A metal mount was chosen to allow efficient thermal transfer between the laser diode and the Peltier TEC connected to the PID control circuit. The TEC is mounted between the laser mount and a metal heat sinking plate at the bottom of the box. Desiccants were included in each of the boxes to further mitigate the effect of condensation on the sampling windows and electronics.

The position of the laser diode within the mount can be varied continuously and then locked in place by tightening the connecting screws between the outer mounting tube and the base of the mount. The ability to vary the spacing between the laser and the sampling window was desired as this allows the trade off between image magnification and sampling volume size to be controlled. As the laser-sampling window spacing is decreased, the magnification increases according to Equation 4.3 and hence smaller objects can be resolved, provided a suitable number of fringes are recorded on the sensor. Reducing this spacing also results in a decrease in the size of the instrument sampling volume, defined as the product of the laser beam spot area and the sampling window spacing. The sampling volume was modelled

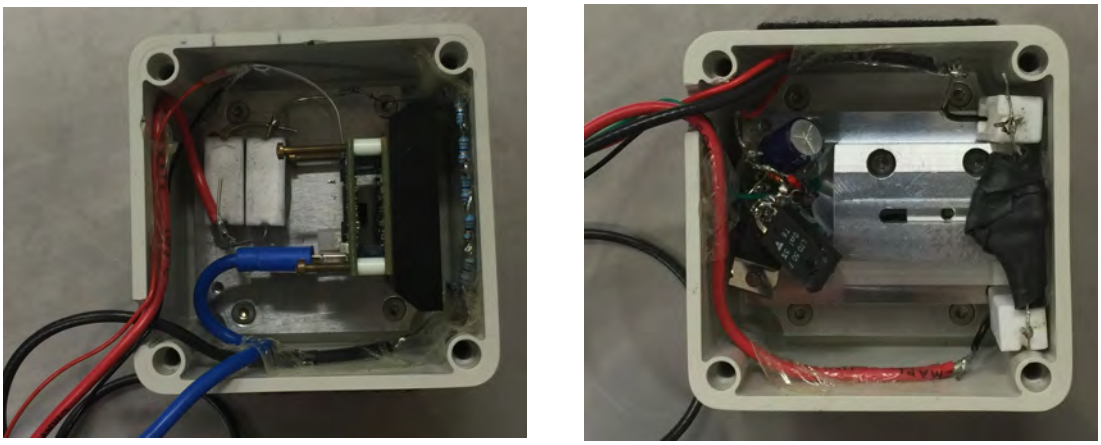

(a) (b)

Fig. 4.22 a) Box in which the camera and optional optical filter are mounted. Resistive heaters are used to avoid condensation effects on the sampling window. b) Box in which the laser and pulsing circuit are mounted. The laser position can be varied to adjust the magnification and the temperature is controlled with a heatsinked TEC.

by approximating the laser diode wavefront as an elliptical Gaussian beam with divergence angles obtained from the datasheet. The volume was then calculated using the area of this ellipse as a function of depth and integrating the solid of revolution. The laser spot area was clamped at the value obtained when the spot area on the sampling windows became greater than the camera sensor area, as it was assumed that angular scatter from particles outside of the forward scattering region would be negligible. The modelled sampling volume size as a function of the laser-sampling window depth and the sampling window spacing is included in Figure 4.23. This model is useful in designing different experimental modes of operation for the instrument based on the trade off between required laser power, which decreases as the inverse square of the propagation distance, the size of the sampling volume and the desired image magnification which depends on the laser position, due to the divergent beam.

The spacing between the boxes can be varied to provide a trade off between the sampling volume size and the required laser power for the divergent laser diode beam. A collimating lens can be included to minimise this divergence loss to allow large sampling volume sizes of upwards of 10 cubic centimetres; however, this comes at the cost of a reduced magnification. Due to the modular design, a wide parameter space of magnification, sampling volume and required laser power combinations are possible to allow a range of experimental studies to be performed with this instrument. The instrument has been designed for deployment on either a weather balloon or a tower structure and so the method for varying the box spacing depends on the application. For weather balloon deployment, the relative forces on the smaller boxes relative to the large box are relatively small and so a light weight Aluminium mounting

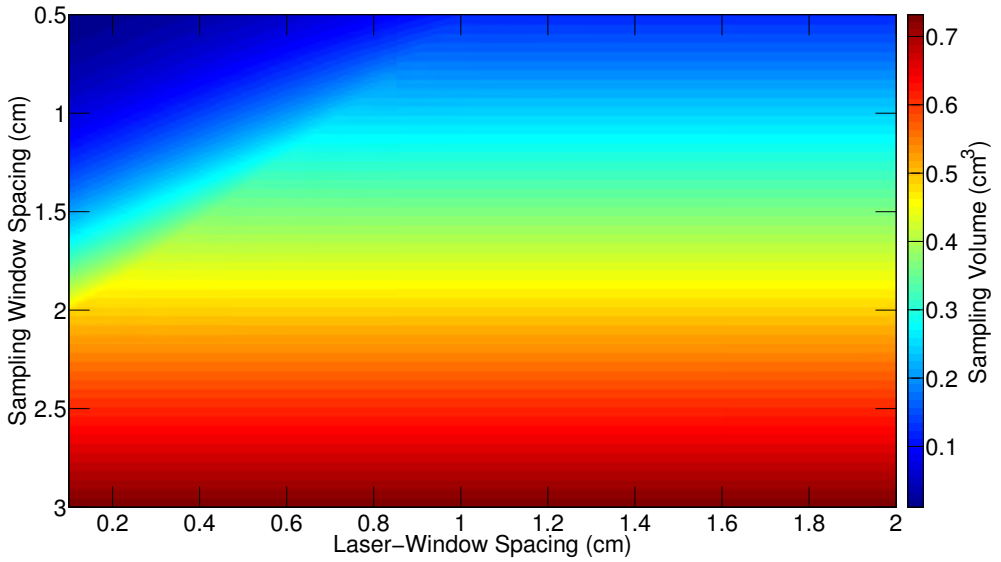

Fig. 4.23 Modelled instrument sampling volume size as a function of the sampling window spacing and laser-sampling window spacing.

bracket was used since the balloon payload size and weight needed to be minimised. The box spacing can then be easily varied at discrete intervals. For deployment on a tower, a sturdier mounting bracket was needed to keep the main boxes attached, due to the larger relative forces exerted by the winds. This requires the sampling volume to be fixed for a given mounting bracket, but can still be varied by changing the mounting plate. These mounting configurations are summarised in Figure 4.24.

Fig. 4.24 Mounting configurations developed to control the spacing between the instrument sampling windows. The left configuration is light weight and suitable for balloon deployment and the right configuration is more sturdy, as required for deployment on a tower.

Chapter 5

Field Testing Results

5.1 Introduction

The instrument was tested in a field campaign at a Tasmanian mountain field site. The major goals for this testing were to investigate the long term stability and performance of the instrument in realistic cloud conditions, determine more realistic intensity thresholds to extract particle information with the automated analysis software and to provide validation for an independently developed polarimetric backscatter instrument sensitive to cloud particle phase. An overview of the field site conditions will be presented in this chapter along with details about the preparation process and a preliminary analysis of some data in which cloud particles were identified.

5.2 Field Site Details

The field site is located at $(-41.84S, 145.54E)$ which corresponds to the Mount Read mountain in Tasmania. The site was selected due to a combination of the relatively high elevation of 1123 m, suitable climate for potential ice crystal formation inside of clouds and the fact that infrastructure and security measures were already in place at the site. The site is operated by TasNetworks whose assistance is gratefully acknowledged for their role in supplying power to the instruments and in installing the instruments on their tower structure. A photo of the region surrounding the tower on which the instruments were installed is included in Figure 5.1. It can be seen that clouds had formed below the height of the instrument positions, suggesting that the site was at a suitable height for intersection of the instrument sampling volumes with clouds as they form and travel.

Fig. 5.1 Photo of the region surrounding the Mt Read field site at which the holographic instrument was tested. The presence of clouds around the tower highlights the suitable elevation and climate for cloud studies.

The holographic instrument was deployed on the tower alongside a Polarsonde instrument as shown in Figure 5.2. The Polarsonde instrument emits polarised light into the cloud and measures the depolarisation of the returning backscattered light. This provides information about the shape of the scattering particles and hence can be used to distinguish aspherical ice crystals from spherical water droplets within a cloud. The holographic instrument was placed on a different face of the tower to the Polarsonde to minimise the chance of backscattered Polarsonde light into the holographic camera field of view. The placement was also chosen such that the prevailing winds would tend to force clouds into the instrument sampling volume to minimise sampling biases due to interaction of cloud particles with the instrument enclosure. Further information about the meteorological conditions at the site, such as the temperature and relative humidity, were obtained from a nearby weather station operated by the Bureau of Meteorology.

5.3 Preliminary Preparation

Prior to deployment of the instrument at the field site, a fault was detected in one of the components of the laser pulsing circuit. This circuit was replaced with an alternate design incorporating a MOSFET to amplify the pulsed laser current. This circuit provided a

Fig. 5.2 Tower structure on which the holographic instrument and Polarsonde were deployed. A zoomed in view of the holographic instrument is shown in the bottom right inset and the Polarsonde is shown in the top right.

smaller peak power than the primary design and hence the optical filter was not used in this deployment to minimise further attenuation of the laser signal. The orientation of the instrument on the tower was therefore chosen to minimise the influence of stray light from the sun and moon into the field of view of the camera. The instrument was operated in the lab before sending it to the field site over the course of multiple hours to obtain a large number of images of the reference wave intensity with no objects present. These images can then be used for flat fielding and background subtraction in the analysis stage to improve the SNR.

The instruments were planned to be deployed on the tower site for a duration of at least two weeks and hence the sampling rate of the instrument had to be optimised to provide useful data over this duration. A single raw image from the camera is approximately 10MB in size and contains information about cloud particles at a given moment in time. To study how the cloud particle properties evolve with a high temporal resolution over the entire deployment duration, a 4TB external hard drive was included to maximise the possible sampling rate. For a storage size of 4TB and a deployment duration of two weeks, it was calculated that the maximum possible sampling rate was 0.2 images per second or one image every 5 seconds. Clouds were assumed to be passing the detector at speeds similar to the

background winds, of order 5 m/s. This sampling rate therefore provided a suitable balance between allowing the study of local cloud structural inhomogeneities on the scale of a few metres in size and enabling a relatively low cost for the required external hard drive which scales with memory capacity.

The sampling volume configuration was selected to provide a minimum magnification of the images and instead provide a larger sampling volume size by setting a relatively large laser-sampling window spacing of approximately 1.2cm. The spacing between the sampling windows was chosen to be 3.1cm and the laser power was set to provide a sufficient hologram intensity on the camera, as tested with calibration spheres. The final sampling volume size was calculated to be approximately 0.8 cm^3. The noise in the hologram scales with the sampling volume size due to particle-particle scattering and it can be shown that this effect becomes significant at a threshold particle number density given by the relation[53]

$$n_c = \frac{0.04}{\pi d^2 l} \tag{5.1}$$

where d is the particle diameter and l is the depth of the sampling volume. For a typical particle diameter of 15 microns and a sampling depth of 3.1cm, this corresponds to a threshold of 1830 particles per cubic centimetre. Typical water droplet number densities in the atmosphere are well below this limit[54] and hence particle-particle scattering effects are likely to be negligible for this sampling volume size. This limit does not take into account the effects of magnification due to the diverging reference beam; however, it provides an approximate upper limit for the particle densities at which this effect becomes significant.

5.4 Preliminary Data Analysis and Future Work

A number of cloud events were identified in the datasets of both the holographic instrument and the collocated Polarsonde instrument. One such event that was identified is shown in Figure 5.3 which shows two slices of the reconstructed 3D image at different depth positions at which cloud particles were identified. The reconstructed particle images are identified by the in focus dark regions relative to the lighter background and red bounding circles have been overlaid to emphasise the locations of some of the larger particles. An Arago diffraction spot is seen towards the centre of the larger particles as expected since this corresponds to the Fresnel diffraction regime. The transverse and longitudinal co-ordinates displayed on the image have been corrected for magnification effects and hence the particle sizes and 3D positions can be directly read off from the images.

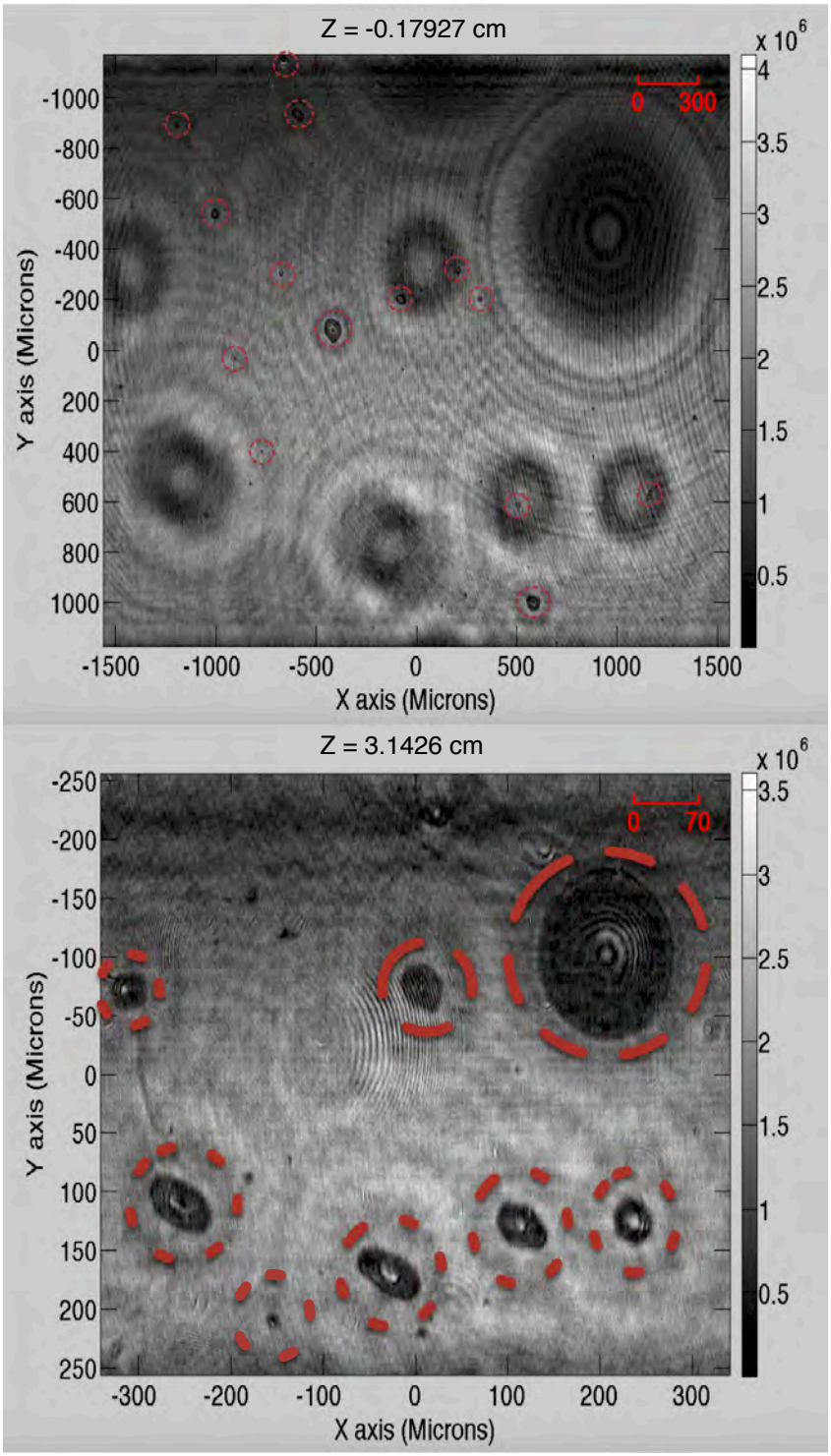

Fig. 5.3 Reconstructed 3D image at two depth positions at which cloud particles were identified. The particles are identified by the in focus dark regions against the lighter background and some of the larger particles are highlighted with red bounding circles.

The particles shown in Figure 5.3 have been impacted on the front and back sampling windows of the instrument and should therefore be analysed separately to the pristine particles identified within the sampling volume. Such a separation is simple to undertake since the depths of the sampling windows are known and hence particles reconstructed at these depths can be differentiated from those reconstructed at other depths within the sampling volume. Particles on the window surfaces persist for longer than particles travelling through the sampling volume and hence this allows the study of processes such as the evaporation rate of the water droplets with time. If it is desired to only detect pristine particles, a hydrophobic coating could be used on the sampling window; however, the optical properties of such a coating would need to be investigated to determine what effect this would have on the transmitted laser beam which could affect the reconstruction performance.

A number of particles with sizes ranging between approximately 6 microns and 100 microns are seen on the front sampling window and particles with sizes from 10 to 300 microns are seen on the farther window. The 300 micron spherical particle seen on the farther window is consistent with the detection of a large spherical rain droplet whereas the other aspherical particles could be either impacted rain/water droplets or irregular ice crystals on the window surface.

A collection of pristine particles identified at various times during the cloud events are presented in Figure 5.4. Of the particles identified, many can be classified as either spherical or irregular with sizes ranging from a few microns up to approximately 30 microns. This is consistent with the detection of small, spherical water droplets along with small irregular ice crystals. The observed size variation is in agreement with typical cloud particle sizes.

The holographic observations can be compared to collocated measurements from the Polarsonde instrument. This instrument emits linearly polarised light at two different polarisation angles into the cloud. The backscattered light that returns to the detector is then measured using photodiode detectors with polarising filters to separate the returning light into polarised components that are parallel and orthogonal to the transmitted polarisation. This allows the linear depolarisation of the light to be measured which is sensitive to the shape properties of the scattering particles. The interpretation of this data is an ongoing subject of research and hence comparison between the Polarsonde observations and the direct imaging results from the holographic instrument was one of the goals of this field testing.

Figure 5.5 shows the Polarsonde observations during the same time period in which the cloud particles shown in Figure 5.3 and Figure 5.4 were identified in the holographic dataset. This event occurred at 11.6802 days (UTC relative to 1/8/2016). The grey and green traces show the raw backscattered signals for each of the polarisation channels. These signals are larger than zero which implies that a scattering target was present for the duration of this

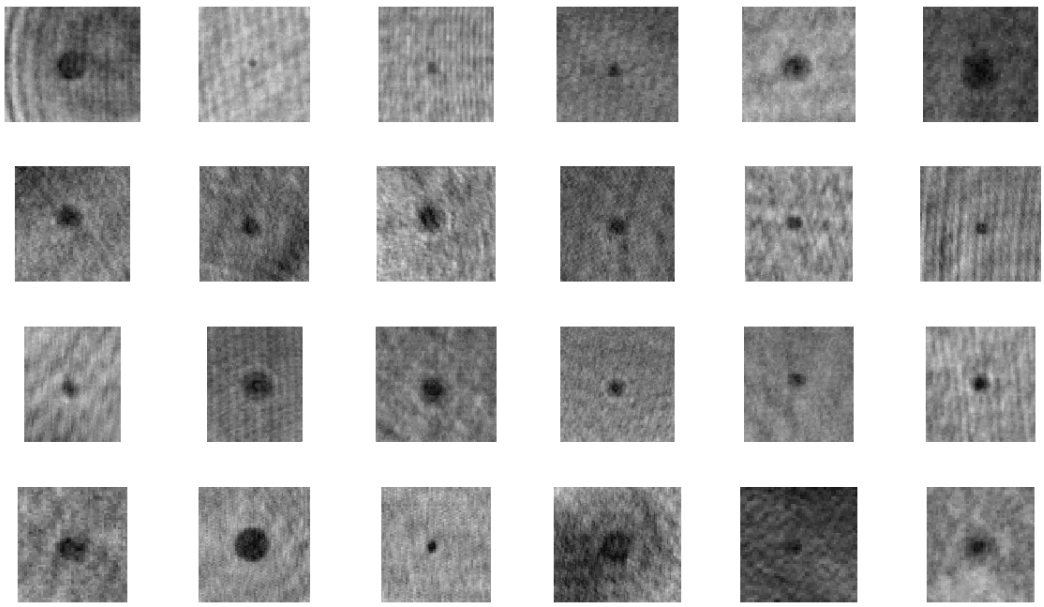

Fig. 5.4 Various pristine cloud particles observed during the identified cloud events.

observation period. This suggests that a cloud was present during this time as confirmed in the holographic dataset in which cloud particles were detected. The red and blue traces show the linear depolarisation for each of the transmitted polarisations. The interpretation of depolarisation measurements is still an open research question; however, insights can be inferred based on results from Monte Carlo scattering simulations that have been undertaken (M. Hamilton, private communication). The low depolarisation signals are consistent with the presence of spherical water droplets and this also provides evidence to exclude the presence of aggregated ice crystals which are expected to produce a somewhat larger depolarisation signature. This is in agreement with the holographic observations in Figure 5.3 in which spherical water droplets are observed and complicated crystal aggregates are not seen. The depolarisation properties of the irregularly shaped particles in the holographic dataset are not yet understood and so further analysis is required to compare these particular results in more detail.

The holographic dataset is currently being analysed manually to determine suitable intensity thresholds to be used with the developed automated analysis software to automatically extract the particle shape, size and spatial distributions. Once this is working efficiently, the entire dataset can then be studied and the evolution of the microphysical properties can then be studied as a function of the external meteorological conditions and time. Correlations between properties such as the effective particle diameter or the particle shape distribution properties with meteorological parameters, such as temperature and relative humidity, would

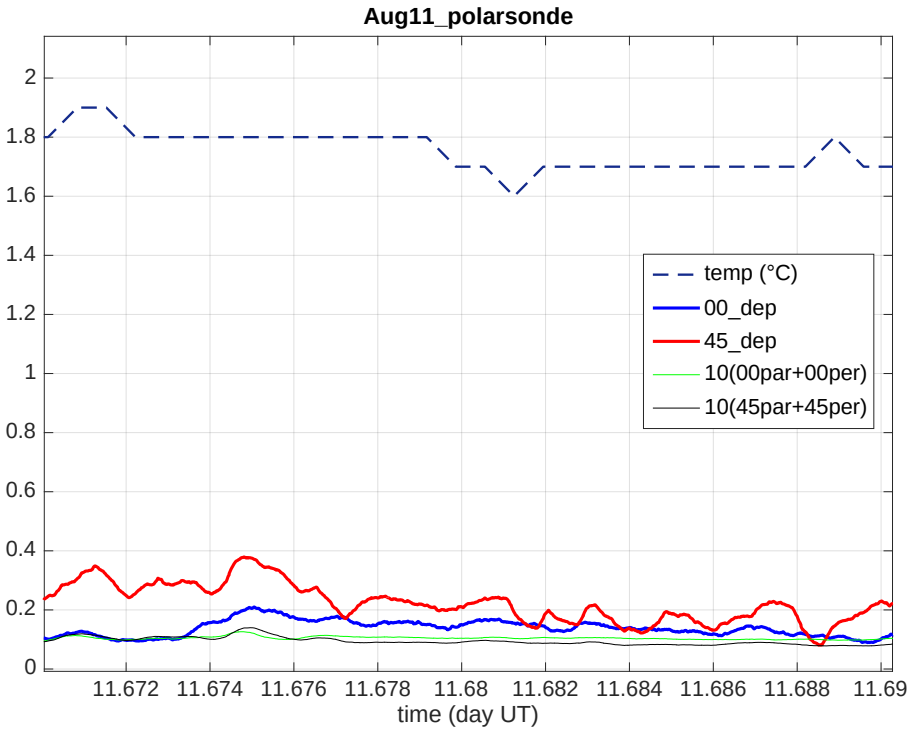

Fig. 5.5 Polarsonde observations taken at the same time as the holographic observations shown in Figure 5.3. The green and grey traces show the raw backscattered signal for each polarisation channel and the red and blue traces show the depolarisation for each channel. The dotted blue line shows the temperature observations from the weather station. Figure courtesy of M. Hamilton.

allow these microphysical properties to be parametrised by the simpler properties, such as temperature, which are significantly easier to represent in climate models.

Chapter 6

Conclusion

6.1 Conclusion

In this thesis, the development and experimental testing of a low cost, light weight digital holographic imager suitable for the study of cloud microphysics has been presented. A broad overview of the resolution constraints involved in designing a holographic imager for cloud studies is presented and has been used to optimise the design aspects of this particular system. The instrument performance aspects such as resolution, operational stability and control system response have been measured and tested experimentally under both laboratory conditions and through field testing at a Tasmanian mountain field site alongside collocated instruments. A number of cloud events were identified in the field testing dataset and cloud particles of varying sizes and shapes have been successfully identified and measured, providing confirmation that the instrument can operate autonomously in cloud conditions whilst being both low cost and robust, as required for tower deployments over widespread regions and for weather balloon deployments.

The instrument hardware systems developed include a high speed triggering circuit, a laser pulse amplifier based on a MOSFET gate driver, a PID temperature control system and an instrument enclosure suitable for reliable operation within a cloud. The developed software elements include a simulation for determining the effect of system parameters such as camera sensor size on holographic imaging performance, automated system control software suitable for ARM Linux operation, diffraction based 3D image reconstruction software, automated analysis software for the extraction of particle properties from 3D images and various simulations of the other system performance aspects. All system aspects have been designed to be modular and easily reconfigured to allow different experiments to be undertaken and future upgrades to be simply achieved.

6.2 Future Work

In this project, a low cost holographic imaging instrument has been designed and experimentally tested in both laboratory conditions and through a field study at a mountain site. The instrument was seen to operate effectively and hence the proof of principle of its operation has been confirmed. Future work could fall within the two broadly defined paths of either improving the underlying hardware and software systems of the instrument or using the instrument for the scientific study of cloud microphysical processes.

The automated analysis algorithm has been shown to work for laboratory testing conditions; however, further development is needed to apply this analysis to the field testing data. This will require manual analysis of the dataset to determine suitable intensity thresholds to separate particles from the background noise, or investigation of alternate approaches such as machine learning algorithms. Once this has been improved, the automated analysis algorithm can then be used to study the entire dataset alongside observations from the collocated weather station and Polarsonde instrument.

The PID temperature control system has been demonstrated to operate effectively in experimental testing conditions. The performance of this feedback system depends on the thermal properties of the instrument along with the external cooling properties of the environment in which it is deployed. Modelling of these effects could be undertaken to optimise the gain stages of the analogue PID circuit, to minimise convergence time to the desired system temperature. The use of a digital PID controller using the included Arduino microcontroller could also be investigated as a potentially self calibrating alternative through software.

The instrument was designed to be modular and allows variation of many aspects such as the laser diode, camera, sampling volume size and image magnification. Different field testing experiments could be undertaken in these other operation modes to test the performance of each setup. One such possibility would be to use a collimating aspheric lens to reduce the divergence of the laser diode beam and hence allow a significantly larger sampling volume to be obtained, without the need for a greater laser power. The Raspberry Pi computer could also be replaced with a more modern mini computer to improve the data transfer rate. This would allow holographic videos to be created with frame rates of upwards of 30fps which could potentially allow the trajectories of cloud particles to be studied, providing potential insights into the microscale turbulence properties of the cloud.

The use of more complicated laser beam geometries such as an off axis holographic setup or the use of mirrors to allow the reference beam to be guided through the sampling volume from multiple directions could be investigated due to the modular design. The off axis detection geometry would allow artefacts due to the overlaid twin image noise source

to be filtered out in a simple manner, to improve the reconstruction quality. The multiple pass geometry would allow information about multiple orientations of a single particle to be studied as opposed to the single viewing orientation provided by the simple in line geometry presently used.

The intensity of the reconstructed object wave was primarily analysed in this work. The digital holographic method also allows the optical phase of the wavefront to be reconstructed and the reconstruction algorithm has been designed to extract this in a simple manner. The phase distribution would in principle allow nanometre scale depth variations in the image to be quantitatively measured to within a 2π phase ambiguity. The reconstructed wavefront phase may therefore contain information about the surface roughness properties of the detected ice crystals which would be of significant interest as this is an important factor in determining the optical properties of clouds in climate models. It is also possible that studies of the Arago diffraction spot observed in reconstructions of larger cloud particles could provide surface roughness information, as such a dependence is theoretically expected.

A range of scientific observations are possible with this instrument on top of those previously discussed. Due to the low cost design, many of these instruments could be realistically manufactured and a network of holographic observations could be obtained. This could be undertaken either at a single site to study the large scale structure of a cloud as it passes through the tower mounted instruments or the devices could be deployed at different locations to study how these cloud processes vary between multiple sites. Possible tower based studies that could be undertaken would include the analysis of the time evolution of the cloud particle observables of low lying clouds and fog as a function of the local meteorological conditions, as well as studies of falling snow particles and their clustering behaviour. Balloon based observations could be undertaken to provide insights into poorly understood phenomena such as microscale turbulence effects within clouds, thunderstorm processes and lightning generation mechanisms due to cloud particle interactions. Direct cloud particle observations during these events could then be compared to collocated instruments such as radar and LIDAR to gain further insight into these complex processes.

References

[1] Mischenko, M., Travis, L. & Lacis, A. *Scattering, absorption, and emission of light by small particles* (Cambridge University Press, Cambridge, 2002).

[2] Takano, Y. & Liou, K.-N. Solar Radiative Transfer in Cirrus Clouds. Part I: Single-Scattering and Optical Properties of Hexagonal Ice Crystals. *Journal of the Atmospheric Sciences* **46**, 3–19 (1989).

[3] Takano, Y., Takano, Y., Liou, K.-N. & Liou, K.-N. Solar radiative transfer in cirrus clouds. Part II: Theory and computation of multiple scattering in an anisotropic medium. *Journal of the Atmospheric Sciences* **46**, 20–36 (1989).

[4] Takano, Y. & Liou, K. N. Radiative Transfer in Cirrus Clouds. Part III: Light Scattering by Irregular Ice Crystals. *Journal of the Atmospheric Sciences* **52**, 818–837 (1995).

[5] Ramanathan, V., Crutzen, P. J., Kiehl, J. T. & Rosenfeld, D. Aerosols, Climate, and the Hydrological Cycle. *Science* **294**, 2119–2124 (2001).

[6] Huntington, T. G. Evidence for intensification of the global water cycle: Review and synthesis. *Journal of Hydrology* **319**, 83–95 (2006).

[7] Rossow, W. B. Cloud microphysics: Analysis of the clouds of Earth, Venus, Mars and Jupiter. *Icarus* **36**, 1–50 (1978).

[8] Kulmala, M. *et al.* Introduction: European Integrated Project on Aerosol Cloud Climate and Air Quality interactions (EUCAARI)-integrating aerosol research from nano to global scales. *Atmospheric Chemistry and Physics* **9**, 2825–2841 (2009).

[9] Stubenrauch, C. J. *et al.* Assessment of global cloud datasets from satellites. *Bulletin of the American Meteorological Society* **94**, 1031–1049 (2013).

[10] Liou, K. N. K.-N. Influence of cirrus clouds on weather and climate processes A global perspective. *Monthly Weather Review* **114**, 1167–1199 (1986).

[11] Cao, Y., Wu, Z., Su, Y. & Xu, Z. Aircraft flight characteristics in icing conditions. *Progress in Aerospace Sciences* **74**, 62–80 (2015).

[12] Cebeci, T. & Kafyeke, F. Aircraft Icing. *Annual Review of Fluid Mechanics* **35**, 11–21 (2003).

[13] Bernlohr, K. Impact of atmospheric parameters on the atmospheric Cherenkov technique. *Astroparticle Physics* **12**, 255–268 (2000).

[14] Saunders, C. P. R. A Review of Thunderstorm Electrification Processes. *Journal of Applied Meteorology* **32**, 642–655 (1993).

[15] Baker, M. B. Cloud Microphysics and Climate. *Science* **276**, 1072–1078 (1997).

[16] Baran, A. J. A review of the light scattering properties of cirrus. *Journal of Quantitative Spectroscopy and Radiative Transfer* **110**, 1239–1260 (2009).

[17] Heymsfield, A. J. *et al.* A General Approach for Deriving the Properties of Cirrus and Stratiform Ice Cloud Particles. *Journal of the Atmospheric Sciences* **59**, 3–29 (2002).

[18] Baker, M. B. & Peter, T. Small-scale cloud processes and climate. *Nature* **451**, 299–300 (2008).

[19] Barker, H. W., Cole, Jason, N. S., Li, J., Yi, B. & Yang, P. Estimation of Errors in Two-Stream Approximations of the Solar Radiative Transfer Equation for Cloudy-Sky Conditions. *Journal of the Atmospheric Sciences* 4053–4074 (2015).

[20] Webb, M., Senior, C., Bony, S. & Morcrette, J. J. Combining ERBE and ISCCP data to assess clouds in the Hadley Centre, ECMWF and LMD atmospheric climate models. *Climate Dynamics* **17**, 905–922 (2001).

[21] Curry, J. A. *et al.* FIRE arctic clouds experiment. *Bulletin of the American Meteorological Society* **81**, 5–29 (2000).

[22] Shupe, M. D. Clouds at Arctic Atmospheric Observatories. Part II: Thermodynamic Phase Characteristics. *Journal of Applied Meteorology and Climatology* **50**, 645–661 (2011).

[23] Shupe, M. D. & Intrieri, J. M. Cloud radiative forcing of the Arctic surface: The influence of cloud properties, surface albedo, and solar zenith angle. *Journal of Climate* **17**, 616–628 (2004).

[24] Flato, G., Marotzke, J., Abiodun, B., Braconnot, P., Chou, S., Collins, W., Cox, P., Driouech, F., Emori, S., Eyring, V., Forest, C., Gleckler, P., Guilyardi, E., Jakob, C., Kattsov, V., Reason, C., and Rummukainen, M. Evaluation of Climate Models, in: Climate Change 2013: The Physical Science Basis. Contribution of Working Group I to the Fifth Assessment Report of the Intergovernmental Panel on Climate Change. Tech. Rep. (2013).

[25] Schultz, C. J., Petersen, W. a. & Carey, L. D. Lightning and Severe Weather: A Comparison between Total and Cloud-to-Ground Lightning Trends. *Weather and Forecasting* **26**, 744–755 (2011).

[26] Stolzenburg, M., Rust, W. D. & Marshall, T. C. Electical structure in thunderstorm convective regions: 2. Isolated Storms. *Journal of Geophysical Research* **103**, 14,079–14,096 (1998).

[27] Shaw, R. A. Particle-Turbulence Interactions in Atmospheric Clouds. *Annual Review of Fluid Mechanics* **35**, 183–227 (2003).

[28] Brooks, I., Saunders, C., Mitzeva, R. & Peck, S. The effect on thunderstorm charging of the rate of rime accretion by graupel. *Atmospheric Research* **43**, 277–295 (1997).

[29] Saunders, C. P. R., Keith, W. D. & Mitzeva, R. P. The Effect of Liquid Water on Thunderstorm Charging. *Journal of Geophysical Research* **96**, 11007–1017 (1991).

[30] Houze Jr., R. A. *Cloud Dynamics* (1993).

[31] Gimeno, L. Grand challenges in atmospheric science. *Frontiers in Earth Science* **1**, 1–5 (2013).

[32] Dwyer, J. R. & Uman, M. A. The physics of lightning. *Physics Reports* **534**, 147–241 (2014).

[33] Dwyer, J. R., Smith, D. M. & Cummer, S. A. High-energy atmospheric physics: Terrestrial gamma-ray flashes and related phenomena. *Space Science Reviews* **173**, 133–196 (2012).

[34] Marsh, N. D. & Svensmark, H. Low cloud properties influenced by cosmic rays. *Physical Review Letters* **85**, 5004–5007 (2000).

[35] Lyu, F. *et al.* Ground detection of terrestrial gamma ray flashes from distant radio signals. *Geophysical Research Letters* 8728–8734 (2016).

[36] Kristiansen, J. Is there a cosmic ray signal in recent variations in global cloudiness and cloud radiative forcing? *Journal of Geophysical Research* **105**, 11,851–11863 (2000).

[37] Aab, A. *et al.* The Pierre Auger Cosmic Ray Observatory. *Nuclear Instruments and Methods in Physics Research, Section A: Accelerators, Spectrometers, Detectors and Associated Equipment* **798**, 172–213 (2015).

[38] Doro, M., Daniel, M., Reyes, R. D. L., Gaug, M. & Maccarone, M. C. Strategy implementation for the CTA Atmospheric monitoring program. *EPJ Web of Conferences* **89**, 02005 (2015).

[39] BenZvi, S. Y. *et al.* Measurement of the aerosol phase function at the Pierre Auger Observatory. *Astroparticle Physics* **28**, 312–320 (2007).

[40] Nolan, S. J., Pühlhofer, G. & Rulten, C. B. Detailed studies of atmospheric calibration in imaging Cherenkov astronomy. *Astroparticle Physics* **34**, 304–313 (2010). arXiv:1009.0517.

[41] Iyer, A. R. *et al.* A CHARACTERISTIC TRANSMISSION SPECTRUM DOMINATED BY H2O APPLIES TO THE MAJORITY OF HST /WFC3 EXOPLANET OBSERVATIONS. *The Astrophysical Journal* **823**, 109 (2016).

[42] Kreidberg, L. *et al.* Clouds In The Atmosphere Of The Super-Earth Exoplanet GJ1214b. *Nature* **505**, 69–72 (2014).

[43] Kaltenegger, L., Traub, W. A. & Jucks, K. W. Spectral evolution of an Earth like planet. *The Astronomical Journal* **658**, 598–616 (2007).

[44] Jones, E. G. & Lineweaver, C. H. Using the phase diagram of liquid water to search for life. *Australian Journal of Earth Sciences* **59**, 253–262 (2012).

[45] Connolly, P. J. *et al.* Calibration of the cloud particle imager probes using calibration beads and ice crystal analogs: The depth of field. *Journal of Atmospheric and Oceanic Technology* **24**, 1860–1879 (2007).

[46] Dye, J. E. & Baumgardner, D. Evaluation of the Forward Scattering Spectrometer Probe. Part I: Electronic and Optical Studies. *Journal of Atmospheric and Oceanic Technology* **1**, 329–344 (1984).

[47] Baumgardner, D. *et al.* Airborne instruments to measure atmospheric aerosol particles, clouds and radiation: A cook's tour of mature and emerging technology. *Atmospheric Research* **102**, 10–29 (2011).

[48] Schnars, U. & Juptner, W. Digital recording and numerical reconstruction of holograms. *Measurement Science & Technology* **13**, 17 (2002).

[49] Colomb, T. *et al.* Automatic procedure for aberration compensation in digital holographic microscopy and applications to specimen shape compensation. *Applied optics* **45**, 851–863 (2006).

[50] Spuler, S. M. & Fugal, J. Design of an in-line, digital holographic imaging system for airborne measurement of clouds. *Applied optics* **50**, 1405–1412 (2011).

[51] Henneberger, J., Fugal, J. P., Stetzer, O. & Lohmann, U. HOLIMO II: a digital holographic instrument for ground-based in situ observations of microphysical properties of mixed-phase clouds. *Atmospheric Measurement Techniques* **6**, 2975–2987 (2013).

[52] Beck, A., Henneberger, J., Schöpfer, S. & Lohmann, U. HoloGondel: in-situ cloud observations on a cable car in the Swiss Alps using a holographic imager. *Atmospheric Measurement Techniques Discussions* **25**, 1–26 (2016).

[53] Beals, M. J. *et al.* Holographic measurements of inhomogeneous cloud mixing at the centimeter scale. *Science (New York, N.Y.)* **350**, 87–90 (2015).

[54] Pruppacher, H. R. & Klett, J. D. *Microphysics of Clouds and Precipitation* (Springer Dordrecht, Heidelberg, 2010).

[55] Wallace, J. M. & Hobbs, P. V. *Atmospheric Science: An Introductory Survey* (Academic Press, New York, 2006).

[56] Andrews, D. *An Introduction to Atmospheric Physics* (Cambridge University Press, Cambridge, 2010).

[57] Lohmann, U. & Feichter, J. Global indirect aerosol effects: a review. *Atmospheric Chemistry and Physics Discussions* **4**, 7561–7614 (2004).

[58] Harrison, E. F. *et al.* Seasonal Variation of Cloud Radiative Forcing Derived From the Earth Radiation Budget Experiment. *Journal of Geophysical Research* **95703**, 687–18 (1990).

[59] Wylie, D., Jackson, D. L., Menzel, W. P. & Bates, J. J. Trends in global cloud cover in two decades of HIRS observations. *Journal of Climate* **18**, 3021–3031 (2005).

[60] Kirkby, J. *et al.* Role of sulphuric acid, ammonia and galactic cosmic rays in atmospheric aerosol nucleation. *Nature* **476**, 429–433 (2011).

[61] Svensmark, H. & Friis-Christensen, E. Variation of cosmic ray flux and global cloud coverage—a missing link in solar-climate relationships. *Journal of Atmospheric and Solar-Terrestrial Physics* **59**, 1225–1232 (1997).

[62] Kirkby, J. *et al.* Ion-induced nucleation of pure biogenic particles. *Nature* **533**, 521–525 (2016).

[63] Berry, E. Cloud Droplet Growth by Collection. *Journal of the Atmospheric Sciences* **24**, 688–701 (1967).

[64] Gillespie, D. T. The Stochastic Coalescence Model for Cloud Droplet Growth. *Journal of the Atmospheric Sciences* **29**, 1496–1510 (1972).

[65] Beard, K. V. & Ochs III, H. T. Warm-Rain Initiation: An Overview of Microphysical Mechanisms. *Journal of Applied Meteorology* **32**, 608–625 (1993).

[66] Falkovich, G., Fouxon, A. & Stepanov, M. G. Acceleration of rain initiation by cloud turbulence. *Nature* **419**, 151–154 (2002).

[67] Johnson, D. B. The Role of Giant and Ultragiant Aerosol Particles in Warm Rain Initiation. *Journal of the Atmospheric Sciences* **39**, 448–460 (1982).

[68] Feingold, G., Cotton, W. R., Kreidenweis, S. M. & Davis, J. T. The Impact of Giant Cloud Condensation Nuclei on Drizzle Formation in Stratocumulus: Implications for Cloud Radiative Properties. *Journal of the Atmospheric Sciences* **56**, 4100–4117 (1999).

[69] Cooper, W. a., Lasher-Trapp, S. G. & Blyth, A. M. The Influence of Entrainment and Mixing on the Initial Formation of Rain in a Warm Cumulus Cloud. *Journal of the Atmospheric Sciences* **70**, 1727–1743 (2013).

[70] Murray, B. J., Malkin, T. L. & Salzmann, C. G. The crystal structure of ice under mesospheric conditions. *Journal of Atmospheric and Solar-Terrestrial Physics* **127**, 78–82 (2014).

[71] Murray, B. J., Knopf, D. A. & Bertram, A. K. The formation of cubic ice under conditions relevant to earth's atmosphere. *Nature* **434**, 202–205 (2005).

[72] Whalley, E. Scheiner's Halo: Evidence for Ice Ic in the Atmosphere. *Science* **211**, 389–390 (1981).

[73] Koop, T., Luo, B., Tsias, A. & Peter, T. Water activity as the determinant for homogeneous ice nucleation in aqueous solutions. *Nature* **406**, 611–614 (2000).

[74] Rosenfeld, D. & Woodley, W. Deep convective clouds with sustained supercooled liquid water down to -37.5 degrees C. *Nature* **405**, 440–2 (2000).

[75] Wang, B. *et al.* The deposition ice nucleation and immersion freezing potential of amorphous secondary organic aerosol: Pathways for ice and mixed-phase cloud formation. *Journal of Geophysical Research Atmospheres* **117**, 1–12 (2012).

[76] Heymsfield, A. J. *et al.* Homogeneous ice nucleation in subtropical and tropical convection and its influence on cirrus anvil microphysics. *Journal of the Atmospheric Sciences* **62**, 41–64 (2005).

[77] McFarquhar, G. M. *et al.* Ice properties of single-layer stratocumulus during the Mixed-Phase Arctic Cloud Experiment: 1. Observations. *Journal of Geophysical Research Atmospheres* **112**, 1–25 (2007).

[78] DeMott, P. J. *et al.* Predicting global atmospheric ice nuclei distributions and their impacts on climate. *Proceedings of the National Academy of Sciences of the United States of America* **107**, 11217–22 (2010).

[79] Abbatt, J. P. D. *et al.* Solid Ammonium Sulfate Aerosols as Ice Nuclei: A Pathway for Cirrus Cloud Formation. *Science* **313**, 1770–1773 (2006).

[80] Isono, K., Komabayasi, M. & Ono, A. The nature and origin of ice nuclei in the atmosphere. *Journal of the Meteorological Society of Japan* **37**, 211–233 (1959).

[81] Chen, J.-P. & Lamb, D. The Theoretical Basis for the Parameterization of Ice Crystal Habits: Growth by Vapor Deposition. *Journal of the Atmospheric Sciences* **51**, 1206–1222 (1994).

[82] Ono, A. The Shape and Riming Properties of Ice Crystals in Natural Clouds. *Journal of the Atmospheric Sciences* **26**, 138–147 (1969).

[83] Cotton, W. R., Tripoli, G. J., Rauber, R. M. & Mulvihill, E. A. Numerical Simulation of the Effects of Varying Ice Crystal Nucleation Rates and Aggregation Processes on Orographic Snowfall. *Journal of Climate and Applied Meteorology* **25**, 1658–1680 (1986).

[84] Lawson, R. P., Baker, B., Pilson, B. & Mo, Q. In Situ Observations of the Microphysical Properties of Wave, Cirrus, and Anvil Clouds. Part II: Cirrus Clouds. *Journal of the Atmospheric Sciences* **63**, 3186–3203 (2006).

[85] Magono, C. & Lee, C. Meteorological Classification of Natural Snow Crystals. *Journal of the Faculty of Science, Hokkaido University* **2**, 321–335 (1966).

[86] Heymsfield, A. J., Schmitt, C., Bansemer, A. & Twohy, C. H. Improved Representation of Ice Particle Masses Based on Observations in Natural Clouds. *Journal of the Atmospheric Sciences* **67**, 3303–3318 (2010).

[87] Libbrecht, K. G. The physics of snow crystals. *Reports on Progress in Physics* **68**, 855–895 (2005).

[88] Shupe, M. D. *et al.* High and Dry: New Observations of Tropospheric and Cloud Properties above the Greenland Ice Sheet. *Bulletin of the American Meteorological Society* **94**, 169–186 (2013).

[89] Sikand, M. *et al.* Estimation of Mixed-Phase Cloud Optical Depth and Position Using In Situ Radiation and Cloud Microphysical Measurements Obtained from a Tethered-Balloon Platform. *Journal of the Atmospheric Sciences* **70**, 317–329 (2013).

[90] Fan, J. *et al.* Representation of Arctic mixed-phase clouds and the Wegener-Bergeron-Findeisen process in climate models: Perspectives from a cloud-resolving study. *Journal of Geophysical Research* **116**, 1–17 (2011).

[91] Morrison, H. *et al.* Resilience of persistent Arctic mixed-phase clouds. *Nature Geoscience* **5**, 11–17 (2011).

[92] Korolev, A. Limitations of the Wegener–Bergeron–Findeisen Mechanism in the Evolution of Mixed-Phase Clouds. *Journal of the Atmospheric Sciences* **64**, 3372–3375 (2007).

[93] Verlinde, J., Harrington, J., McFarquhar, G. & Al., E. The mixed-phase Arctic cloud experiment. *American Meteorological Society* 205–221 (2007).

[94] Waterman, P. Symmetry, Unitarity, and geometry in electomagnetic scattering. *Physical review D* **19**, 101–104 (1971).

[95] Yang, P. *et al.* Spectrally Consistent Scattering, Absorption, and Polarization Properties of Atmospheric Ice Crystals at Wavelengths from 0.2 to 100 μ m. *Journal of the Atmospheric Sciences* **70**, 330–347 (2013).

[96] Sun, Z. & Shine, K. P. Parameterization of ice cloud radiative properties and its application to the potential climatic importance of mixed-phase clouds. *Journal of Climate* **8**, 1874–1888 (1995).

[97] Gultepe, I. *et al.* A review on ice fog measurements and modeling. *Atmospheric Research* (2014).

[98] Girard, E. & Blanchet, J.-P. Microphysical Parameterization of Arctic Diamond Dust, Ice Fog, and Thin Stratus for Climate Models. *Journal of the Atmospheric Sciences* **58**, 1181–1198 (2001).

[99] Ramanathan, V. *et al.* Cloud-Radiative Forcing and Climate: Results from the Earth Radiation Budget Experiment. *Science* **243**, 57–63 (1989).

[100] Kay, J. E. *et al.* Exposing global cloud biases in the Community Atmosphere Model (CAM) using satellite observations and their corresponding instrument simulators. *Journal of Climate* **25**, 5190–5207 (2012).

[101] Lohmann, U. & Roeckner, E. Influence of cirrus cloud radiative forcing on climate and climate sensitivity in a general circulation model. *Journal of Geophysical Research* **100**, 16305 (1995).

[102] Hansen, J. *et al.* Climate Sensitivity: Analysis of Feedback Mechanisms. *Climate Processes and Climate Sensitivity* **29**, 130–163 (1984).

[103] Baran, A. J. *et al.* A self-consistent scattering model for cirrus. II: The high and low frequencies. *Quarterly Journal of the Royal Meteorological Society* **140**, 1039–1057 (2014).

[104] Key, J. R., Yang, P., Baum, B. A. & Nasiri, S. L. Parameterization of shortwave ice cloud optical properties for various particle habits. *Journal of Geophysical Research Atmospheres* **107**, 1–10 (2002).

[105] Yi, B. *et al.* Influence of ice particle surface roughening on the global cloud radiative effect. *J. Atmos. Sci.* **70**, 2794–2807 (2013).

[106] Draine, B. T. & Flatau, P. J. Discrete-dipole approximation for scattering calculations. *Journal of the Optical Society of America A* **11**, 1491–1499 (1994).

[107] Bi, L. & Yang, P. Accurate simulation of the optical properties of atmospheric ice crystals with the invariant imbedding T-matrix method. *Journal of Quantitative Spectroscopy and Radiative Transfer* **138**, 17–35 (2014).

[108] Yang, P. *et al.* Scattering and absorption property database for nonspherical ice particles in the near- through far-infrared spectral region. *Applied optics* **44**, 5512–5523 (2005).

[109] Heymsfield, A. J. *et al.* Observations and Parameterizations of Particle Size Distributions in Deep Tropical Cirrus and Stratiform Precipitating Clouds: Results from In Situ Observations in TRMM Field Campaigns. *Journal of the Atmospheric Sciences* **59**, 3457–3491 (2002).

[110] Baum, B. A. *et al.* Bulk Scattering Properties for the Remote Sensing of Ice Clouds. Part I: Narrowband Models. *Journal of Applied Meteorology* **44**, 1896–1911 (2005).

[111] Heymsfield, A. J., Schmitt, C. & Bansemer, A. Ice Cloud Particle Size Distributions and Pressure-Dependent Terminal Velocities from In Situ Observations at Temperatures from 0C to -86C. *Journal of the Atmospheric Sciences* **70**, 4123–4154 (2013).

[112] Schumann, U., Mayer, B., Graf, K. & Mannstein, H. A parametric radiative forcing model for contrail cirrus. *Journal of Applied Meteorology and Climatology* **51**, 1391–1406 (2012).

[113] Stephens, G. L. & Kummerow, C. D. The remote sensing of clouds and precipitation from space: a review. *Journal of the Atmospheric Sciences* **64**, 3742–3765 (2007).

[114] Baum, B. A. *et al.* Improvements in shortwave bulk scattering and absorption models for the remote sensing of ice clouds. *Journal of Applied Meteorology and Climatology* **50**, 1037–1056 (2011).

[115] Baum, B. A., Heymsfield, A. J., Yang, P. & Bedka, S. T. Bulk Scattering Properties for the Remote Sensing of Ice Clouds. Part II: Narrowband Models. *Journal of Applied Meteorology* **44**, 1885–1895 (2005).

[116] Yang, P. *et al.* On the Radiative Properties of Ice Clouds : Light Scattering , Remote Sensing , and Radiation Parameterization. *Advances in Atmospheric Sciences* **32**, 32–63 (2015).

[117] Emde, C. *et al.* The libRadtran software package for radiative transfer calculations (version 2.0.1). *Geoscientific Model Development* **9**, 1647–1672 (2016).

[118] Cooper, S. J., L'Ecuyer, T. S., Gabriel, P., Baran, A. J. & Stephens, G. L. Performance assessment of a five-channel estimation-based ice cloud retrieval scheme for use over the global oceans. *Journal of Geophysical Research Atmospheres* **112**, 1–19 (2007).

[119] Schnaiter, M. *et al.* Influence of particle size and shape on the backscattering linear depolarisation ratio of small ice crystals – cloud chamber measurements in the context of contrail and cirrus microphysics. *Atmospheric Chemistry and Physics* **12**, 10465–10484 (2012).

[120] Winker, D. M. *et al.* The Calipso Mission: A Global 3D View of Aerosols and Clouds. *Bulletin of the American Meteorological Society* **91**, 1211–1229 (2010).

[121] Sassen, K. & Liou, K.-N. Scattering of Polarized Laser Light by Water Droplet, Mixed-Phase and Ice Crystal Clouds. Part I: Angular Scattering Patterns. *Journal of the Atmospheric Sciences* **36**, 838–851 (1979).

[122] Avery, M. *et al.* Cloud ice water content retrieved from the CALIOP space-based lidar. *Geophysical Research Letters* **39**, 2–7 (2012).

[123] Wang, Z. & Sassen, K. Cirrus Cloud Microphysical Property Retrieval Using Lidar and Radar Measurements. Part I: Algorithm Description and Comparison with In Situ Data. *Journal of Applied Meteorology* **41**, 218–229 (2002).

[124] Delanoë, J. *et al.* Comparison of airborne in situ, airborne radar-lidar, and spaceborne radar-lidar retrievals of polar ice cloud properties sampled during the POLARCAT campaign. *Journal of Atmospheric and Oceanic Technology* **30**, 57–73 (2013).

[125] Sekelsky, S. M., Ecklund, W. L., Firda, J. M., Gage, K. S. & McIntosh, R. E. Particle Size Estimation in Ice-Phase Clouds Using Multifrequency Radar Reflectivity Measurements at 95, 33, and 2.8 GHz. *Journal of Applied Meteorology* **38**, 5–28 (1999).

[126] Cahalan, R. F., McGill, M., Kolasinski, J., Várnai, T. & Yetzer, K. THOR - Cloud Thickness from Offbeam Lidar Returns. *Journal of Atmospheric and Oceanic Technology* **22**, 605–627 (2005).

[127] Shupe, M. D. The Status of Ground-Based Observational Methods. *American Meteorological Society* (2008).

[128] Hogan, R. & Francis, P. Characteristics of mixed-phase clouds. I: Lidar, radar and aircraft observations from CLARE98. *Royal Meteorological Society* **129** (2003).

[129] Botta, G., Aydin, K. & Verlinde, J. Variability in millimeter wave scattering properties of dendritic ice crystals. *Journal of Quantitative Spectroscopy & Radiative Transfer* **131**, 105–114 (2013).

[130] Wang, Z. *et al.* Single aircraft integration of remote sensing and in situ sampling for the study of cloud microphysics and dynamics. *Bulletin of the American Meteorological Society* **93**, 653–668 (2012).

[131] Fugal, J. P., Shaw, R. a., Saw, E. W. & Sergeyev, A. V. Airborne digital holographic system for cloud particle measurements. *Applied optics* **43**, 5987–5995 (2004).

[132] Barbet, C. *et al.* Modeling organic aerosol composition at the puy de Dôme mountain (France) for two contrasted air masses with the WRF-Chem model. *Atmospheric Chemistry and Physics Discussions* **15**, 13395–13455 (2015).

[133] Marlton, G. J., Harrison, R. G., Nicoll, K. A. & Williams, P. D. Note : A balloon-borne accelerometer technique for measuring atmospheric turbulence. *Review of Scientific Instruments* **86**, 14–16 (2015).

[134] Nagaraja Rao, C. Balloon measurements of the polarization of light diffusely reflected by the earth's atmosphere. *Planetary and Space Science* **17**, 1307–1309 (1969).

[135] Hagan, D. E. *et al.* Validating AIRS upper atmosphere water vapor retrievals using aircraft and balloon in situ measurements. *Geophysical Research Letters* **31**, 10–13 (2004).

[136] Greenberg, J. P. *et al.* Tethered balloon measurements of biogenic VOCs in the atmospheric boundary layer. *Atmospheric Environment* **33**, 855–867 (1999).

[137] Korolev, A. & Field, P. R. Assessment of the performance of the inter-arrival time algorithm to identify ice shattering artifacts in cloud particle probe measurements. *Atmospheric Measurement Techniques* **8**, 761–777 (2015).

[138] Wergin, W. P., Rango, a. & Erbe, E. F. Image comparisons of snow and ice crystals photographed by light (video) microscopy and low-temperature scanning electron microscopy. *Scanning.* **20**, 285–296 (1998).

[139] Mie, G. Beitrage zur optik truber medien, speziell kolloidaler metallosungen. *Ann. Phys* (1908).

[140] Drake, R. M. Mie scattering. *American Journal of Physics* **53**, 955 (1985).

[141] Arends, B., Kos, G. & Wobrock, W. Comparison of techniques for measurements of fog liquid water content. *Tellus B* (1992).

[142] Cotton, R. *et al.* The ability of the small ice detector (SID-2) to characterize cloud particle and aerosol morphologies obtained during flights of the FAAM BAe-146 research aircraft. *Journal of Atmospheric and Oceanic Technology* **27**, 290–303 (2010).

[143] Spiegel, J. K. *et al.* Evaluating the capabilities and uncertainties of droplet measurements for the fog droplet spectrometer (FM-100). *Atmospheric Measurement Techniques* **5**, 2237–2260 (2012).

[144] Bu, L., Yuan, J., Huang, X. & Chang, Y. A cloud droplet probe based on forward scattering. *Optik - International Journal for Light and Electron Optics* **124**, 5878–5881 (2013).

[145] Borrmann, S., Luo, B. & Mishchenko, M. Application of the T-matrix method to the measurement of aspherical (ellipsoidal) particles with forward scattering optical particle counters. *Journal of Aerosol Science* **31**, 789–799 (2000).

[146] Febvre, G., Gayet, J. F., Shcherbakov, V., Gourbeyre, C. & Jourdan, O. Some effects of ice crystals on the FSSP measurements in mixed phase clouds. *Atmospheric Chemistry and Physics* **12**, 8963–8977 (2012).

[147] McFarquhar, G. M. *et al.* Importance of small ice crystals to cirrus properties: Observations from the Tropical Warm Pool International Cloud Experiment (TWP-ICE). *Geophysical Research Letters* **34**, 1–6 (2007).

[148] Fugal, J. P. & Shaw, R. A. Cloud particle size distributions measured with an airborne digital in-line holographic instrument. *Atmospheric Measurement Techniques Discussions* **2**, 659–688 (2009).

[149] Gayet, J. F. *et al.* On the onset of the ice phase in boundary layer Arctic clouds. *Journal of Geophysical Research Atmospheres* **114**, 1–15 (2009).

[150] Pohl J. L. Van Genderen, C. & Pohl J. L. Van Genderen, C. Review article Multisensor image fusion in remote sensing: concepts, methods and applications. *International Journal of Remote Sensing* **19**, 823–854 (1998).

[151] Kim, M. K. Principles and techniques of digital holographic microscopy. *SPIE Reviews* **1**, 018005 (2010).

[152] Fugal, J. P. & Shaw, R. A. Ice Crystal Number Densities and Size Distributions from HOLODEC 3 . Preliminary Comparisons to Standard Probes 1–4 (2002).

[153] Uhlig, E. M., Borrmann, S. & Jaenicke, R. Holographic in-situ measurements of the spatial droplet distribution in stratiform clouds. *Tellus, Series B: Chemical and Physical Meteorology* **50B**, 377–387 (1998).

[154] Sansoni, G., Trebeschi, M. & Docchio, F. State-of-the-art and applications of 3D imaging sensors in industry, cultural heritage, medicine, and criminal investigation. *Sensors* **9**, 568–601 (2009).

[155] Himpel, M., Buttenschn, B. & Melzer, A. Three-view stereoscopy in dusty plasmas under microgravity: A calibration and reconstruction approach. *Review of Scientific Instruments* **82** (2011).

[156] Himpel, M., Killer, C., Buttenschön, B. & Melzer, A. Three-dimensional single particle tracking in dense dust clouds by stereoscopy of fluorescent particles. *Physics of Plasmas* **19** (2012).

[157] Davis, C. J. *et al.* Stereoscopic imaging of an Earth-impacting solar coronal mass ejection: A major milestone for the STEREO mission. *Geophysical Research Letters* **36**, 1–5 (2009).

[158] Ersoy, O. Surface area and volume measurements of volcanic ash particles by SEM stereoscopic imaging. *Journal of Volcanology and Geothermal Research* **190**, 290–296 (2010).

[159] Oktem, R., Lee, J., Thomas, A., Zuidema, P. & Romps, D. M. Stereo Photogrammetry of Oceanic Clouds. *Journal of Atmospheric and Oceanic Technology* 140507124240009 (2014).

[160] Seiz, G., Baltsavias, E. & Gruen, A. A. Cloud mapping from the ground: Use of photogrammetric methods. *Photogrammetric engineering and remote sensing* **68**, 941–951 (2002).

[161] Abdelmonem, A. *et al.* First correlated measurements of the shape and light scattering properties of cloud particles using the new Particle Habit Imaging and Polar Scattering (PHIPS) probe. *Atmospheric Measurement Techniques* **4**, 2125–2142 (2011).

[162] Lawson, R. P. *et al.* The 2D-S (stereo) probe: Design and preliminary tests of a new airborne, high-speed, high-resolution particle imaging probe. *Journal of Atmospheric and Oceanic Technology* **23**, 1462–1477 (2006).

[163] Das, S. & Ahuja, N. Performance analysis of stereo, vergence, and focus as depth cues for active vision. *IEEE Transactions on Pattern Analysis and Machine Intelligence* **17**, 1213–1219 (1995).

[164] Pouchou, J. L. *et al.* 3D reconstruction of rough surfaces by SEM stereo imaging. *Mikrochim. Acta* **139**, 139–144 (2002).

[165] Höhle, J. & Höhle, M. Accuracy assessment of digital elevation models by means of robust statistical methods. *ISPRS Journal of Photogrammetry and Remote Sensing* **64**, 398–406 (2009).

[166] Bühler, Y. *et al.* Spatially continuous mapping of snow depth in high alpine catchments using digital photogrammetry. *The Cryosphere Discussions* **8**, 3297–3333 (2014).

[167] Blostein, S. D. & Huang, T. S. Error analysis in stereo determination of 3-d point positions. *IEEE transactions on pattern analysis and machine intelligence* **9**, 752–765 (1987).

[168] Bradley, D., Atcheson, B., Ihrke, I. & Heidrich, W. Synchronization and rolling shutter compensation for consumer video camera arrays. *2009 IEEE Conference on Computer Vision and Pattern Recognition, CVPR 2009* 1–8 (2009).

[169] Gabor, D. Microscopy by reconstructed wave-fronts. *Proceedings of the Royal Society of London. Series A, Mathematical and Physical Sciences* **197**, 454–487 (1949).

[170] Bragg, W. L. The X-Ray Microscope. *Nature* **149**, 470–471 (1942).

[171] Khaleghi, M., Furlong, C., Ravicz, M., Cheng, J. T. & Rosowski, J. J. Three-dimensional vibrometry of the human eardrum with stroboscopic lensless digital holography. *Journal of Biomedical Optics* **20**, 051028 (2015).

[172] Kjeldsen, H. D., Kaiser, M. & Whittington, M. A. Near-field electromagnetic holography for high-resolution analysis of network interactions in neuronal tissue. *Journal of Neuroscience Methods* **253**, 1–9 (2015).

[173] Curtis, J. E., Koss, B. A. & Grier, D. G. Dynamic holographic optical tweezers. *Optics Communications* **207**, 169–175 (2002).

[174] Fujita, J. *et al.* Manipulation of an atomic beam by a computer-generated hologram. *Nature* **380**, 691–694 (1996).

[175] Hasegawa, S. & Hayasaki, Y. Holographic femtosecond laser processing with multiplexed phase fresnel lenses displayed on a liquid crystal spatial light modulator. *Optical Review* **14**, 208–213 (2007).

[176] Lee, S.-H. & Grier, D. G. Holographic microscopy of holographically trapped three-dimensional structures. *Optics express* **15**, 1505–1512 (2007).

[177] Zhang, Y. *et al.* Application of short-coherence lensless Fourier-transform digital holography in imaging through diffusive medium. *Optics Communications* **286**, 56–59 (2013).

[178] Lindsey, C. & Braun, D. C. Principles of Seismic Holography for Diagnostics of the Shallow Subphotosphere. *The Astrophysical Journal Supplement Series* **155**, 209–225 (2004).

[179] Wardosanidze, Z. V., Chanishvili, A., Petriashvili, G. & Chilaya, G. Cholesteric liquid crystal holographic laser. *Optics letters* **39**, 1008–10 (2014).

[180] Hinsch, K. D. & Herrmann, S. F. Holographic particle image velocimetry. *Measurement Science & Technology* **15** (2004).

[181] Walker, M. A., Koopmans, L. V. E., Stinebring, D. R. & Van Straten, W. Interstellar holography. *Monthly Notices of the Royal Astronomical Society* **388**, 1214–1222 (2008).

[182] Leith, E. N. & Upatnieks, J. Wavefront Reconstruction with Diffused Illumination and Three Dimensional Objects. *Journal of the Optical Society of America* **54**, 1295–1301 (1964).

[183] Rogers, G. L. Gabor diffraction microscopy: the hologram as a generalized zone-plate. *Nature* **166**, 237 (1950).

[184] Locatelli, M. *et al.* Imaging live humans through smoke and flames using far-infrared digital holography. *Optics express* **21**, 5379–90 (2013).

[185] Xue, K., Li, Q., Li, Y.-D. & Wang, Q. Continuous-wave terahertz in-line digital holography. *Optics Letters* **37**, 3228 (2012).

[186] Wachulak, P. W. *et al.* Sub 400 nm spatial resolution extreme ultraviolet holography with a table top laser. *Optics express* **14**, 9636–9642 (2006).

[187] Bartels, M., Krenkel, M., Haber, J., Wilke, R. N. & Salditt, T. X-Ray Holographic Imaging of Hydrated Biological Cells in Solution. *Physical Review letters* **114**, 1–5 (2015).

[188] Korecki, P., Materlik, G. & Korecki, J. Complex γ-ray hologram: Solution to twin images problem in atomic resolution imaging. *Physical Review Letters* **86**, 1534–1537 (2001).

[189] D'Alfonso, A. J. *et al.* Generalized Fourier Holography Meets Coherent Diffractive Imaging. *Microscopy Today* **23**, 28–33 (2015).

[190] Wachulak, P. & Marconi, M. Holographic imaging with nanometer resolution using compact table-top EUV laser. *Opto-Electronics Review* **18**, 121–136 (2010).

[191] Leith, E. N. & Upatnieks, J. Reconstructed Wavefronts and Communication Theory. *Journal of the Optical Society of America* **52**, 1123 (1962).

[192] Kreuzer, H. J., Nakamura, K., Wierzbicki, a., Fink, H. W. & Schmid, H. Theory of the point source electron microscope. *Ultramicroscopy* **45**, 381–403 (1992).

[193] Leith, E. N. & Upatnieks, J. Microscopy by Wavefront Reconstruction. *Journal of the Optical Society of America* **55**, 569_1 (1965).

[194] Thompson, B. J., Ward, J. H. & Zinky, W. R. Application of hologram techniques for particle size analysis. *Applied optics* **6**, 519–526 (1967).

[195] Brown, P. R. A. Use of Holography for Airborne Cloud Physics Measurements. *Journal of Atmospheric and Oceanic Technology* **6**, 293–306 (1989).

[196] Thompson, B. J. Holographic Methods for Particle Size and Velocity Measurement - Recent Advances. *Holographic Optics II: Principles and Applications* **1136**, 308–326 (1989).

[197] Vössing, H. J., Borrmann, S. & Jaenicke, R. In-line holography of cloud volumes applied to the measurement of raindrops and snowflakes. *Atmospheric Research* **49**, 199–212 (1998).

[198] Raupach, S. M. F., Vössing, H. J., Curtius, J. & Borrmann, S. Imaging of Atmospheric Ice Particles. *Journal of Optics A: Pure and Applied Optics* **8**, 796–806 (2006).

[199] Amsler, P. *et al.* Ice crystal habits from cloud chamber studies obtained by in-line holographic microscopy related to depolarization measurements. *Applied optics* **48**, 5811–5822 (2009).

[200] Lawson, R., Lawson, R., Cormack, R. & Cormack, R. Theoretical design and preliminary tests of two new particle spectrometers for cloud microphysics research. *Atmospheric Research* **35**, 315–348 (1995).

[201] Schnars, U. & Jueptner, W. *Digital Holography* (Springer-Verlag, Berlin, 2005).

[202] Benton, S. A. & Bove, V. M. *Holographic Imaging* (John Wiley & Sons, New Jersey, 2008).

[203] Goodman, J. W. *Introduction to Fourier Optics* (McGraw-Hill, New York, 1996).

[204] Colomb, T. *et al.* Numerical parametric lens for shifting, magnification, and complete aberration compensation in digital holographic microscopy. *Journal of the Optical Society of America A* **23**, 3177–90 (2006).

[205] Latychevskaia, T. & Fink, H. W. Solution to the twin image problem in holography. *Physical Review Letters* **98**, 1–4 (2007).

[206] Raupach, S. M. F. Cascaded adaptive-mask algorithm for twin-image removal and its application to digital holograms of ice crystals. *Appl. Opt.* **48**, 287–301 (2009).

[207] Shen, F. & Wang, A. Fast-Fourier-transform based numerical integration method for the Rayleigh-Sommerfeld diffraction formula. *Applied optics* **45**, 1102–1110 (2006).

[208] Molony, K. M., Hennelly, B. M., Kelly, D. P. & Naughton, T. J. Reconstruction algorithms applied to in-line Gabor digital holographic microscopy. *Optics Communications* **283**, 903–909 (2010).

[209] Ghan, S. J., Leung, L. R. & Easter, R. C. Prediction of cloud droplet number in a general circulation model. *Journal of Geophysical Research* **102**, 777–794 (1997).

[210] Leaitch, W. R., Isaac, G. A., Strapp, J. W., Banic, C. M. & Wiebe, H. A. The relationship between cloud droplet number concentrations and anthropogenic pollution: observations and climatic implications. *Journal of Geophysical Research* **97**, 2463–2474 (1992).

[211] Li, J.-C. & Picart, P. *Digital Holography* (ISTE Ltd, London, 2012).

[212] Fournier, C., Ducottet, C. & Fournel, T. Digital in-line holography: influence of the reconstruction function on the axial profile of a reconstructed particle image. *Measurement Science and Technology* **15**, 686–693 (2004).

[213] Collier, R. J., Burkhardt, C. B. & Lin, L. H. *Optical Holography* (Academic Press, New York, 1971).

[214] Pan, G. & Meng, H. Digital holography of particle fields: reconstruction by use of complex amplitude. *Applied optics* **42**, 827–833 (2003).

[215] Ozgen, M. T. Analysis of in-line Fresnel holograms via chirp separation. *Optical Engineering* **45**, 035801 (2006).

[216] Widjaja, J. & Chuamchaitrakool, P. Holographic particle tracking using Wigner-Ville distribution. *Optics and Lasers in Engineering* **51**, 311–316 (2013).

[217] Yang, W., Kostinski, A. B. & Shaw, R. A. Depth-of-focus reduction for digital in-line holography of particle field. *Optics Letters* **30**, 1303–1305 (2005).

[218] Liebling, M., Blu, T. & Unser, M. Fresnelets: New multiresolution wavelet bases for digital holography. *IEEE Transactions on Image Processing* **12**, 29–43 (2003).

[219] Atherton, T. J. & Kerbyson, D. J. Size invariant circle detection. *Image and Vision Computing* **17**, 795–803 (1999).

[220] Tan, S., Zhang, F., Huang, Q. & Wang, S. Measuring and Calculating geometrical parameters of marine plankton using digital laser holographic imaging. *Optik - International Journal for Light and Electron Optics* **125**, 5119–5123 (2014).

[221] Nishihara, K. New method of obtaining particle diameter by the fast Fourier transform pattern of the in-line hologram. *Optical Engineering* **36**, 2429 (1997).

[222] Meyer, F. & Beucher, S. Morphological segmentation. *Journal of Visual Communication and Image Representation* **1**, 21–46 (1990).

[223] Rodriguez, A., Ehlenberger, D. B., Dickstein, D. L., Hof, P. R. & Wearne, S. L. Automated three-dimensional detection and shape classification of dendritic spines from fluorescence microscopy images. *PLoS ONE* **3** (2008).

[224] Zhu, Y., Carragher, B., Mouche, F. & Potter, C. S. Automatic Particle Detection through Efficient Hough Transforms. *IEEE Transactions on Medical Imaging* **22**, 1053–1062 (2003).

[225] Fugal, J. P., Schulz, T. J. & Shaw, R. A. Practical methods for automated reconstruction and characterization of particles in digital in-line holograms. *Measurement Science and Technology* **20**, 075501 (2009).

[226] Otsu, N. A Threshold Selection Method from Gray-Level Histograms. *IEEE Transactions on Systems, Man and Cybernetics* **20**, 62–66 (1979).

[227] Sheng, J., Malkiel, E. & Katz, J. Digital holographic microscope for measuring three-dimensional particle distributions and motions. *Applied optics* **45**, 3893–3901 (2006).

[228] Cartwright, S., Dunn, P. & Thompson, B. Particle sizing using far -field holography: new developments. *Optical Engineering* **19**, 727–733 (1980).

[229] Jericho, S. K., Garcia-Sucerquia, J., Xu, W., Jericho, M. H. & Kreuzer, H. J. Submersible digital in-line holographic microscope. *Review of Scientific Instruments* **77** (2006).

[230] Garcia-sucerquia, J. *et al.* Digital in-line holographic microscopy. *Applied Optics* **45**, 836–850 (2006).

[231] Jacquot, M., Sandoz, P. & Tribillon, G. High resolution digital holography. *Optics Communications* **190**, 87–94 (2001).

[232] Saleh, B. E. A. & Teich, M. C. *Fundamentals of Photonics* (John Wiley & Sons, New York, 1991).

Appendix A

3D Image Reconstruction Software

```
close all
clear all
%%%%%%%%%%Read In and Processing Stage%%%%%%%%%%
RpathRPI = '/path/to/reference_image';
IpathRPI = '/path/to/hologram';
%Camera Laser spacing
%Example spacing:
ZL = 5.7;
%Spacing from camera to microscope slide to determine start point of
%sampling volume
Zoffset = 1.9;
%Construct distances to reconstruct over:
%Object 1 Recon:
Zmin = 35e-2;
Zmax = 45e-2;
DNz = 40;
Z = 1*linspace(Zmin,Zmax,DNz);
%Switches:
%If true, use original camaera sampling rate for reconstruction
samp = true;
%If true, subtract reference wave background image.
refsub = false;
%If true, do fourier filtering to remove fringe noise
dofilt = false;
%If true, read in RPI cam image format, else use see3cam file.
RPIcam = false;
%switch to do phase analysis or not:
dophase = false;
```

```
%switch to choose reconstruct method:
%True for AS_conv, false for fresnel
convrec = true;
%Output gif filename:
fini = IpathSee3(84:98);
if(dofilt)
  fini = horzcat(fini,'_filt');
else
    fini = horzcat(fini,'_nofilt');
end
if(refsub)
    fini = horzcat(fini,'_refsub');
end
fini = horzcat(fini,'_Z_');
Zfocus = Zmin/1e-2;
%Magnification corrected min depth:
ZminT = ((1/Zfocus)+(1/ZL))^(-1);
Zfocus = Zmax/1e-2;
%Magnification corrected max depth:
ZmaxT = ((1/Zfocus)+(1/ZL))^(-1);
%If want output image labels to have origin of depth at start of sampling
%volume set true
offsetsub = true;
if offsetsub == true;
        ZmaxT = ZmaxT - Zoffset;
        ZminT = ZminT - Zoffset;
filename = horzcat(fini,num2str(ZminT),'cm_',num2str(ZmaxT),'cm.gif');
else
    filename = horzcat(fini,num2str(ZminT),'cm_',num2str(ZmaxT),'cm.gif');
end
%switch to save gif or not. Saves if true.
savegif = false;
%If only want images, set to true. if want axis etc, set to false.
gifsimple = false;
%Set true if want output images with grayscale colourbar
graygif = true;
%If want scale on output image set true
scaleon = true;
%Experimental Parameters:
%Laser wavelength:
L = 827.5e-9;
L = 403e-9;
if RPIcam==true
    %Create camera grid:
```

```
    %Pixel Size:
Pix = 1.4e-6;
%Number of pixels in array:
Nx = 2612;
Ny = 1944;
%If using padding:
if samp==false
 Nx = 4096;
 Ny = 4096;
end
X = Nx*Pix;
Y = Ny*Pix;
X2 = linspace(-X/2,X/2,Nx);
Y2 = linspace(-Y/2,Y/2,Ny);
[x2,y2] = meshgrid(X2,Y2);
%Get RAW Images:
Ipath = IpathRPI;
Rpath = RpathRPI;
fpath = {
Ipath;
Rpath;
};
fileID1=fopen(Ipath);
fileID2=fopen(Rpath);
files = [fileID1,fileID2];
%Make title names:
titles = {'Hologram','Reference'};
%Number of Images
Nim = 2;
%Store Raw images
Raw = zeros(2612,1944,Nim);
%Store Original images
Jpeg = zeros(2592,1944,3,Nim);
for ii = 1:Nim;
%Read the data bytes into a single column array
fid = files(ii);
%A=fread(fileID);
A=fread(fid);
%Save the jpeg images for comparison:
J = imread(fpath{ii});
J = imrotate(J,270);
J = flipdim(J,2);
Jpeg(:,:,:,ii) = J;
%Get total number of bytes
```

```
N=length(A);
%Only store raw image information
N1=N-6345217;
A1=A(N1+2:N);
%Reshape the single column into an image matrix
B=reshape(A1,3264,1944);
%Removes every 5th byte as this is not a true sensor pixel byte
removeList = 5:5:3264;
B(removeList,:) = [];
%Store Raw image
Raw(:,:,ii) = B;
end
I = Raw(:,:,1)';
%Save hologram
Ites = I;
R = Raw(:,:,2)';
else
    %Create camera grid:
Pix = 2.2e-6;
Nx = 2592;
width = Nx;
Ny = 1944;
height= Ny;
%If using padding:
if samp==false
 Nx = 4096;
 Ny = 4096;
end
X = Nx*Pix;
Y = Ny*Pix;
X2 = linspace(-X/2,X/2,Nx);
Y2 = linspace(-Y/2,Y/2,Ny);
[x2,y2] = meshgrid(X2,Y2);
fid = fopen(IpathSee3);
A = fread(fid);
n = length(A);
B = zeros(1,n/2);
B = B';
for pii = 1:n/2;
    a = A(2*pii-1);
    b = A(2*pii);
    whole = a + 256*b;
    B(pii) = whole;
end
```

```
I = reshape(B,width,height);
I = I';
fid = fopen(RpathSee3);
A = fread(fid);
n = length(A);
B = zeros(1,n/2);
B = B';
for pii = 1:n/2;
    a = A(2*pii-1);
    b = A(2*pii);
    whole = a + 256*b;
    B(pii) = whole;
end
R = reshape(B,width,height);
  R=R';
end
%Investigate reference wave intensity:
%%%....Plotting routines omitted here for brevity....%%%
if dofilt == true
    output = I;
%FFt filtering:
%Amplitude + Phase:
Aa = output;
Bb=fftshift(fft2(Aa));
[a,b] =size(Aa);
Filt = zeros(a,b);
%For removing sections
Filt = ones(a,b);
%Inner offaxis central features
Filt(1290:1305,965:970)=0;
Filt(1290:1305,976:982)=0;
% Create a logical image of a circle with specified
% diameter, center, and image size.
% First create the image.
imageSizeX = height;
imageSizeY = width;
[columnsInImage rowsInImage] = meshgrid(1:imageSizeX, 1:imageSizeY);
% Next create the circle in the image.
centerX1 = 932;
centerY1 = 1235;
radius1 = 10;
centerX2 = 1012;
centerY2 = 1358;
radius2 = 10;
```

```
centerX3 = 970;
centerY3 = 1297;
radius3 = 2;
centerX4 = 976;
centerY4 = 1297;
radius4 = 2;
centerX5 = 956;
centerY5 = 1297;
radius5 = 4;
centerX6 = 990;
centerY6 = 1297;
radius6 = 4;
centerX7 = 916;
centerY7 = 1238;
radius7 = 4;
centerX8 = 1031;
centerY8 = 1357;
radius8 = 4;
centerX9 = 973;
centerY9 = 1297;
radius9 = 1;
circ = (rowsInImage - centerY1).^2 ...
    + (columnsInImage - centerX1).^2 >= radius1.^2 &(rowsInImage - centerY2).^2 ...
    + (columnsInImage - centerX2).^2 >= radius2.^2 &(rowsInImage - centerY3).^2 ...
    + (columnsInImage - centerX3).^2 >= radius3.^2 &(rowsInImage - centerY4).^2 ...
    + (columnsInImage - centerX4).^2 >= radius4.^2 &(rowsInImage - centerY5).^2 ...
    + (columnsInImage - centerX5).^2 >= radius5.^2 &(rowsInImage - centerY6).^2 ...
    + (columnsInImage - centerX6).^2 >= radius6.^2 &(rowsInImage - centerY7).^2 ...
    + (columnsInImage - centerX7).^2 >= radius7.^2 &(rowsInImage - centerY8).^2 ...
    + (columnsInImage - centerX8).^2 >= radius8.^2 ;%&(rowsInImage - centerY9).^2 ...
    %+ (columnsInImage - centerX9).^2 >= radius9.^2;
circ = circ';
% circ is a 2D "logical" array.
% Now, display it.
%%%....Plotting routines omitted here for brevity....%%%
Cc = circ.*Bb;
Dd = ifft2(fftshift(Cc));
I = abs(Dd);
end
if(refsub)
I = I - R;
end
%Try fourier filtering to improve image quality:
Eff = fft2(I);
```

```
%%%....Plotting routines omitted here for brevity....%%%
Ipp = ((Eff));
Iff = fftshift(Ipp);
[a,b] =size(I);

%%%%%%%%%%Reconstruction Stage%%%%%%%%%%
%%%Loop to construct at multiple distances from sensor%%%
Eoutcomplex = zeros(Ny,Nx,length(Z));
Eout = zeros(Ny,Nx,length(Z));
%Store axis values for each Z plane
A_x = ones(length(X2),length(Z));
A_y = ones(length(Y2),length(Z));
%Construct axis vectors for fixed display size:
A_xF = cell(1,length(Z));
A_yF = cell(1,length(Z));
%Reconstruct with convolution method or Fresnel approx:
%Convolution method:
if convrec == true
for jj = 1 : length(Z);
%Vary z2 here to reconstruct at different distances (hopefully)
z2 = Z(jj);
%Reference wave phase at hologram plane:
Zla = 6.8e-2;
Zphase = Zla + z2;
%Use spherical wave phase:
PR2 = (2*pi/L)*((1/2*Zphase)*(x2.^2 + y2.^2));
PR2 = 0;
%Assume constant intensity plane wave
Ir = max(max(R));
AR2 = sqrt(Ir);
AR2 = mean2(R);
%Or using spherical wave amplitude:
R2 = AR2.*exp(-i*PR2);
%If no reference used:
% R2=1;
%normalise reference and hologram before taking product:
% R2=(R2-min(R2(:)))/(max(R2(:))-min(R2(:)));
% I=(I-min(I(:)))/(max(I(:))-min(I(:)));
%Take product of reference and hologram
E = R2.*I;
%If constructing with convolution method (short distances):
Uf=fft2(E);
Uf=fftshift(Uf); % Spectrum of the initial field
fex=Nx/X;fey=Ny/Y;% sampling of frequency plane
```

```
fx=[-fex/2:fex/Nx:fex/2-fex/Nx];
fy=[-fey/2:fey/Ny:fey/2-fey/Ny];
[FX,FY]=meshgrid(fx,fy);
k=2*pi/L;
G=exp(i*k*z2*sqrt(1-(L*FX).^2-(L*FY).^2)); % Angular spectrum transfer function % Diffra
result=Uf.*G;
Uf=ifft2(result);
If=abs(Uf);
Eout(:,:,jj) = Uf;
convgif = true;
end
%Fresnel method:
else
for jj = 1 : length(Z);
%Vary z2 here to reconstruct at different distances (hopefully)
z2 = Z(jj);
%Reference wave phase at hologram plane:
Zphase = z2;
%Use spherical wave phase:
PR2 = (2*pi/L)*((1/2*Zphase)*(x2.^2 + y2.^2));
%Assume constant intensity plane wave
Ir = max(max(R));
AR2 = sqrt(Ir);
AR2 = mean2(R);
%Or using spherical wave amplitude:
R2 = AR2.*exp(-i*PR2);
%If no reference used:
R2=1;
% R2 = AR2;
%normalise reference and hologram before taking product:
% R2=(R2-min(R2(:)))/(max(R2(:))-min(R2(:)));
% I=(I-min(I(:)))/(max(I(:))-min(I(:)));
%Take product of reference and hologram
E = R2.*I;
%If constructing with Fresnel approximation (large distances):
%Include Fresnel factor:
fac = exp((-i*pi/(L*z2))*(x2.^2 + y2.^2));
E = E.*fac;
E2 = E;
%Calculate reconstructed image
E = ifft2(E);
E = fftshift(E);
%Normalisation factor:
Norm = i/(L*z2);
```

```
E = Norm*E;
% %Add in phase factors:
% Pfac1 = exp(-i*2*pi*z2/L);
% Pfac2 = exp(-i*pi*L*z2*((x2/Nx*Pix).^2 + (y2/Ny*Pix).^2));
% E = E.*Pfac1.*Pfac2;
%Save complex wavefronts into a variable:
Eoutcomplex(:,:,jj) = E;
%Save intensities:
E = abs(E);
If = abs(E);
Eout(:,:,jj) = E;
%Scale reconstruction axis to correct values
Ffx = (L*Z(jj))/(Nx*(Pix^2));
A_x(:,jj) = Ffx*linspace(-X/2,X/2,Nx);
Ffy = (L*Z(jj))/(Ny*(Pix^2));
A_y(:,jj) = Ffy*linspace(-Y/2,Y/2,Ny);
Nxx = round(Nx/Ffx);
Nyy = round(Ny/Ffy);
A_xF{jj} = linspace(-X/2,X/2,Nxx);
A_yF{jj} = linspace(-Y/2,Y/2,Nyy);
convgif = false;
end
for ii =1:length(Z);
    xT = length(A_xF{ii});
    yT = length(A_yF{ii});
    Ai = Eout(round(Ny/2-yT/2+1):round(Ny/2+yT/2),round(Nx/2-xT/2+1):round(Nx/2+xT/2)
    Ai = im2double(Ai);
    Ai = imresize(Ai,[Ny,Nx]);
%Rescale back to 256 bit dataset:
% minValueS = min(min(Ai));
% maxValueS = max(max(Ai));
% rangeS = maxValueS - minValueS;
% Ai = (Ai - minValueS) / rangeS;
% Ai = Ai*256;
Esame(:,:,ii) = Ai;
end
end
[Mz,Iz] = max(abs(Eout),[],3);
%%%....Plotting routines omitted here for brevity....%%%

%%%%%%%%%%%Phase Analysis%%%%%%%%%%%
if(dophase);
%Get heightmaps from phase:
%Since phase = k.z = (2pi/lambda)*z, z = phase*lambda/2pi for variation
```

```
%between 0 and 2pi. for -pi to pi then get factor of half, hence:
%Investigate phase in plane where image in focus:
%Example
hmap = (L/(2*pi)*angle(Eout(:,:,30)));
%Mod 2pi phase ambiguity means cannot resolve features deeper than lambda/2
%without phase unwrapping or PSDH. eg. for L = 830nm, depthmax = 415nm

%%%....Plotting routines omitted here for brevity....%%%

%Load in reference spectrum
load('/path/to/gradphase.mat');
%Define view window:
xi = 1;
xf = 1775;
yi = 1;
yf = 2500;
%Define cut position:
ysliy = 1275;
Npha = 1;
phase_av = 1e9*((hmap(:,ysliy)-refphase(:,ysliy))/1);
%Or just subtract whole images from each other
for pii = 1:Npha;
phase_av = phase_av + 1e9*((hmap(:,ysliy+pii)- refphase(:,ysliy+pii))/1);
end
phase_av = phase_av/(Npha+1);
%%%....Plotting routines omitted here for brevity....%%%
end
%%%%%%%%%%Output Stage%%%%%%%%%%
%If want a gif saved:
if savegif == true
% Save results as .gif movies:
   figure('units','normalized','outerposition',[0 0 1 1])
if convgif == true
for ii = 1:DNz;
clf('reset')
xT = length(A_xF{ii});
yT = length(A_yF{ii});
%Or with Convolution approach:
%Phase image:
%Height map from phase image:
hmapplot = (L/(2*pi))*angle(Eout(:,:,ii));
Zfocus = Z(ii)/1e-2;
ZT = ((1/Zfocus)+(1/ZL))^(-1);
if offsetsub == true
```

```
425 T = horzcat('Z=', num2str(ZT-Zoffset),' cm');
426 else
427     T = horzcat('Z=', num2str(ZT),' cm');
428 end
429 Npix = 10;
430 Zobj = ZT;
431 Mag = -1/((Zobj/ZL)-1);
432 Dparticle = Npix*Pix*1e6/Mag;
433 Xmag = 1e6*X2/Mag;
434 Ymag = 1e6*Y2/Mag;
435 if gifsimple == true
436 figure;
437 % remove decorations
438      set(gcf,'toolbar','none');
439      set(gcf,'menubar','none');
440      set(gcf,'numbertitle','off');
441 % ...the axis
442      set(gca,'position',[0 0 1 1]);
443 % ...the image
444      h = imagesc(abs(Eout(:,:,ii)));
445          if graygif == true
446         colormap('Gray')
447          else
448          end
449 % ...at full size
450      set(gcf,'position',...
451          get(0,'screensize'));
452  set(gca,'xtick',[])
453  set(gca,'ytick',[])
454 else
455     if scaleon == true
456     ImE = abs(Eout(:,:,ii));
457     h = imagesc(Xmag,Ymag,ImE);
458     hold on
459     daspect([1 1 1])
460     scalebar('Bold',true,'Colour',[1 0 0])
461     else
462             ImE = abs(Eout(:,:,ii));
463     h = imagesc(Xmag,Ymag,ImE);
464     end
465     if graygif == true
466         colormap('Gray')
467     else
468     end
```

```
469 title(T)
470 xlabel('X axis (Microns)')
471 ylabel('Y axis (Microns)')
472 colorbar
473 end
474 drawnow
475 frame = getframe(gcf);
476 im = frame2im(frame);
477 [imind,cm] = rgb2ind(im,256);
478 if ii == 1;
479     imwrite(imind,cm,filename,'gif', 'Loopcount',inf);
480 else
481     imwrite(imind,cm,filename,'gif','WriteMode','append');
482 end
483 end
484 else
485     for ii = 1:DNz;
486 clf('reset')
487 xT = length(A_xF{ii});
488 yT = length(A_yF{ii});
489 h = imagesc(A_xF{ii},A_yF{ii},Eout(round(Ny/2-yT/2+1):round(Ny/2+yT/2),round(Nx/2-xT/2+1
490 Zfocus = Z(ii)/1e-2;
491 ZT = ((1/Zfocus)+(1/ZL))^(-1);
492 T = horzcat('Z=', num2str(ZT),' cm');
493 if gifsimple == true
494     axis off
495 else
496 title(T)
497 xlabel('X axis (pixels)')
498 ylabel('Y axis (pixels)')
499 colorbar
500 end
501     if graygif == true
502         colormap('Gray')
503     else
504     end
505 drawnow
506 frame = getframe(gcf);
507 frame = getframe(gca);
508 im = frame2im(frame);
509 [imind,cm] = rgb2ind(im,256);
510 if ii == 1;
511     imwrite(imind,cm,filename,'gif', 'Loopcount',inf);
512 else
```

```
513     imwrite(imind,cm,filename,'gif','WriteMode','append');
514 end
515     end
516 end
517 else
518 end
519 %%%%%%%%%%Useful Equations%%%%%%%%%%
520 %Critical point for Z
521 Zcritx = Pix^2*Nx/L;
522 Zcrity = Pix^2*Ny/L;
523 %NA for holography ( ie. of a CCD) given by:
524 %(Depends on z so use ztest value)
525 ztest = 1e-2*[0.5,1,2,3,4,5,6,7,8,9];
526 NAx = 0.5*X./sqrt((X/2).^2 + ztest.^2);
527 NAy = 0.5*Y./sqrt((Y/2).^2 + ztest.^2);
528 %To resolve particles need to have them seperated by at least:
529 Ltest = 405e-9;
530 Ltest = 830e-9;
531 rsep = Ltest./(2*NAx)
532 figure()
533 plot(100*ztest,NAx)
534 xlabel('Depth (cm)')
535 ylabel('NAx')
536 figure()
537 plot(100*ztest,1e6*rsep)
538 xlabel('depth (cm)')
539 ylabel('Minimum Resolvable Seperation (microns)')
540 %Calculate actual object position from focus image location (see Benton):
541 % ztrue = ((1/zfocus)+(1/zlaser))^(-1);
542 %Eg:
543 ztrue = ((1/12.9)+(1/12.5))^(-1);
544 %Lateral magnification:
545 %Mlat = Zimage/Zobj = zfocus/ztrue;
546 %Eg:
547 Mlat = 12.9/6.35;
548 %Convert depth from input to physical depth
549 ZL = 5.7;
550 Zobject = 45e-2;
551 Zfocus = Zobject/1e-2;
552 %Example
553 ZmaxT = ((1/Zfocus)+(1/ZL))^(-1)
554 %%For saving 3D array into a gif:
555 %ki = abs(Eout);
556 %save_3D_matrix_as_gif('/Users/tomchambers/Desktop/testgray.gif',ki)
```

Appendix B

Refereed Conference Paper

A low cost digital holographic imager for calibration and validation of cloud microphysics remote sensing

Thomas E. Chambers[a], Murray W. Hamilton[a], and Iain M. Reid[a]

[a]The University of Adelaide, Adelaide 5005, South Australia , Australia

ABSTRACT

Clouds cover approximately 70% of the Earth's surface and therefore play a crucial role in governing both the climate system and the hydrological cycle. The microphysical properties of clouds such as the cloud particle size distribution, shape distribution and spatial homogeneity contribute significantly to the net radiative effect of clouds and these properties must therefore be measured and understood to determine the exact contribution of clouds to the climate system. Significant discrepancies are observed between meteorological models and observations, particularly in polar regions that are most sensitive to changes in climate, suggesting a lack of understanding of these complex microphysical processes. Remote sensing techniques such as polarimetric LIDAR and radar allow microphysical cloud measurements with high temporal and spatial resolution however these instruments must be calibrated and validated by direct in situ measurements. To this end a low-cost, light-weight holographic imaging device has been developed and experimentally tested that is suitable for deployment on a weather balloon or tower structure to significantly increase the availability of in situ microphysics retrievals.

Keywords: cloud microphysics, digital holography, in situ, remote sensing, validation

1. INTRODUCTION

Clouds have been identified as being one of the largest sources of uncertainty in the predictions of global climate models and weather forecasting operations.[1,2] This large uncertainty can be attributed to the complicated formation, dynamics and evolution of clouds[3,4] dependent on their microphysical observables such as the particle size distribution, thermodynamic phase, particle shape distribution, particle refractive index, surface roughness and spatial homogeneity. These properties can vary on scales ranging from nanometres up to kilometres[5] over characteristic timescales of minutes to days[6] and to date the accurate detection and characterisation of these processes has been elusive. Remote sensing techniques such as polarimetric LIDAR and radar have been used with considerable success[7,8] to extract some of these observables at high spatial and temporal resolutions however there are underlying uncertainties in the retrieval process of these microphysical observables in current implementations[9] particularly in retrievals from mixed phase clouds[10] and complicated vertical cloud structures.[11] Remote sensing of these microphysical properties is typically performed by comparison of return signals with bulk scattering models based on the single scattering properties of water droplets and ice crystals obtained from look up tables[12] guided by in situ observations[13,14] of the true observables such as particle size and shape distribution. Significant progress has been made in the development of these retrieval models, however there is still a need for accurate in situ observations to be made in both the calibration and validation of remote sensing techniques.[15,16]

In situ measurement of cloud microphysical properties has traditionally been performed via ground based observations and on board research aircraft.[17] Ground based measurements reveal limited information about the vertical distribution of cloud properties, and can only be undertaken at field sites that are sufficiently high so as to intersect with cloud formation heights. This limits the spatial resolution of these techniques and cannot be used for direct validation of satellite techniques in the case of complicated vertical cloud structures. Research aircraft observations allow the full profile of the cloud to be studied, however the cost of these flights and the corresponding design challenges of operating such instruments in a safe manner has severely restricted the temporal resolution of these studies. The large speeds associated with aircraft observations also raise the challenge of sampling biases due to shattering of ice crystals on the probes of instrument inlets.[18] There is therefore a need for a low cost, light weight device that can extract these microphysical observables

Further author information: (Send correspondence to A.A.A.)
A.A.A.: E-mail: thomas.chambers@adelaide.edu.au, Telephone: 61 411 170 536
B.B.A.: E-mail: murray.hamilton@adelaide.edu.au, Telephone: 831 33994

Remote Sensing of Clouds and the Atmosphere XXI, edited by Adolfo Comerón, Evgueni I. Kassianov, Klaus Schäfer, James W. Jack, Richard H. Picard, Konradin Weber, Proc. of SPIE Vol. 10001, 100010P · © 2016 SPIE · CCC code: 0277-786X/16/$18 · doi: 10.1117/12.2239590

in a robust manner that is suitable for both ground based deployment and vertical profiling via attachment to a standard weather balloon.[19] The potential for balloon deployment would significantly increase the availability of valuable in situ observations in regions where aircraft flights are considered too dangerous, and where terrain does not allow for a ground based in situ observation system.

Digital holography is a wavefront sensing technique that allows both the amplitude and the phase of a coherent optical wavefront to be sampled from a single image acquisition.[20] If this technique is applied to the light scattered from a field of objects, it allows a three dimensional image of the object field to be reconstructed. Digital holography has been successfully used in a range of applications including the in situ sampling of cloud microphysical observables such as particle shape, size and spatial distribution.[21–23] The key challenge in the present day implementation of these instruments is the significant cost associated with obtaining data in a robust and reliable fashion in a range of atmospheric conditions. This has led to these instruments being relatively expensive and heavy, precluding their use in potentially expendable deployment methods such as attachment to a weather balloon, and wide spread deployment via mass production. For this reason a low-cost, light-weight digital holographic imager has been developed and experimentally tested and the results of this process will be outlined in this work.

2. INSTRUMENT OVERVIEW AND DESIGN CONSIDERATIONS

A digital holographic imaging system consists of three major components; the optoelectronic detection hardware and control systems, the instrument enclosure and the image reconstruction and analysis software. These features have been optimised to minimise cost and weight whilst still providing a robust and reliable system.

2.1 Digital holography overview

Digital holographic imaging is a two stage technique in which a coherent light source is used to illuminate a set of objects to be imaged, and the resultant interference pattern between the scattered and unscattered background light is recorded on a CCD or CMOS sensor. This interference pattern is then treated as a numerical diffracting aperture and scalar diffraction theory is used to numerically reconstruct the original object wavefront at a range of depth positions, allowing a three dimensional image of the objects to be generated. This process can be carried out efficiently by use of the Fast Fourier Transform (FFT) algorithm allowing large sampling volumes to be reconstructed and analysed automatically with software such as that described in this work.

A holographic imaging system is relatively simple, requiring only a coherent light source such as a laser and a digital CCD or CMOS camera to sample the interference pattern. Due to the relatively coarse resolution imposed by the pixel sizes of digital sensors, an inline geometry has been selected for this imager; with the laser, sampling volume and camera coaxial with each other as outlined in Figure 1. This produces the largest fringe spacing of any recording geometry. Furthermore this geometry does not require any lenses or complex optical components and hence the alignment issues, vibration sensitivity and cost of such a system are significantly reduced, as required for a potentially expendable system.

The divergent spherical wavefront produced by the 405nm wavelength laser diode allows geometric magnification of the interference pattern, improving the resolution of this system. This magnification allows a theoretical resolution on the order of the laser wavelength[24] however due to the divergent nature of the beam, the sampling volume is significantly reduced. For this reason the system has been designed to be as modular as possible allowing this magnification to be quickly varied, as well as allowing the use of an additional lens system for collimation of the beam to increase the sampling volume at the cost of resolution, depending on the application of interest.

2.2 Instrument design considerations

The robust operation of a low cost holographic imager in the diverse range of conditions encountered within a cloud guided the design of this instrument. A CMOS sensor was selected as this provided an optimum balance between a low cost, and critical performance aspects such as small pixel size, large sensor extent, global shutter frame readout to avoid motion blur and a monochrome sensor array. A 405nm wavelength laser diode was selected to provide an optimal diffraction limited resolution whilst still being within the sensitivity limits of silicon detectors. The low coherence length of typical laser diodes preclude their use in more complicated off axis systems, however for the short path differences between background and scattered beams in the inline geometry used in this imager this was not found to be a concern. A Raspberry Pi computer

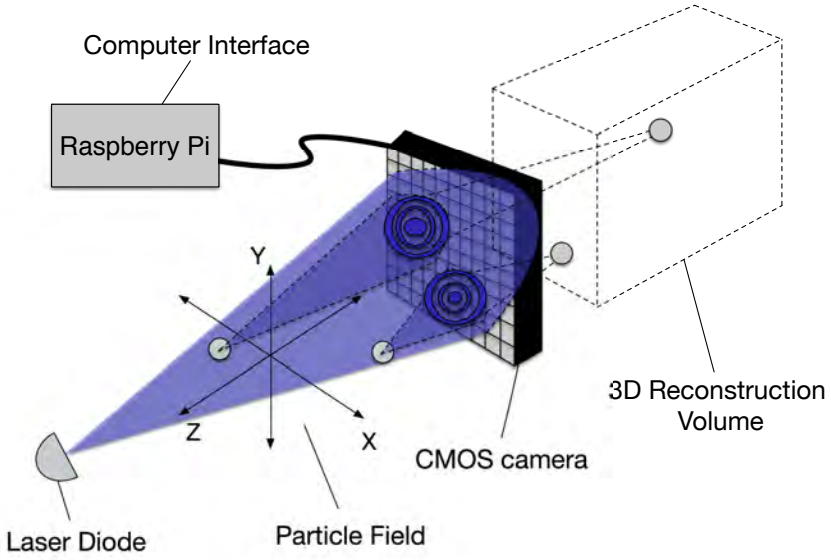

Figure 1. In line holographic recording geometry as used in this imager. A laser diode produces a coherent spherical wavefront and the interference between background and scattered light from the object field is recorded on a CMOS sensor. This interference pattern is then saved on a low cost Raspberry Pi computer for further processing.

was included to save the recorded images and also provides the potential for in flight analysis of images and for quality control considerations.

The instrument is intended for deployment on a weather balloon and for typical weather balloon ascent rates of 5 m/s the motion blur of micron scale cloud particles becomes significant. To reduce this blurring a digital pulsing circuit incorporating a high speed MOSFET gate driver was designed. The laser was pulsed with a pulse width between 100ns and 1μs, depending on the required pulse energy to adequately expose the camera for a given sampling volume. The pulse repetition frequency determines the sampling rate of the imaging system and this is limited by the data transfer capabilities of the computer interface. It was determined that a maximum sampling rate of 2 fps was attainable for full RAW image recording with the Raspberry Pi interface, however this can be significantly increased with the inclusion of recently developed low cost ARM based mini computers.

Temperatures within a cloud can extend to below -40°C[25] and hence temperature control systems are needed to stabilise laser wavelength and avoiding icing up of the sampling windows and electronics. If an optical filter is incorporated to minimise the contribution of background sunlight, the wavelength must be controlled to within the bandpass region of the filter which is typically on the order of 10nm. A change in the laser wavelength will also lead to a change in the extent of the recorded interference pattern and hence if this is not accurately characterised uncertainties will be introduced in determining the sizes of the scattering particles. To overcome these issues a PID temperature controller circuit was designed and tested for use with a Peltier thermoelectric heater/cooler (TEC) to provide a closed loop temperature control system. The laser diode mount was designed for efficient heat transfer to the diode whilst also allowing heat sinking of the TEC. Further heating was provided by simple power resistors to avoid condensation of the sampling windows and electronics. An Arduino based weather station is included to record both internal and external temperature and relative humidity for comparison with microphysical data and also for potential correction of temperature dependent drifts.

The instrument enclosure must be suitably robust such that it can protect the internal electronics from the harsh environmental conditions whilst not significantly disturbing the sampling region. For this reason the main electronics components are stored in a central main box on top of which are two smaller boxes containing the camera and laser systems as shown in Figure 2. Each box has been carefully waterproofed and all components are mounted in a modular fashion to enable simple

Figure 2. Digital holographic imaging system in designed enclosure. From top left to bottom right the following modular components are shown; external hard drive storage, computing and control systems, power regulation and pulsing circuitry, camera with optional optical filter and adjustable laser diode mount.

upgrade and reconfiguration of the system for a given experiment. The spacing of these boxes may be varied to control the size of the sampling volume. The potential for deployment on a weather balloon poses further constraints on the overall size and weight of the completed system and so components and materials have been selected to facilitate this goal. An external hard drive and cable gland access are provided for extended ground based deployment and testing purposes. The external hard drive is not required for weather balloon deployment since data obtained within the short flight durations can be stored on a USB or SD card. Due to the modular design of the system, the space allocated to the hard drive can be instead used for a battery power supply for deployment on a weather balloon.

2.3 Image reconstruction and analysis software

Digital holography requires an efficient implementation of scalar diffraction theory for propagation of the complex object field recorded at the camera plane to a range of depth positions to reconstruct the original object field. Software has been developed to undertake this numerical diffraction, apply optional filtering, background subtraction and display the resultant three dimensional image in various forms. Due to the large datasets encountered in digital holography an automated analysis routine was developed to extract the relevant microphysical observables such as particle size distribution and particle shapes.

Direct computation with the Rayleigh-Sommerfield diffraction theory is computationally challenging and hence in practice either the Fresnel approximation or the alternate formulation of Angular Spectrum Diffraction are used for holographic reconstruction.[26] Both algorithms have been implemented making use of the FFT operation. Each diffraction algorithm has a corresponding propagation distance to which the phase of the propagation matrix is undersampled and so software was developed to select the appropriate formulation for a given reconstruction depth and system geometry. It has been shown that background subtraction techniques can be used to reduce noise in the reconstructed image,[27] and these features have also been implemented automatically here.

For typical cloud particle densities and holographic sampling volumes on the order of a cubic centimetre or greater, a single hologram can capture information about hundreds of cloud particles. Each hologram must then be numerically focussed by identifying the plane in which the reconstructed objects come into best focus and then analysed to extract

object observables such as their size, shape and spatial distribution. For holograms recorded a few times a second or greater this can become extremely challenging to analyse by manual inspection. Various methods have been proposed to perform this analysis automatically based on computer vision algorithms[28–31] and an automated analysis routine based on these results was implemented in this work.

The algorithm begins by determining the particle position as a function of depth by use of an intensity criteria. The particle boundary is determined with intensity threshold and edge detection algorithms and converted to a binary image. The particle size is then calculated by counting the number of pixels after correction for magnification effects and the physical pixel size uncertainty. Particle shape parameters such as aspect ratio are also recorded along with a separate image of each reconstructed particle.

3. SYSTEM CALIBRATION AND EXPERIMENTAL TESTING

Given the complexity involved in the image reconstruction and automated analysis stages along with non ideal effects introduced by the electro optical components a holographic system must be characterised with known test samples. Independent testing with a USAF resolution target and calibration test spheres was performed to test both the image reconstruction performance and the automated analysis software.

3.1 Experimental testing

The resolution and performance of a holographic imaging system is dependent on a range of factors[32] including the beam coherence, wavefront quality, diffraction limit, reconstruction depth spacing, shot noise and edge detection criteria. Rather than independently trying to characterise each of these effects, the overall resolution of the system was determined by testing with known reference objects.

To test the reconstruction algorithm performance, a range of calibration test spheres and a USAF resolution test target were used to verify the uniqueness of the reconstructed image positions as well as the sizing algorithm performance. The particle size is determined by first identifying the depth position at which the reconstructed particle is in best focus. This depth is then used along with the known laser depth position to determine the true object depth based on the standard holographic imaging equations.[33] The geometric magnification of the divergent spherical wave is then determined and used to measure the true particle size based on the size of the magnified reconstructed image of the particle. An example of the reconstructed three dimensional image produced from this process is shown in the attached video in Figure 3. Two sets of calibration test spheres are placed at two different depth positions within the sampling volume. The intensity throughout this sampling volume is then reconstructed and the two distinct sets of particles are seen to come into focus at their original depth positions as expected.

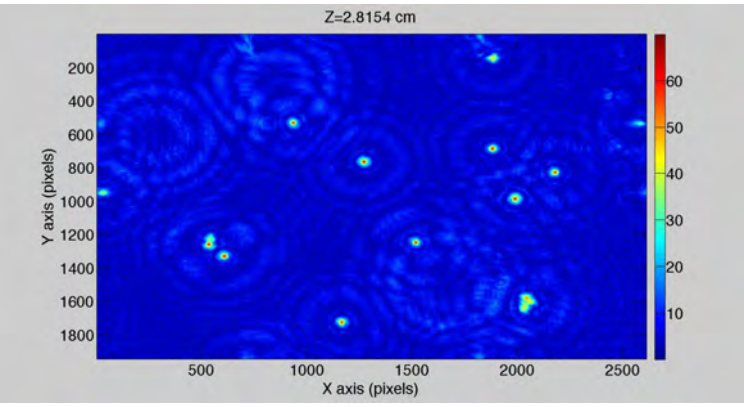

Figure 3. Video 1: Example of a reconstructed three dimensional image. 20 micron calibration test spheres were placed at two depth positions in the sampling volume. As the reconstructed intensity is scanned through the depth, both sets of particles are seen to come into focus at their corresponding depth positions as expected. Note that the low image resolution is due to compression to reduce the file size. http://dx.doi.org/doi.number.goes.here

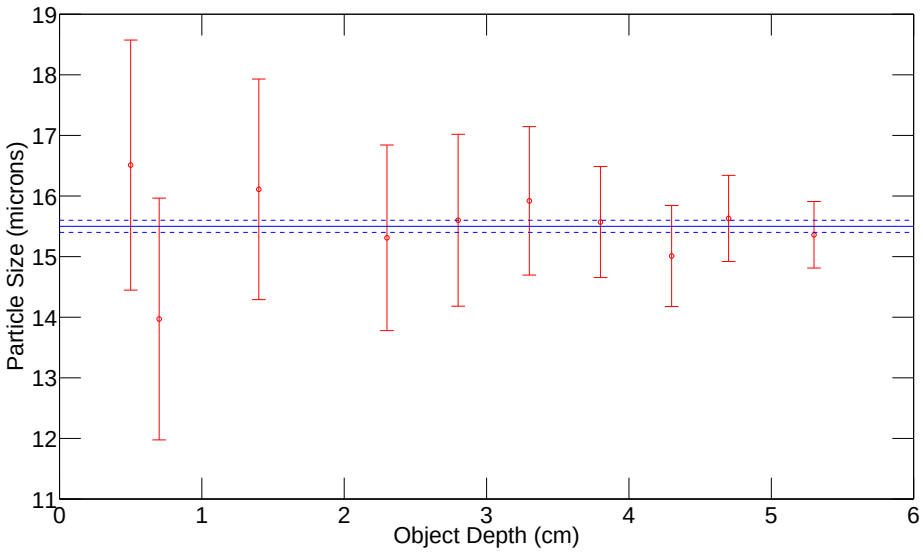

Figure 4. Reconstructed particle sizes for a set of 15.5 micron calibration test spheres placed throughout the instrument sampling volume. Measurements agree with the actual particle size value to within the experimental uncertainty. Object depth is defined as the distance from the camera sensor.

A set of monodisperse calibration test spheres with a diameter of 15.5 microns were placed at a range of depth positions throughout the instrument sampling volume to characterise the sizing algorithm performance. The reconstruction program was then used to measure the size of these objects and the results are shown in Figure 4. The measured particle sizes agree with the actual value at all positions measured to within the experimental uncertainty attributed to the sizing algorithm. The uncertainty was determined by measuring the change in calculated particle size as the number of pixels in the particle boundary is varied. This uncertainty depends on the position of the particle in the sampling volume due to the depth dependence of the spherical wavefront magnification factor.

3.2 Automated analysis software

An automated analysis routine was developed to extract particle properties from the recorded holograms. The program initially determines the three dimensional location of each reconstructed particle by means of an image focussing criteria. An intensity threshold and edge detection criteria is then applied to isolate each particle and extract the particle size, shape and spatial location. This information is stored for each particle and a histogram can then be built up to determine the statistical properties within the sampling volume.

The algorithm was tested with a range of calibration test spheres placed throughout the sampling volume. An example of this testing is shown in Figure 5. A set of polydisperse test spheres with sizes ranging between 63 microns and 75 microns were placed at a single depth position and the automated analysis routine was used to extract the particle properties. It is seen that most particles were successfully identified as indicated by the red boundary circles assigned by the code. The extracted particle size distribution is shown in Figure 6. If a uniform size distribution is assumed for the spheres, the measured variation is in agreement with the uncertainties associated with particle counting statistics. It can be seen that not all particles were successfully identified and some were misclassified. The performance of this algorithm is expected to improve with the use of more realistic intensity threshold criteria and edge detection tests and this information can be obtained by manual observation of results of a field test of the instrument that is currently under way.

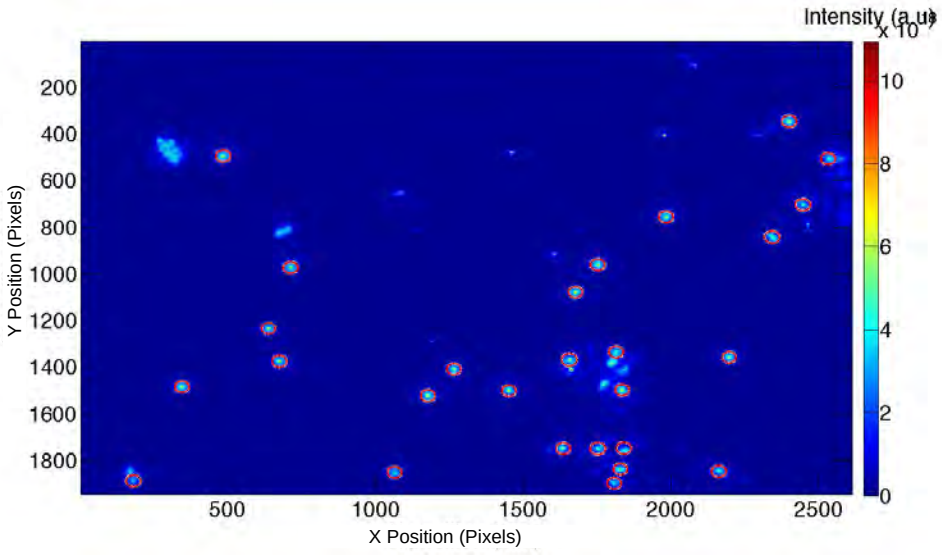

Figure 5. Reconstructed intensity of a set of polydisperse calibration test spheres with sizes ranging from 63 microns to 75 microns. The red circles indicate particles identified by the algorithm to be sized and extracted. Most particles are successfully identified however there are cases of missed particles and misclassification that can be improved on.

4. CONCLUSIONS AND FUTURE WORK

A low cost, light weight digital holographic imaging system suitable for deployment on a weather balloon or ground based tower structure has been designed and experimentally tested. Software has been developed for efficient three dimensional image reconstruction and automated analysis. Validation of the system was undertaken using known calibration test spheres and a USAF resolution target. It was found that the system could automatically and accurately extract the relevant object observables throughout the three dimensional sampling volume however further testing and more realistic intensity thresholding criteria are required to improve the reliability of the automated analysis routine.

The system is currently deployed at a ground based field site on a Tasmanian mountain for testing. Data from this experiment can be compared with measurements from collocated devices including a polarimetric backscatter instrument and a nearby weather station. The results of this field testing will guide the necessary upgrades that must be made in coping with any unexpected environmental challenges faced. If successful, the next development stage will involve integration with a weather balloon system allowing direct validation and calibration of both satellite and ground based remote sensing retrievals of cloud microphysical observations over widespread regions.

ACKNOWLEDGMENTS

The authors are grateful to Philip Nelson and Robert Males of TasNetworks for their excellent support in the installation of this instrument at the Tasmanian field site. Bob Chivell is thanked for his assistance in the design and construction of the instrument enclosure and optical mounts. Financial support from the University of Adelaide and the South Australian Government Department of State Development is gratefully acknowledged.

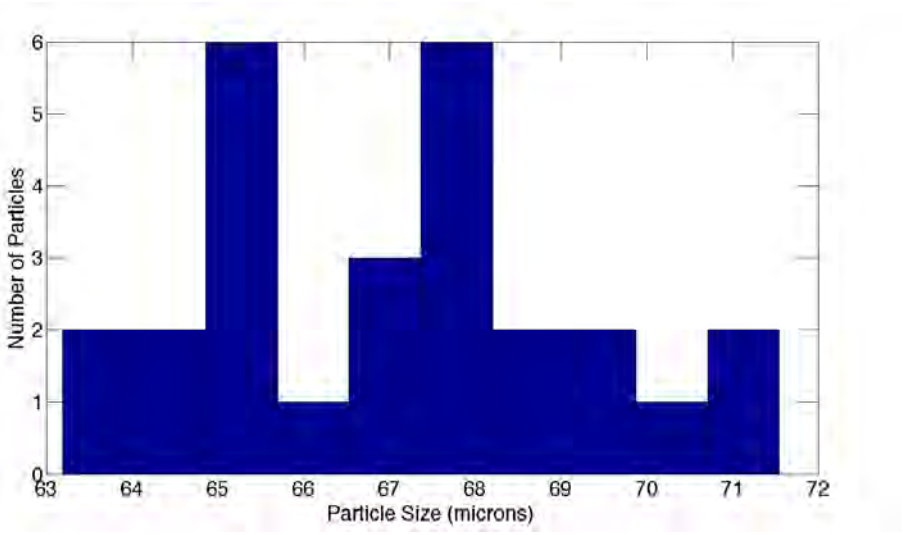

Figure 6. Extracted particle size distribution for the polydisperse 63 to 75 micron calibration test sphere sample. Sizes are consistent with inherit uncertainties due to particle counting statistics.

REFERENCES

[1] Flato, G., Marotzke, J., Abiodun, B., Braconnot, P., Chou, S., Collins, W., Cox, P., Driouech, F., Emori, S., Eyring, V., Forest, C., Gleckler, P., Guilyardi, E., Jakob, C., Kattsov, V., Reason, C., and Rummukainen, M., "Evaluation of Climate Models, in: Climate Change 2013: The Physical Science Basis. Contribution of Working Group I to the Fifth Assessment Report of the Intergovernmental Panel on Climate Change," tech. rep. (2013).

[2] Stephens, G. L., Vane, D. G., Boain, R. J., Mace, G. G., Sassen, K., Wang, Z., Illingworth, A. J., O'Connor, E. J., Rossow, W. B., Durden, S. L., Miller, S. D., Austin, R. T., Benedetti, A., and Mitrescu, C., "The cloudsat mission and the A-Train: A new dimension of space-based observations of clouds and precipitation," *Bulletin of the American Meteorological Society* **83**(12), 1771–1790 (2002).

[3] Baker, M. B., "Cloud Microphysics and Climate," *Science* **276**(5315), 1072–1078 (1997).

[4] Shupe, M. D., Turner, D. D., Walden, V. P., Bennartz, R., Cadeddu, M. P., Castellani, B. B., Cox, C. J., Hudak, D. R., Kulie, M. S., Miller, N. B., Neely, R. R., Neff, W. D., and Rowe, P. M., "High and Dry: New Observations of Tropospheric and Cloud Properties above the Greenland Ice Sheet," *Bulletin of the American Meteorological Society* **94**, 169–186 (feb 2013).

[5] Shaw, R. A., "Particle-Turbulence Interactions in Atmospheric Clouds," *Annual Review of Fluid Mechanics* **35**(1), 183–227 (2003).

[6] Morrison, H., de Boer, G., Feingold, G., Harrington, J., Shupe, M. D., and Sulia, K., "Resilience of persistent Arctic mixed-phase clouds," *Nature Geoscience* **5**, 11–17 (2011).

[7] Stephens, G. L. and Kummerow, C. D., "The remote sensing of clouds and precipitation from space: a review," *Journal of the Atmospheric Sciences* **64**(11), 3742–3765 (2007).

[8] Van Diedenhoven, B., Cairns, B., Fridlind, A. M., Ackerman, A. S., and Garrett, T. J., "Remote sensing of ice crystal asymmetry parameter using multi-directional polarization measurements - Part 2: Application to the Research Scanning Polarimeter," *Atmospheric Chemistry and Physics* **13**(6), 3125–3203 (2013).

[9] van Diedenhoven, B., Fridlind, A. M., Ackerman, A. S., and Cairns, B., "Evaluation of hydrometeor phase and ice properties in cloud-resolving model simulations of tropical deep convection using radiance and polarization measurements," *Journal of the Atmospheric Sciences* , 3290–3314 (2012).

[10] Sikand, M., Koskulics, J., Stamnes, K., Hamre, B., Stamnes, J. J., and Lawson, R. P., "Estimation of Mixed-Phase Cloud Optical Depth and Position Using In Situ Radiation and Cloud Microphysical Measurements Obtained from a Tethered-Balloon Platform," *Journal of the Atmospheric Sciences* **70**(1), 317–329 (2013).

[11] Curry, J. A., Hobbs, P. V., King, M. D., Randall, D. A., Minnis, P., Isaac, G. A., Pinto, J. O., Uttal, T., Bucholtz, A., Cripe, D. G., Gerber, H., Fairall, C. W., Garrett, T. J., Hudson, J., Intrieri, J. M., Jakob, C., Jensen, T., Lawson, P., Marcotte, D., Nguyen, L., Pilewskie, P., Rangno, A., Rogers, D. C., Strawbridge, K. B., Valero, F. P. J., Williams, A. G., and Wylie, D., "FIRE arctic clouds experiment," *Bulletin of the American Meteorological Society* **81**(1), 5–29 (2000).

[12] Yang, P., Bi, L., Baum, B. A., Liou, K.-N., Kattawar, G. W., Mishchenko, M. I., and Cole, B., "Spectrally Consistent Scattering, Absorption, and Polarization Properties of Atmospheric Ice Crystals at Wavelengths from 0.2 to 100 μ m," *Journal of the Atmospheric Sciences* **70**, 330–347 (jan 2013).

[13] Baum, B. A., Heymsfield, A. J., Yang, P., and Bedka, S. T., "Bulk Scattering Properties for the Remote Sensing of Ice Clouds. Part II: Narrowband Models," *Journal of Applied Meteorology* **44**(12), 1885–1895 (2005).

[14] Okamoto, H., "An algorithm for retrieval of cloud microphysics using 95-GHz cloud radar and lidar," *Journal of Geophysical Research* **108**(D7), 1–21 (2003).

[15] Wang, Z., French, J., Vali, G., Wechsler, P., Haimov, S., Rodi, A., Deng, M., Leon, D., Snider, J., Peng, L., and Pazmany, A. L., "Single aircraft integration of remote sensing and in situ sampling for the study of cloud microphysics and dynamics," *Bulletin of the American Meteorological Society* **93**(5), 653–668 (2012).

[16] King, M. D., Platnick, S., Yang, P., Arnold, G. T., Gray, M. A., Riedi, J. C., Ackerman, S. A., and Liou, K. N., "Remote sensing of liquid water and ice cloud optical thickness and effective radius in the Arctic: Application of airborne multispectral MAS data," *Journal of Atmospheric and Oceanic Technology* **21**(6), 857–875 (2004).

[17] Baumgardner, D., Brenguier, J. L., Bucholtz, a., Coe, H., DeMott, P., Garrett, T. J., Gayet, J. F., Hermann, M., Heymsfield, a., Korolev, a., Krämer, M., Petzold, a., Strapp, W., Pilewskie, P., Taylor, J., Twohy, C., Wendisch, M., Bachalo, W., and Chuang, P., "Airborne instruments to measure atmospheric aerosol particles, clouds and radiation: A cook's tour of mature and emerging technology," *Atmospheric Research* **102**, 10–29 (2011).

[18] Heymsfield, A. J., "On measurements of small ice particles in clouds," *Geophysical Research Letters* **34**(23), 1–6 (2007).

[19] Lawson, R. P., Stamnes, K., Stamnes, J., Zmarzly, P., Koskuliks, J., Roden, C., Mo, Q., Carrithers, M., and Bland, G. L., "Deployment of a tethered-balloon system for microphysics and radiative measurements in mixed-phase clouds at Ny-Alesund and South Pole," *Journal of Atmospheric and Oceanic Technology* **28**(5), 656–670 (2011).

[20] Schnars, U. and Jüptner, W., "Direct recording of holograms by a CCD target and numerical reconstruction.," *Applied optics* **33**, 179–181 (1994).

[21] Beals, M. J., Fugal, J. P., Shaw, R. A., Lu, J., Spuler, S. M., and Stith, J. L., "Holographic measurements of inhomogeneous cloud mixing at the centimeter scale," *Science (New York, N.Y.)* **350**(6256), 87–90 (2015).

[22] Henneberger, J., Fugal, J. P., Stetzer, O., and Lohmann, U., "HOLIMO II: a digital holographic instrument for ground-based in situ observations of microphysical properties of mixed-phase clouds," *Atmospheric Measurement Techniques* **6**(11), 2975–2987 (2013).

[23] Beck, A., Henneberger, J., Schöpfer, S., and Lohmann, U., "HoloGondel: in-situ cloud observations on a cable car in the Swiss Alps using a holographic imager," *Atmospheric Measurement Techniques Discussions* **25**(August), 1–26 (2016).

[24] Garcia-sucerquia, J., Xu, W., Jericho, S. K., Klages, P., Jericho, M. H., and Kreuzer, H. J., "Digital in-line holographic microscopy," *Applied Optics* **45**(5) (2006).

[25] Stubenrauch, C. J., Rossow, W. B., Kinne, S., Ackerman, S., Cesana, G., Chepfer, H., Di Girolamo, L., Getzewich, B., Guignard, a., Heidinger, a., Maddux, B. C., Menzel, W. P., Minnis, P., Pearl, C., Platnick, S., Poulsen, C., Riedi, J., Sun-Mack, S., Walther, a., Winker, D., Zeng, S., and Zhao, G., "Assessment of global cloud datasets from satellites: Project and database initiated by the GEWEX radiation panel," *Bulletin of the American Meteorological Society* **94**(7), 1031–1049 (2013).

[26] Molony, K. M., Hennelly, B. M., Kelly, D. P., and Naughton, T. J., "Reconstruction algorithms applied to in-line Gabor digital holographic microscopy," *Optics Communications* **283**(6), 903–909 (2010).

[27] Fugal, J. P. and Shaw, R. A., "Cloud particle size distributions measured with an airborne digital in-line holographic instrument," *Atmospheric Measurement Techniques Discussions* **2**, 659–688 (2009).

[28] Fugal, J. P., Schulz, T. J., and Shaw, R. A., "Practical methods for automated reconstruction and characterization of particles in digital in-line holograms," *Measurement Science and Technology* **20**, 075501 (2009).

[29] Zhu, Y., Carragher, B., Mouche, F., and Potter, C. S., "Automatic Particle Detection through Efficient Hough Transforms," *IEEE Transactions on Medical Imaging* **22**(9), 1053–1062 (2003).

[30] Atherton, T. J. and Kerbyson, D. J., "Size invariant circle detection," *Image and Vision Computing* **17**(February 1997), 795–803 (1999).

[31] Meyer, F. and Beucher, S., "Morphological segmentation," *Journal of Visual Communication and Image Representation* **1**(1), 21–46 (1990).

[32] Cartwright, S., Dunn, P., and Thompson, B., "Particle sizing using far -field holography: new developments," *Optical Engineering* **19**(5), 727–733 (1980).

[33] Meier, R., "Magnification and Third-Order Aberrations in Holography," *Journal of the Optical Society of America* **55**(8), 987–992 (1965).